

## INFORMATION TO USERS

This manuscript has been reproduced from the microfilm master. UMI films the text directly from the original or copy submitted. Thus, some thesis and dissertation copies are in typewriter face, while others may be from any type of computer printer.

**The quality of this reproduction is dependent upon the quality of the copy submitted.** Broken or indistinct print, colored or poor quality illustrations and photographs, print bleedthrough, substandard margins, and improper alignment can adversely affect reproduction.

In the unlikely event that the author did not send UMI a complete manuscript and there are missing pages, these will be noted. Also, if unauthorized copyright material had to be removed, a note will indicate the deletion.

Oversize materials (e.g., maps, drawings, charts) are reproduced by sectioning the original, beginning at the upper left-hand corner and continuing from left to right in equal sections with small overlaps.

Photographs included in the original manuscript have been reproduced xerographically in this copy. Higher quality 6" x 9" black and white photographic prints are available for any photographs or illustrations appearing in this copy for an additional charge. Contact UMI directly to order.

ProQuest Information and Learning  
300 North Zeeb Road, Ann Arbor, MI 48106-1346 USA  
800-521-0600

UMI<sup>®</sup>



NULLING INTERFEROMETRY FOR STUDYING OTHER PLANETARY  
SYSTEMS: TECHNIQUES AND OBSERVATIONS

by  
Philip Mark Hinz

---

A Dissertation Submitted to the Faculty of the  
DEPARTMENT OF ASTRONOMY  
In Partial Fulfillment of the Requirements  
For the Degree of  
DOCTOR OF PHILOSOPHY  
In the Graduate College  
THE UNIVERSITY OF ARIZONA

2 0 0 1

UMI Number: 3010268



---

UMI Microform 3010268

Copyright 2001 by Bell & Howell Information and Learning Company.

All rights reserved. This microform edition is protected against  
unauthorized copying under Title 17, United States Code.

---

Bell & Howell Information and Learning Company  
300 North Zeeb Road  
P.O. Box 1346  
Ann Arbor, MI 48106-1346

THE UNIVERSITY OF ARIZONA ©  
GRADUATE COLLEGE

As members of the Final Examination Committee, we certify that we have  
read the dissertation prepared by Philip Mark Hinz

entitled Nulling Interferometry for Studying Other Planetary Systems:  
Techniques and Observations

and recommend that it be accepted as fulfilling the dissertation  
requirement for the Degree of Doctor Philosophy

William F. Hoffmann  
William F. Hoffmann

1/31/01  
Date

Neville J. Woolf  
Neville J. Woolf

1/31/01  
Date

Donald W. McCarthy Jr.  
Donald W. McCarthy Jr.

1/31/01  
Date

J. Roger P. Angel  
J. Roger P. Angel

1/31/01  
Date

Michael R. Meyer  
Michael R. Meyer

1-31-01  
Date

Final approval and acceptance of this dissertation is contingent upon  
the candidate's submission of the final copy of the dissertation to the  
Graduate College.

I hereby certify that I have read this dissertation prepared under my  
direction and recommend that it be accepted as fulfilling the dissertation  
requirement.

J. Roger P. Angel  
Dissertation Director  
J. Roger P. Angel

1/31/01  
Date

## STATEMENT BY AUTHOR

This dissertation has been submitted in partial fulfillment of requirements for an advanced degree at The University of Arizona and is deposited in the University Library to be made available to borrowers under rules of the Library.

Brief quotations from this dissertation are allowable without special permission, provided that accurate acknowledgment of source is made. Requests for permission for extended quotation from or reproduction of this manuscript in whole or in part may be granted by the head of the major department or the Dean of the Graduate College when in his or her judgment the proposed use of the material is in the interests of scholarship. In all other instances, however, permission must be obtained from the author.

SIGNED: Philip H. H.

## ACKNOWLEDGMENTS

Many graduate students only have one advisor. I had the luxury of having effectively four, each giving me their approach to observing, solving problems, building instruments, and brainstorming. Roger Angel and Nick Woolf showed me the value of thinking out a problem from first principles, and not trusting conventional wisdom. Bill Hoffmann and Don McCarthy taught me the care and creativity required to build an efficiently working instrument. I am grateful to each one for the lessons they have taught me and hope some of their approach to problem solving shines through in this dissertation.

BLINC would not have been possible without the expert design work and fabrication by Elliott Solheid and Mitch Nash of Infrared Laboratories. They put up with my unannounced visits, last minute changes in the design, making of additional parts, and even changes after it was built, all without seeming to worry whether I really knew what I was doing. With all the 200+ parts the instrument worked the first time it was assembled, a testament to their skill.

I would also like to acknowledge the help of the MMT staff, including J.T. Williams, Bill Kindred, Ale Milone, John McAfee and Carol Heller who, both with the old and new MMT, provided expert support, so important for successful telescope observations with a new instrument. In addition Craig Foltz has given the project continual institutional support for which I am grateful.

Finally, I would like to thank my wife, Joannah, for all the proofreading, but more importantly, for the constant emotional and day-to-day support during all the telescope runs, stretches of lab work, and writing periods. I've become so used to the support you might think I'm not aware of it. But I am, and, as always, am deeply thankful for it.

## DEDICATION

To the “Astronomy Campers” who remind me each summer why I went into astronomy.



# TABLE OF CONTENTS

LIST OF FIGURES . . . . .	9
LIST OF TABLES . . . . .	11
ABSTRACT . . . . .	12
1 INTRODUCTION . . . . .	14
1.1 Planet Hunting . . . . .	15
1.2 Zodiacal Dust . . . . .	17
1.3 Direct Detection Methods . . . . .	18
2 NULLING INTERFEROMETRY BASICS . . . . .	20
2.1 Nulling Interferometry . . . . .	21
2.2 Achromatic Nulling . . . . .	25
3 GROUND-BASED NULLING DESIGN AND LIMITATIONS . . . . .	27
3.1 Design of a Nulling Beam-splitter . . . . .	28
3.1.1 Phase Compensation . . . . .	29
3.1.2 Amplitude Matching . . . . .	30
3.2 Control of the Null . . . . .	32
3.3 Limitations to Nulling . . . . .	35
3.3.1 Phase vs. Wavelength . . . . .	35
3.3.2 Intensity vs. Wavelength . . . . .	37
3.3.3 Polarization Effects . . . . .	39
3.3.4 Diameter of the Star . . . . .	42
3.3.5 Atmospheric Turbulence . . . . .	44
4 A PROTOTYPE NULLING INTERFEROMETER. WITH THE OLD MULTIPLE MIRROR TELESCOPE . . . . .	52

4.1	Optical Layout . . . . .	52
4.2	Observations . . . . .	55
5	DESIGN OF A CRYOGENIC NULLING INTERFEROMETER FOR THE 6.5 M MMT . . . . .	64
5.1	Instrument Description . . . . .	64
5.1.1	Nulling Optimization . . . . .	66
5.1.2	Optical Layout . . . . .	66
5.1.3	Mechanical Design . . . . .	68
5.1.4	The Mid-infrared Array Camera (MIRAC3) . . . . .	69
5.1.5	The Beam-splitter . . . . .	71
5.2	Phase Correction System . . . . .	71
5.3	Alignment of the Interferometer . . . . .	72
5.4	Expected Null Depth . . . . .	75
5.4.1	Phase vs. Wavelength . . . . .	76
5.4.2	Intensity and Polarization Effects . . . . .	76
5.4.3	Diameter of the Star . . . . .	77
5.4.4	Atmospheric Turbulence . . . . .	77
6	LABORATORY EXPERIMENTS IN PRECISE SOURCE CANCELLATION . . .	80
6.1	Experimental Setup . . . . .	80
6.2	Expected Null Depth . . . . .	81
6.3	Alignment and Tolerances . . . . .	82
6.4	Results . . . . .	83
7	NULLING OBSERVATIONS WITH THE 6.5 M MMT . . . . .	87
7.1	Observing Procedures . . . . .	87
7.2	Observations . . . . .	90
7.3	Calibration Stars . . . . .	90

7.4	Evolved Stars . . . . .	92
7.4.1	Resolved Examples . . . . .	94
7.5	Herbig Ae/Be Stars . . . . .	100
7.5.1	Model Parameters . . . . .	100
7.5.2	Measurements . . . . .	104
7.5.3	HD163296 . . . . .	106
7.6	Main Sequence stars . . . . .	106
7.6.1	Limit to Zodiacal Dust . . . . .	107
8	FUTURE OF GROUND-BASED NULLING . . . . .	111
8.1	Photometric Sensitivity . . . . .	111
8.1.1	MMT Nulling Sensitivity . . . . .	114
8.1.2	LBT Sensitivity . . . . .	115
8.2	Science Goals . . . . .	116
8.2.1	Zodiacal Dust . . . . .	117
8.2.2	Giant Planets . . . . .	121
8.3	2020 Telescope . . . . .	125
9	DESIGN CONSIDERATIONS FOR THE TERRESTRIAL PLANET FINDER . .	129
9.1	Configuration Design . . . . .	130
9.2	A Strawman Optical Design for TPF . . . . .	136
9.3	Nulling with a Mesh Beam-splitter . . . . .	138
9.3.1	Signal-to Noise Comparison of a Mesh Beam-splitter . . . . .	142
	REFERENCES . . . . .	144

## LIST OF FIGURES

2.1	A symmetric nulling interferometer. . . . .	22
3.1	A Symmetric Beam-splitter. . . . .	28
3.2	Plot of reflection intensity and phase difference for an 11 $\mu\text{m}$ symmetric beam-splitter. . . . .	33
3.3	Plot of reflection intensity and phase difference for a 5 $\mu\text{m}$ symmetric beam-splitter. . . . .	34
3.4	Phase variation and residual intensity for an 11 $\mu\text{m}$ beam-splitter. . .	38
3.5	Phase variation and residual intensity for a 5 $\mu\text{m}$ beam-splitter. . . .	39
3.6	Residual intensity from a finite stellar diameter. . . . .	43
4.1	Optical layout of the prototype nulling interferometer at the MMT. .	53
4.2	Prototype nulling instrument mounted at the central combining area of the MMT. . . . .	55
4.3	Plot of intensity variations of the null due to atmospheric turbulence.	57
4.4	Single short-exposure frames at 10.3 $\mu\text{m}$ showing constructive and destructive interference. . . . .	58
4.5	Combined nulled images for $\alpha$ Orionis and R Leonis. . . . .	62
4.6	Difference images showing the showing the suppressed diffraction pattern. . . . .	63
5.1	The optical layout of BLINC. . . . .	65
5.2	Mechanical Drawing and photo of the BLINC cryostat interior. . . .	69
5.3	Pupil image showing the two sides of the mirror overlapped. . . . .	74
6.1	The laboratory setup for demonstrating deep levels of nulling. . . .	82
6.2	Deep suppression of an artificial point source. . . . .	84
6.3	Measurement of phase compensation. . . . .	86

7.1	Constructive and destructive images for a typical calibrator star. . . .	93
7.2	Nulled image of dust around $\mu$ Cephei. . . . .	96
7.3	Nulled images of $\alpha$ Scorpii at two different baseline orientations. . . .	98
7.4	Nulled image of HD 188037 at $10.3\ \mu\text{m}$ . . . . .	99
7.5	Images of IRC+10216 showing the extended and point-like components.	101
7.6	Sketch of Herbig disk model. . . . .	102
8.1	Sky and telescope background in the thermal infrared. . . . .	113
8.2	Transmitted flux of zodiacal dust at the MMT for different spectral types at 10 pc. . . . .	118
8.3	Transmitted flux of zodiacal dust at the LBT for different spectral types at 10 pc. . . . .	119
8.4	Detectability of planets in the N, M, and L' bands. . . . .	122
8.5	Minimum planet mass detectable at L' for the MMT and LBT. . . . .	123
8.6	Comparison of parameter space for nulling and radial velocity detections. . . . .	124
9.1	Transmission patterns for three-element arrays. . . . .	134
9.2	Transmission patterns for four-element arrays. . . . .	135
9.3	An optical layout of an OASES beam-combiner. . . . .	137
9.4	An optical layout for a double Bracewell beam-combiner. . . . .	139
9.5	Pupil of a mesh beam-splitter system and resulting images. . . . .	141

## LIST OF TABLES

5.1	Contributing levels of residual intensity. . . . .	76
7.1	Observing log for nulling observations. . . . .	91
7.2	Nulling measurements of evolved stars at $10.3\ \mu\text{m}$ . . . . .	95
7.3	Model parameters and expected nulls for Herbig Ae/Be stars. . . . .	104
7.4	Observations of Herbig Ae/Be stars. . . . .	105
7.5	Observations of main sequence stars. . . . .	107
7.6	Parameter values for the solar zodiacal cloud. . . . .	109
7.7	Parameters for Vega and Altair. . . . .	109
8.1	Telescope parameters for sensitivity calculations. . . . .	115
8.2	Photometric sensitivity limits of the MMT and LBT nulling interferometers. . . . .	117
8.3	Detectable limits of dust around the nearest stars with the MMT nulling interferometer. . . . .	120
8.4	Detectability of planets at 10 pc at $L'$ band. . . . .	126

## ABSTRACT

Nulling interferometry is an important technique in the quest for direct detection of extrasolar planets. It is central to NASA's plans for a Terrestrial Planet Finder (TPF) mission to detect and characterize Earth-like planets. This thesis presents the first experiments to demonstrate that the technique is a useful tool for ground-based observations as well. It demonstrates the ability of the technique to study faint, circumstellar environments otherwise not easily observed. In addition the observations and experiments allow more confident estimation of expected sensitivity to planetary systems around nearby stars.

The old MMT was used for the first telescope experiments of stellar suppression via nulling. The stellar suppression achieved was sufficient to observe thermal emission from cool dust in the outflows around late-type stars. Based on the original MMT prototype, which worked at ambient temperature, I have constructed a cryogenic nulling interferometer for use with the renovated 6.5 m MMT. Features include the capability of sensing and correcting the phase between the two arms of the interferometer, achromatic tuning of the null using a unique symmetric beam-splitter, and compatibility with the deformable secondary of the MMT. The instrument has been used in a laboratory setup with an artificial source to demonstrate a high level of suppression. Commissioning of the instrument took place at the MMT in June 2000 using the fixed f/9 secondary. The instrument was aligned, phased, and used for science observations of 17 stars over five nights.

The future impact of nulling with the MMT and the Large Binocular Telescope is sketched out. These telescopes will be sensitive to very faint levels of zodiacal dust, indicative of planetary companions and giving us clues as to the make up

of planetary systems. Substellar companions down to near Jupiter mass will be detectable around the nearest stars for the LBT, allowing direct imaging of long-period giant planets. The detection of such companions will be complementary to the Doppler velocity searches, currently so succesful in verifying the existence of planets, thus giving a balanced view of the prevalence and range of separations possible for giant planets around nearby stars.



## CHAPTER 1

### INTRODUCTION

*It goes against nature in a large field to grow only one shaft of wheat,  
and in an infinite universe to have only one living world. -Metrodorus  
of Khios 400 B.C.*

Speculation about the existence of other worlds is nearly as old as human civilization itself. The argument that there “must” be other worlds, originating with Giordano Bruno, who realized the significance of the visible stars being like our sun, has only been sharpened by modern astronomy’s validation of how common sun-like stars are. In addition the success of Laplace’s nebular hypothesis in explaining the formation of the sun’s planetary system, as seen by disk formation around T Tauri stars, has validated ideas about the commonness of planetary systems. Of course, the excitement bound up in the speculation about other worlds is not simply whether rocky bodies exist around other stars, but whether those bodies are suitable for, and possibly even harbor, life.

While life on other planets is not yet able to be addressed scientifically, the question of whether other planetary systems exist has finally become a testable hypothesis in astronomy. The advances in high resolution, precision spectroscopy,

infrared sensing and large telescopes capable of high resolution imaging are fueling a sustained drive toward understanding the prevalence and formation of planetary systems around sun-like stars such as our own.

### 1.1. Planet Hunting

Searching for planets is not an easy task. Perhaps the most telling evidence of this statement is the degree to which the question of other planetary systems has remained unanswered despite humanity's long standing interest in the problem. The planet-finding field is still in its infancy even with astronomical instrumentation which has allowed astronomy to progress from largely empirical knowledge of stars and nebulae in the sky at the end of the nineteenth century to a surprisingly extensive understanding at the end of the twentieth century as to the structure and origin of celestial objects from the stellar scale to the size of the cosmic horizon. Planets have not been directly seen by the casual or dedicated observations of even the most powerful telescopes.

Yet planets *have* been detected via their gravitational influence on their parent star. High resolution spectroscopic observations have revealed the existence of planets around 50 or so nearby stars (Marcy Cochran, and Mayor 2000). These detections include several systems with evidence of multiple planets, indicative of a planetary system. The portent of these surveys has perhaps not yet been fully grasped by the astronomical community and the public. Approximately 6% of stars of spectral type F-K ( $\sim 0.5\text{-}1.5M_{\odot}$ ) are known to have Jupiter-mass planets within approximately 3 AU (Butler et al. 2000), according to these Doppler surveys. The observations appear to be upholding the Copernican principle for our planetary system; that is, our solar system seems to be just an average planetary system,

common around sun-like stars.

Or is it? Most planets found by Doppler velocity surveys are giant planets at distances of  $\leq 1$  AU. The existence of such planets suggests planetary systems whose makeup is very different from ours. Theories which explain the existence of these close-in planets suggest that they needed to form out beyond 5 AU and spiral in to their present position, in the process disrupting the orbit of any smaller interior planets. Even planets discovered outside the region where rocky planets would be expected to harbor life (the habitable zone) have elliptic orbits which would make this zone dynamically unstable for smaller planets. These glimpses of other systems make the existence of an Earth-like planet in them appear unlikely. However, Doppler velocity searches are particularly sensitive to these short-period planets, giving us a skewed view of what we can expect a “typical” system to look like. These searches are much less sensitive to long period planets similar to our own Jupiter or Saturn, both from the decrease in Doppler shift amplitude with separation and the long time it takes for these planets to complete an orbit. To see giant planets at  $\geq 5$  AU our best hope is to detect them directly.

Direct detection is difficult due to two fundamental properties of a planetary system: the planets are very faint compared to the central star of the system, and the planets’ angular separations from the star as viewed from the Earth are very small due to the great distance of even the closest stars. If our solar system were observed at a wavelength of  $10\ \mu\text{m}$  where the planets are relatively brighter, compared to the Sun, than in the visible, Jupiter would be approximately  $10^6$  times fainter and Earth would be  $10^7$  times fainter than the Sun.

For gas-giant planets, potentially detectable from the ground, theoretical models of their spectra (Burrows 1997) suggest that even companions which are

quite cool have significant thermal emission, well above what would be expected from blackbody emission, especially in the 4-5  $\mu\text{m}$  region where a lack of absorption bands from methane and water at these wavelengths allows light from deep within the atmosphere of the planet to escape. This makes the L and M atmospheric windows attractive regions of the spectrum to search for exo-solar giant planets.

## 1.2. Zodiacal Dust

The presence of a planetary system can also be inferred if there is extended thermal emission from a zodiacal dust disk. Zodiacal dust disks are the “smoking gun” of planetary systems around mature main sequence stars. Once accretion has terminated in the disk the zodiacal dust is affected by Poynting-Robertson drag which, clears the inner region ( $< 50$  AU) of the disk in under a million years (Backman and Paresce 1993). The existence of detectable zodiacal dust around main sequence stars requires not only a reservoir in the form of planetesimals for the continuously created dust, but larger planetary bodies for perturbing them into frequent collisions.

As an indicator of a planetary system, zodiacal dust is easier to detect than the planets themselves. The integrated surface brightness of a zodiacal dust disk at solar level is a factor of  $10^4$  fainter than the stellar photosphere in the mid-infrared. Since typical photometry by IRAS and ground-based observations has an uncertainty of 3%, zodiacal emission is only detectable for disks approximately 1000 times as bright as solar level. In addition the area of emission comes from a very compact region around the star. In the 8-13  $\mu\text{m}$  window which provides a suitable spectral region for ground-based zodiacal dust searches, the zodiacal dust cloud of an exo-solar system is expected to be only several AU in size. Thus, even

the brighter signal of the zodiacal disk is difficult to detect in the presence of the central star.

### 1.3. Direct Detection Methods

Many techniques have been proposed for direct detection including adaptive optics coronagraphs, differential band imaging and nulling interferometry. Nulling interferometry, a technique which interferometrically suppresses the starlight, was originally proposed by Bracewell (1978) for use in space-based searches for exo-solar planets. It is perhaps most promising among the different techniques since it is able to suppress the overwhelming starlight while still allowing sensitivity to companions quite close-in to the star. The successful application of this for planet searching is just now becoming feasible as telescopes with sufficient collecting area for detecting these faint signals are being completed and outfitted with adaptive optics systems to control the incoming wavefront.

With these advances in technology the advent of a new field in astronomy, the direct detection of extra-solar planets, is on the horizon. We can expect dramatic progress (and success, one hopes) toward this over the next decade. The observations will help provide a complementary look at the distribution of giant planets compared to Doppler searches by being more sensitive to planets with larger separations. In addition direct detection will allow detailed study of giant planets through their spectra. Zodiacal dust detection will provide information on the distribution of material in a planetary system.

This thesis presents the detailed design constraints needed to make nulling interferometry viable for exo-solar system studies as well as experimental verification of the technique both in the laboratory and with telescope observations.

Chapter 2 describes the concept behind nulling interferometry. Chapter 3 discusses the limits, from different sources, to the level of suppression achievable. Chapter 4 presents the design and results from the first telescopic demonstration of nulling using the original Multiple Mirror Telescope (MMT). Chapters 5-7 describe the design, testing, and use of a cryogenic nulling interferometer on the new 6.5 m MMT for observations of circumstellar structure. Chapter 8 looks at the future of ground-based nulling for detecting and studying exo-solar planetary systems. Chapter 9 discusses design issues related to the Terrestrial Planet Finding (TPF) mission.

## CHAPTER 2

### NULLING INTERFEROMETRY BASICS

Although our understanding of interference in light dates back to Thomas Young (1773-1829), interferometry, as an astronomical technique, was not employed until the early twentieth century with Michelson's observations using the 100 inch telescope on Mt. Wilson to measure the visibility of stars seen through his interferometer. Michelson mounted a beam with two pairs of diagonal mirrors on the telescope which relayed two sections of a stellar wavefront separated by up to 20 feet to within the telescope diameter so they could be brought to a common focus by the telescope optics. The light from the two arms thus formed a single image of a star which was modulated by fringes perpendicular to the baseline of the interferometer. When the baseline was long enough to resolve the diameter of the star the fringes would disappear, providing a sensitive indicator of the spatial size of an object. In this way the diameter of Betelgeuse was first measured (Michelson and Pease 1921) and the viability of optical interferometry to measure the spatial extent of celestial objects was first demonstrated.

Present-day long baseline optical interferometers overlap the entire pupil of separate telescopes using a semi-transparent mirror. Whereas Michelson's stellar interferometer creates fringes in the image plane, when the pupils are overlapped

the fringes are created in the pupil plane. Since the images are also overlapped the fringes can be said to exist “on the sky”. That is, the interference pattern of the interferometer modulates the source function. The interference of a point source between the two telescopes is measured by scanning the relative path-length to measure the contrast or visibility of the fringes through temporal fluctuations. This type of interferometry is typically referred to, somewhat confusingly, as Michelson interferometry (referring to the Michelson interferometer used, for example, in the Michelson-Morley measurements of the variation in the speed of light, not to Michelson’s stellar interferometer).

A few interferometers, such as the original Multiple Mirror Telescope, overlap the images while preserving the sine condition of the array. That is, the exit pupil of the interferometric system looks identical, except for overall scale, to the entrance pupil of the system. This causes the interferometer to act like a single telescope but with a point-spread function (PSF) which is the Fourier transform of its entrance pupil. This has the advantage of providing a wide field of view. Such an interferometer is usually referred to as a Fizeau interferometer, or an imaging interferometer, since it is possible to form images of extended structure at the spatial resolution of the interferometer, by simple deconvolution of the interferometric PSF. This technique is ideally suited for interferometers on a common mount so that their pupil orientation and path-lengths are fixed.

## 2.1. Nulling Interferometry

Nulling interferometry, in its essence, is a Michelson (pupil overlapping) interferometer designed for specific use in suppressing the light from a dominant central point source. The pupils are overlapped using a semi-transparent mirror



(Figure 2.1) so that the path-length differences affect the brightness of the overlapping images. However, the phase difference is constantly maintained at a half-wave to interfere the light destructively at one output. A companion next to this suppressed source will have a different phase relation ( $\Delta\Phi$  in Figure 2.1) depending on its separation from the point source in the direction along the line connecting the telescopes. This phase can be determined through simple geometry. Since the pupils are exactly superposed, the phase difference, relative

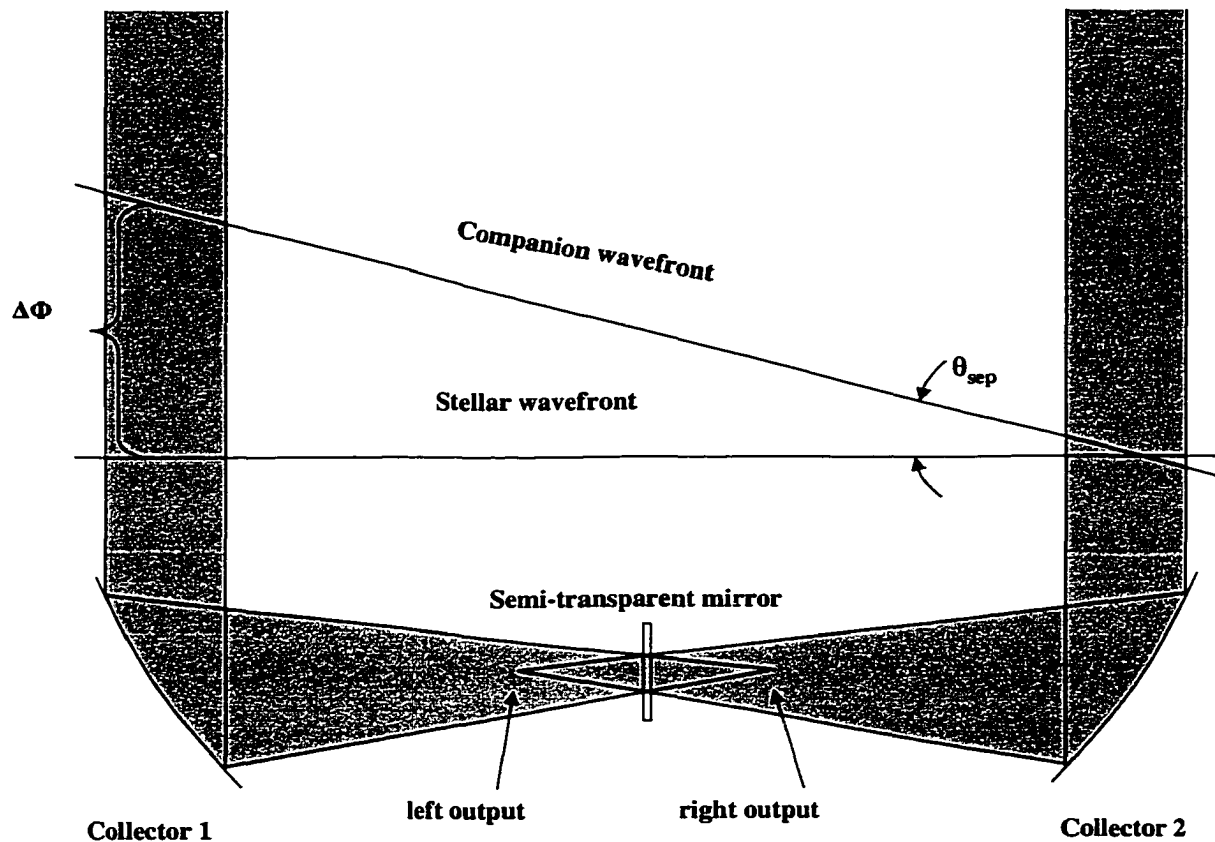


Figure 2.1 A symmetric nulling interferometer. A nulling interferometer contains two essential components: a pair of collectors and a semi-transparent mirror.

to the suppressed source, is set by the difference in path-length, relative to the star's wavefront, introduced by the tilt of the companion's wavefront across the baseline of the interferometer. Thus a path-length difference of a  $(n+1/2)$  waves relative to the suppressed star, the condition required for constructive interference, is introduced for a source which is separated by

$$\theta_{sep} = \left(n + \frac{1}{2}\right) \frac{\lambda}{2b} \quad (2.1)$$

from the star, where  $\theta$  is the angle in radians,  $\lambda$  is the wavelength of observation,  $b$  is the baseline of the interferometer, and  $n$  is an integer number. This is simply due to the fringe spacing of the interferometer. The phase at which the light interferes for a point source is determined by its position, relative to the suppressed point source. For an extended source different parts of the object interfere at different phases. As a result parts of it are enhanced and parts suppressed. The object intensity distribution is multiplied by a transmission function due to the interferometer

$$T(\theta) = \sin^2 \left( \frac{\pi \theta b}{\lambda} \right), \quad (2.2)$$

where  $\theta$  is the angular distance from the line on the sky through the star perpendicular to the interferometer baseline. However, the image formed on the detector is the convolution of the modified intensity distribution with the PSF of a single aperture. Thus, even for a uniformly emitting, extended object *no fringes are seen*; the convolution averages them out, leaving an image where the maximum resolution is  $\lambda/D$  where  $D$  is the diameter of a single telescope element. Since nulling is sensitive to material as close as  $\lambda/2b$  away, objects can be detected which are within the Airy core of the single element. Because the stellar suppression is not perfect, the signal of a faint companion with a separation of  $< \lambda/D$  is mixed with the residual starlight in a common Airy core.

As suggested by Bracewell (1978), such planetary companions could be most easily detected by modulating their signal through rotation of the interferometer. Rotation of the interferometer would rotate the transmission pattern of equation 2.2. The planetary signal would be modulated by the pattern, separating it from any background, and, through the frequency of its modulation, determining its separation from the star.

The implementation of nulling described in this thesis also makes use of the field about the null, which requires a different optical arrangement from the scheme proposed by Bracewell (Figure 2.1). As can be seen by tracing the beams the images are mirror reflections of one another since one beam undergoes an additional reflection at the semi-transparent mirror. In addition the images are only exactly overlapped along the centerline of the image. Point sources to either side of this line do not overlap and thus do not have their light interfered. This is unattractive for studying extended circumstellar structure. The situation can be avoided by creating an asymmetric system such as one shown in Figure 4.1 or 5.1. Since, in these setups each beam undergoes a number of reflections equal to or different by multiples of two, a true image of the field about the star is formed. This is important for three reasons. First, a system which forms a true image of the field can detect the astrometric offset of the companion, while a symmetric system cannot. Secondly, any complex circumstellar structure studied via a symmetric system has the added difficulty of untangling the two mirror (or rotated in some cases) images of the extended structure. Finally, companions outside the Airy core are not overlapped in a symmetric system and cannot be detected by modulation of their signal through rotation of the interferometer, as suggested by Bracewell (1978).

## 2.2. Achromatic Nulling

In the treatment above a crucial point was not discussed. If we tune the path-length to create a  $180^\circ$  phase difference between the beams we are creating a null at one wavelength only. Wavelengths shorter and longer than this center wavelength will not cancel out perfectly. The phase difference (in waves) is given by

$$\Phi(\lambda) = \frac{\lambda_0}{4\lambda} + \frac{1}{4} \quad (2.3)$$

where  $\lambda_0/4$  is the amount of physical path difference between the beams and the additional  $1/4$  wave achromatic phase shift is added by the semitransparent mirror, as explained in section 3.1. The fraction of light remaining in the focal plane compared to constructive interference, or residual intensity, is given by

$$N(\lambda) = \frac{1 + \cos(\Phi(\lambda))}{2} \quad (2.4)$$

where  $N$  is used to denote that the intensity calculated is the nulled intensity. That is, the amount of light is normalized to the intensity of light at constructive interference. The total light remaining in the nulled image is obtained by integrating equation 2.4 over the bandwidth of observation. The intensity is

$$N_{phase} = \int \frac{1 + \cos(2\pi \left( \frac{\lambda_0}{4\lambda} + \frac{1}{4} \right))}{2} \quad (2.5)$$

which can be integrated numerically over the desired bandwidth to determine the level of residual intensity. At  $10 \mu\text{m}$  a bandwidth narrower than 1.4% is needed to keep the residual intensity below  $10^{-4}$ . Clearly a better approach is needed to create the half-wave phase difference between the beams.

Since Bracewell first suggested the concept, several techniques have been suggested to create an achromatic null. If the electric field vector of one aperture is rotated by 180 degrees the light will interfere destructively, independent of

wavelength. This can be achieved either by rotating the beam the required amount using roof prisms, as suggested by Shao and Colavita (1992), or by sending one of the beams through focus (Gay, Rabbia, and Manghini 1997) before combination. These techniques have the advantage of being able to achieve as wide a bandwidth as required, but the rotation of the electric vector necessarily also rotates the field of one telescope with respect to the other. Any off-axis source will appear as a dual image to either side of the null, creating the same difficulties as the original Bracewell design. The concept proposed by Shao and Colavita (1992) also creates two nulled outputs, adding to the complexity of the setup.

A technique proposed by Angel, Burge, and Woolf (1996) avoids this by use of dielectric materials. The color dependence of phase created by a physical path-length difference is balanced by inserting a dielectric, or glass, material in the opposite beam. By choosing an appropriate thickness for the glass the dispersion will cancel out the dispersion due to the path-length difference, creating a null which is, to first order, achromatic. A second dielectric can be used, if necessary, to achieve higher order achromatism and a broader bandwidth of suppression. The system is designed in the same way an achromatic lens is designed, and is, in this sense, very well understood. This is discussed in more detail in section 3.1. The technique allows the image planes of the two telescopes to be exactly superposed with no relative rotation. In addition, as pointed out by Angel and Woolf (1997), the limited spectral range of the null has the unique advantage that shorter wavelengths are not nulled out. Certain wavelengths have a phase difference of 90 degrees, creating a star image which is halfway between constructive and destructive interference. A change in the relative intensity of the two interferometer outputs for this shorter wavelength signal is a sensitive indicator of a change in phase between the beams and can be used to tune the longer wavelength null.

## CHAPTER 3

### GROUND-BASED NULLING DESIGN AND LIMITATIONS

Nulling was originally proposed as a technique for space-based observations, but is a useful technique for ground-based telescopes, especially in combination with adaptive optics. In fact, both scientifically and technically, nulling systems on ground-based telescopes are important for advancing the search for exo-solar planetary systems. Atmospheric windows in the 8-13  $\mu\text{m}$  range, as well as the 4 and 5  $\mu\text{m}$  regions, have dark enough sky backgrounds to undertake sensitive searches both for exo-solar zodiacal dust and planets (Woolf and Angel 1995, Hinz et al. 1999). This chapter discusses design considerations and constraints I have developed for the ground-based nulling instruments presented later as well as limits to their performance.

The most crucial aspect of a nulling instrument is the semi-transparent mirror which blends the light from the two beams. This optic is referred to in the following as a “beam-splitter”, even though the optic really serves to combine the beams.

### 3.1. Design of a Nulling Beam-splitter

The beam-splitter's role is to mix the two beams so that they have equal intensity over the passband, and to not introduce any wavelength dependent phase shift over the pass band. In addition, to control the null using a shorter wavelength it is necessary to have equal reflection and transmission at this wavelength *and* to have this shorter wavelength correspond to a region of the spectrum at which the atmosphere is transparent.

Since one beam reflects off the beam-splitter while the other is transmitted through it (for a given output) it is important that the design be symmetric. An asymmetric beam-splitter will introduce a wavelength dependent phase shift between the beams.

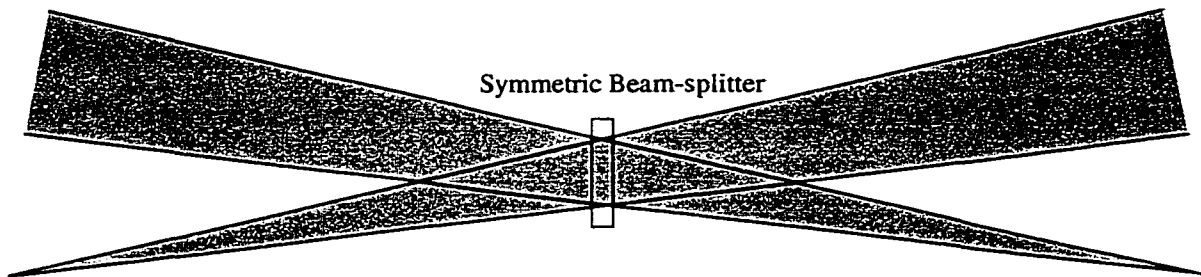


Figure 3.1 A Symmetric Beam-splitter. An achromatic quarter wave phase shift is created by a symmetric beam-splitter between the reflected and transmitted components of the beam. This can be seen by recognizing that the system is symmetric. If the inputs are equal the outputs must also be equal in intensity. Conservation of energy in the total light of the outputs requires that the relative phase shift between the beams be  $1/4$  wave, independent of wavelength.

### 3.1.1. Phase Compensation

A symmetric beam-splitter will provide an achromatic 1/4 wave phase shift between the reflected and transmitted beams. This can be seen by noticing that the two outputs of a symmetric beam-splitter illuminated by light arriving in phase on opposite sides of the optic as shown in Figure 3.1 must be equal. The total energy in both beams must be conserved, requiring that the phase difference between the transmitted and reflected components of each beam must be 1/4 wave, independent of wavelength. This effect has been noted by different groups involved in the design of interferometers (Shao and Colavita 1992, Phillips and Hickey 1995, Angel and Woolf 1997).

The symmetric designs we have developed utilize two plates of the same material held together to create a symmetric thin film stack. The existing beam-splitter substrate and a difference in path between the beams is used to achieve the additional 1/4 wave phase difference required for nulling. The two sides of the beam-splitter can be made with the required thickness difference. The phase difference in waves between the two beams can be written as

$$\Phi(\lambda) = \frac{1}{4} + \frac{p}{\lambda} + \frac{\Delta t n(\lambda)}{\lambda} \quad (3.1)$$

where  $p$  is the path-length difference between the beams,  $n(\lambda)$  is the index of refraction of the substrate, and  $\Delta t$  is the difference in thickness between the two plates. If  $\Delta t$  is set to zero then

$$p = \frac{\lambda_0}{4} \quad (3.2)$$

for destructive interference, but the phase is exactly 1/2 wave only at the center wavelength,  $\lambda_0$ , and is highly chromatic.

The index of refraction of typical materials can be approximated using a



Taylor series expansion so that

$$n(\lambda) \simeq n_0 + n_1(\lambda - \lambda_0) + n_2(\lambda - \lambda_0)^2 + \dots \quad (3.3)$$

where  $n_0$ ,  $n_1$ , and  $n_2$  are the Taylor coefficients about  $\lambda_0$ . Then the phase is given by

$$\Phi(\lambda) = \frac{1}{4} + \frac{p}{\lambda} + \frac{n_0 \Delta t}{\lambda} + n_1 \Delta t - \frac{n_1 \Delta t \lambda_0}{\lambda} + n_2 \Delta t \frac{(\lambda - \lambda_0)^2}{\lambda} + \dots \quad (3.4)$$

To create a half wave achromatic null  $\Delta t$  is set to

$$\Delta t = \frac{1}{4 n_1}. \quad (3.5)$$

If the path-length difference is chosen to cancel out the zero order term, so that

$$p = -\Delta t(\lambda_0 n_1 - n_0) \quad (3.6)$$

then the phase is given by

$$\Phi(\lambda) = \frac{1}{2} + n_2 \Delta t \frac{(\lambda - \lambda_0)^2}{\lambda} + \dots, \quad (3.7)$$

and the null is limited by the second order terms in the index of refraction.

### 3.1.2. Amplitude Matching

Thin film techniques are the standard tools for creating a 50% transmissive optic. In these designs layers of material, which are typically  $1/4$  or  $1/2$  wavelength thick, are built up on a substrate to create an optic with the desired properties. An example of a simple, symmetric beam-splitter is a single material of index of refraction,  $n_2$ ,  $1/4$  wavelength thick at the intended wavelength of observation,  $\lambda_0$ . Each surface reflects a portion of the light. The amplitude of this light from the first interface is

$$r_{12} = \frac{n_2 - n_1}{n_2 + n_1} \quad (3.8)$$

where  $n_1$ , in this case, is one, the index of air. The amplitude of the second interface is

$$r_{23} = \frac{n_1 - n_2}{n_2 + n_1} \quad (3.9)$$

If the thickness of the material is given by

$$h = \frac{\lambda_0}{4} \quad (3.10)$$

and we define the quantity

$$\beta = 2\pi \frac{n_2 h}{\lambda} \quad (3.11)$$

then the total reflected intensity for the interference of these two amplitudes is given by Born and Wolf (1993) as

$$r_{tot} = \frac{r_{12} + r_{23}e^{2i\beta}}{1 + r_{12}r_{23}e^{2i\beta}}. \quad (3.12)$$

The reflected intensity for the optic is

$$R = |r|^2 = \frac{r_{12}^2 + r_{23}^2 + 2r_{12}r_{23}\cos(2\beta)}{1 + r_{12}^2r_{23}^2 + 2r_{12}r_{23}\cos(2\beta)}. \quad (3.13)$$

From the equations above it can be shown that if the desired reflected intensity is 50% an index of 2.41 is needed for the glass. Several infrared transmitting materials have indices in this range, including Zinc Selenide (ZnSe) and Potassium-Thallium Bromide (KRS-5).

Although it is not possible to create a beam-splitter which is a  $1/4$  wavelength thick at  $10 \mu\text{m}$ , it is possible to invert the materials. That is, an air gap  $1/4$  wavelength thick with appropriate glass to either side has the same properties. The ratio of the two outputs is only equal for the design wavelength. However, the spectral response is broad enough (as shown in Figure 3.2) for reasonable performance over the desired range. This is discussed in more detail in section 3.3. If broader spectral coverage is required the same general design can be used

by making a thin film stack with more layers. For example, a  $1/2$  wave layer of material with an index of  $\simeq 2.48$  on the inside of each plate with an air gap of  $1/4$  wave between them would yield a symmetric beam-splitter with a flatter spectral response than the simple air gap.

Figures 3.2 and 3.3 present solutions to the above equations using Zinc Selenide as the beam-splitter material. The plots show the reflected intensity and phase difference as a function of wavelength for beam-splitters designed for use at 11 and 5  $\mu\text{m}$  respectively.

### 3.2. Control of the Null

As mentioned above, an advantage of the dielectric approach to nulling is the ability to adaptively control the null using shorter wavelength light. Since this method of achieving a null is only “pseudo-achromatic”, that is, achromatic only over the science passband, it is possible for the shorter wavelength light to have a phase difference between the beams which is markedly different from half of a wave. The wavelength at which the sensing is done depends on the variation of phase with wavelength as described by equation 3.1 above. A suitable material must be chosen which creates a  $1/4$  or  $3/4$  wave phase shift, corresponding to light which is halfway between constructive and destructive interference for both outputs of the beam-splitter, at a wavelength where the atmosphere is transparent. The beam-splitter design, then, must also provide  $\simeq 50\%$  reflectivity at this wavelength to suitably mix the input. Zinc Selenide, using only a  $1/4$  wave air gap as the film stack, turns out to be suitable for both the 11 and 5  $\mu\text{m}$  windows. As can be seen in Figure 3.2 the design of the 11  $\mu\text{m}$  beam-splitter provides for a  $3/4$  wave phase shift at 2.2  $\mu\text{m}$  (the middle of the K atmospheric window) when it is  $1/2$

wave at  $11\text{ }\mu\text{m}$ . Although the  $5\text{ }\mu\text{m}$  beam-splitter's phase-sensing is not as well centered on an atmospheric window, its phase reaches  $1/4$  wave for the long end of the H atmospheric window ( $1.7\text{--}1.8\text{ }\mu\text{m}$ ). Any variation in path-length between the two arms will be detected by the image in one output getting dimmer while

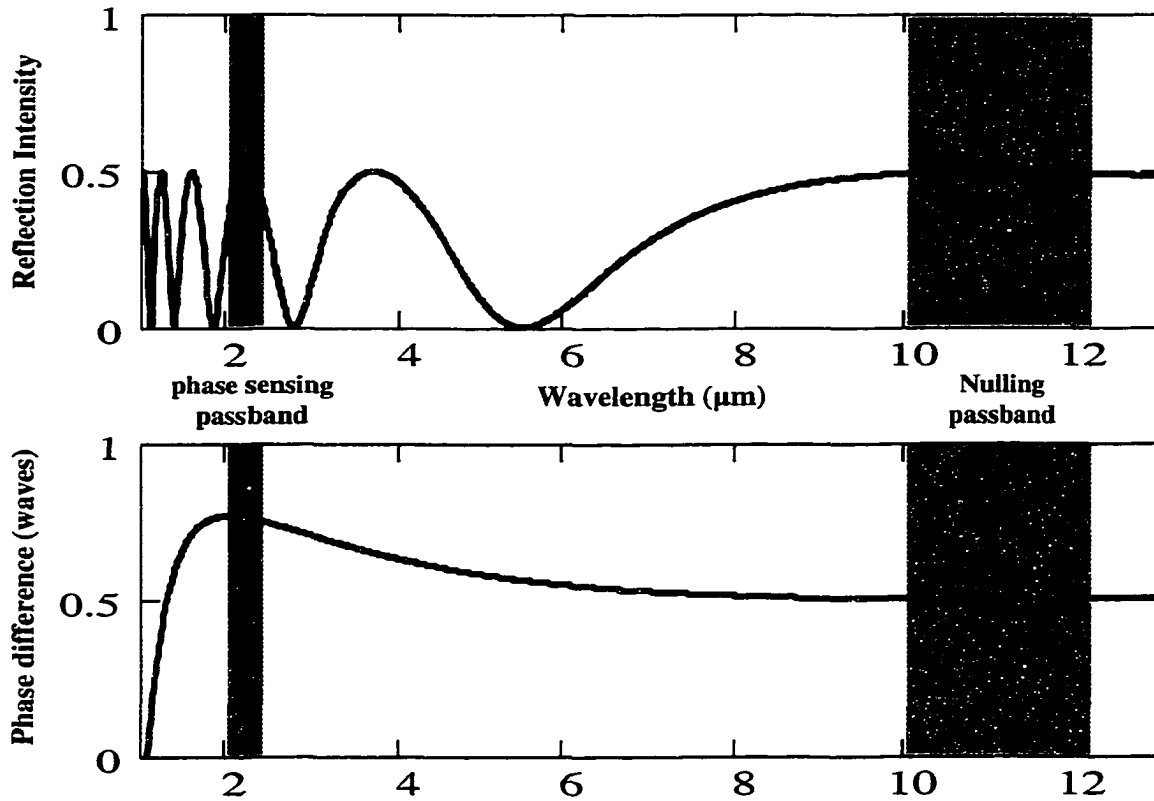


Figure 3.2 Plot of reflection intensity and phase difference for an  $11\text{ }\mu\text{m}$  symmetric beam-splitter. The beam-splitter is composed of two plates of ZnSe separated by  $2.7\text{ }\mu\text{m}$  and having a thickness difference of  $39\text{ }\mu\text{m}$ . The two shaded areas correspond to the passband for nulling and the passband for sensing phase between the two apertures.

the image in the other output gets brighter. For example, using equation 2.4, one can calculate that a null of  $3 \times 10^{-5}$  at  $11 \mu\text{m}$  corresponds to a path variation of 0.02 microns, or 0.01 waves at  $2 \mu\text{m}$ . If the brightness ratio is 1 at  $2 \mu\text{m}$  for the best null such an error would give a ratio of 88% between the images, a differential

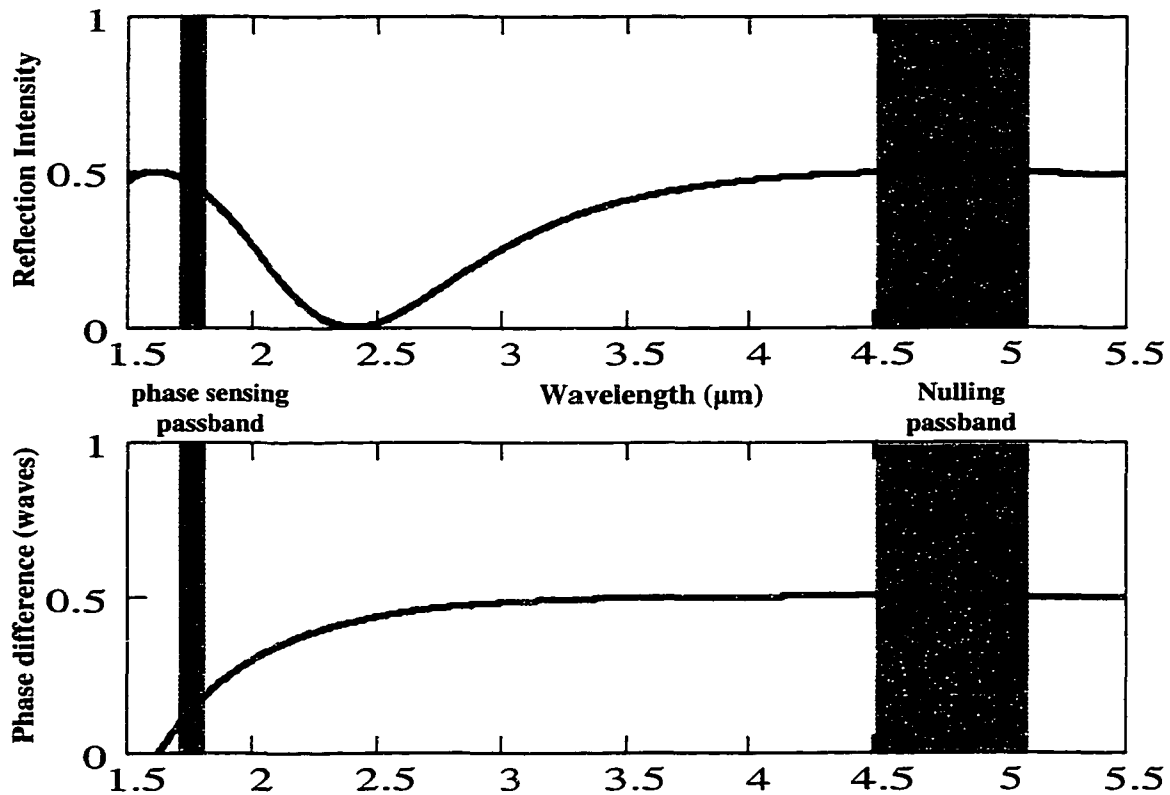


Figure 3.3 Plot of reflection intensity and phase difference for a  $5 \mu\text{m}$  symmetric beam-splitter. The beam-splitter is composed of two ZnSe plates separated by  $1.2 \mu\text{m}$  and having a thickness difference of  $70 \mu\text{m}$ . The two shaded areas correspond to the passband for nulling and the passband for sensing phase between the two apertures.

signal that would be easy to detect for a bright star. It is important to understand that this phase-sensing technique is completely common path with the nulled light, does not degrade the signal-to-noise ratio of the nulled light, and is unique to the pseudo-achromatic way of achieving the null.

This technique can also be applied to make the same phase difference measurements in detail across the interfered aperture. If an image of the pupil is formed on a  $2\text{ }\mu\text{m}$  detector for both outputs, the relative flux can be measured in many places across the pupil. This information can then be used to fine-tune an adaptive optics system correcting the stellar wavefront.

### **3.3. Limitations to Nulling**

Although light from a star can be dramatically suppressed with nulling, there are limitations, both intrinsic and imposed by a given design, which prevent perfect cancellation. This section presents the main contributions to residual light in nulling interferometry. These calculations are then applied in chapters 4 and 5 to the designs of the nulling interferometers presented.

#### **3.3.1. Phase vs. Wavelength**

As discussed above, the phase variation over the passband of observation needs to be carefully controlled to avoid introducing residual light from wavelengths not cancelling out near the edge of the passband. This effect is determined by the index of refraction of the glass used for dispersion compensation as well as how precisely we are able to control the difference in thickness between the plates.

Zinc Selenide is a good material for use as dispersion compensation as well as being suitable for use as a beam-splitter, as described in section 3.1.2. It is

a standard optical material in infrared instruments and can be polished to high precision. In terms of the Taylor series, equation 3.4, ZnSe's coefficients at 11  $\mu\text{m}$  at 77 degrees K are

$$\begin{aligned} n_0 &= 2.388 \\ n_1 &= -6.35 \times 10^{-3} \mu\text{m}^{-1} \\ n_2 &= -2.84 \times 10^{-4} \mu\text{m}^{-2} \end{aligned}$$

Using equation 3.5 the thickness difference should be 39.4  $\mu\text{m}$ . Figure 3.2 shows the phase versus wavelength for this thickness difference and the appropriate amount of path-length difference, determined by equation 3.1. Using this curve the residual intensity is determined by integrating over the passband using the equation

$$N_{phase} = \int_{\lambda_0 - \Delta\lambda/2}^{\lambda_0 + \Delta\lambda/2} \frac{1 + \cos(\Phi(\lambda))}{2\Delta\lambda} d\lambda \quad (3.14)$$

where  $\lambda_0$  is the central wavelength and  $\Delta\lambda$  is the bandwidth. The phase and residual intensity of the null are shown in Figure 3.4 for no compensation (solid line) and for compensation with ZnSe (dotted line). For the dielectric technique the phase is exactly matched at only a discrete number of wavelengths. A tradeoff can be made between the breadth and the depth of the null by tuning the free parameters, the path difference and the thickness difference of the dielectric. The level of null required determines the achievable bandwidth for the system for the dielectric technique. For the solution above using ZnSe a null of 50,000 would limit the bandwidth to 38% at 11  $\mu\text{m}$ .

In designing a beam-splitter for the nulling instrument described in chapter 5 it was realized that glasses typically have an inflection point in their index of refraction curve at a given wavelength. In other words, at a particular wavelength

the second order term in the index equation is zero, leaving only the higher order terms to affect the achromaticity of the null. Although no suitable materials exist with an inflection point at 10  $\mu\text{m}$ , ZnSe has its inflection point at 4.8  $\mu\text{m}$  so that in this region the nulling passband can be extended from 2.9-6.7  $\mu\text{m}$  for a 50,000 null, as shown in Figure 3.5.

At 4.8  $\mu\text{m}$  the coefficients for ZnSe's index of refraction are

$$\begin{aligned} n_0 &= 2.417 \\ n_1 &= -3.6 \times 10^{-3} \mu\text{m}^{-1} \\ n_2 &= -1.47 \times 10^{-6} \mu\text{m}^{-2} \end{aligned}$$

which, using equation 3.5, gives a thickness difference of 69.8  $\mu\text{m}$ . Since the second order term is a factor of 200 smaller than at 11  $\mu\text{m}$  the phase compensation works over a broader range of wavelengths.

### 3.3.2. Intensity vs. Wavelength

Intensity variations over the passband are introduced by the wavelength dependence of the beam-splitter. If one beam is a fraction,  $I_f$ , the intensity of the other, then the residual intensity of this effect is given by

$$N_a(\lambda) = \left( \frac{1 - \sqrt{I_f(\lambda)}}{1 + \sqrt{I_f(\lambda)}} \right)^2 \quad (3.15)$$

Using equation 3.13  $I_f$  is

$$I_f(\lambda) = \frac{R(\lambda)}{1 - R(\lambda)} \quad (3.16)$$

which is valid if the beam-splitter is dielectric, and thus does not absorb any of the radiation. Then the total residual intensity from amplitude variations of the



beam-splitter is given by

$$N_{amp} = \int_{\lambda_0 - \frac{\Delta\lambda}{2}}^{\lambda_0 + \frac{\Delta\lambda}{2}} \frac{N_a(\lambda)}{\Delta\lambda} d\lambda. \quad (3.17)$$

If the edge of the passband is to transmit  $< 10^{-4}$  then using the equations above the reflectivity of the beam-splitter is constrained to be  $50 \pm 1\%$  over these wavelengths as is the case for the curve in Figure 3.2 over the range  $9.7\text{-}13 \mu\text{m}$ .

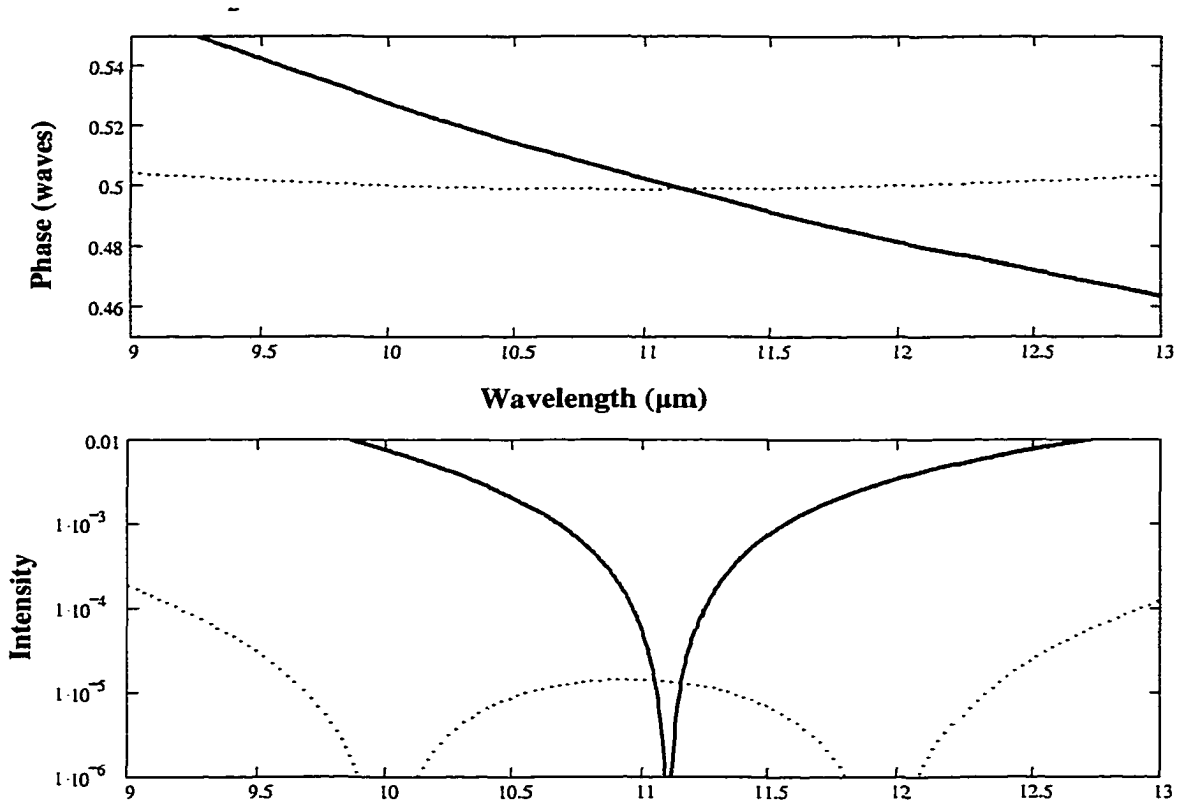


Figure 3.4 Phase variation and residual intensity for an  $11 \mu\text{m}$  beam-splitter. The traces are for nulls created by path-length difference only (solid line), and with ZnSe used for dispersion compensation (dotted line).

### 3.3.3. Polarization Effects

Differences in polarization of the two beams arise from any differences in angles of incidence on the optics between the two arms. The most sensitive optic to this

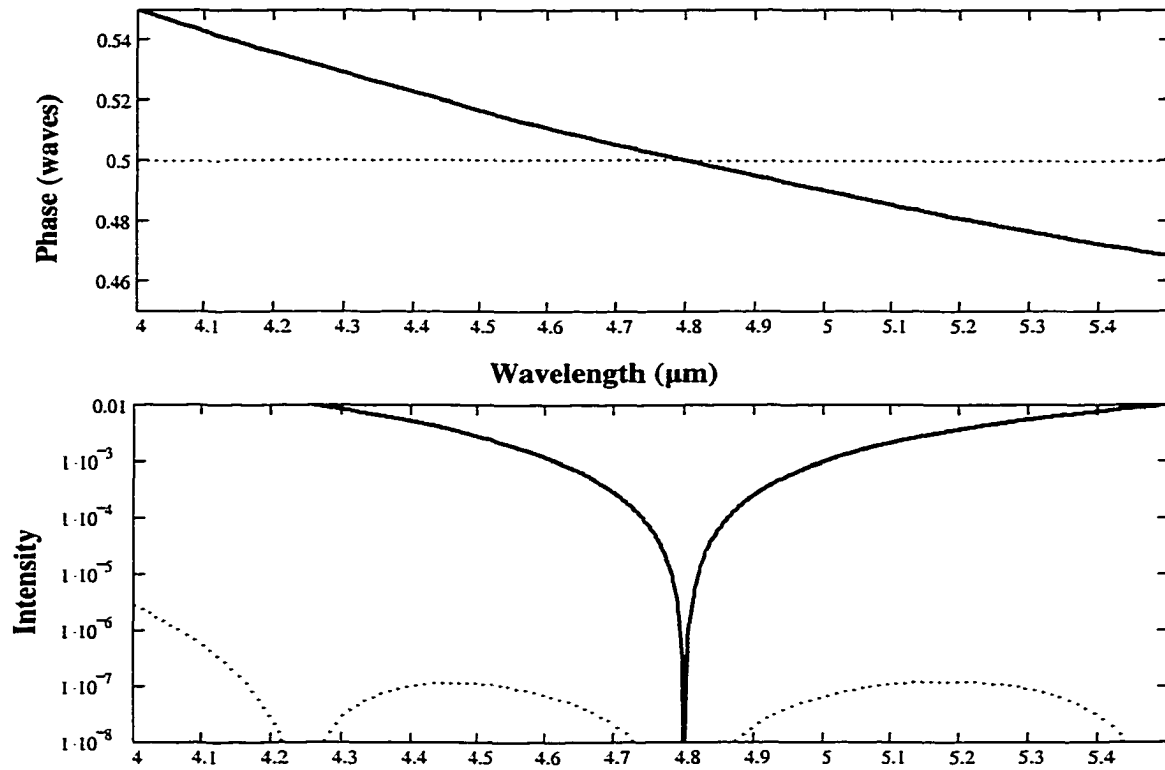


Figure 3.5 Phase variation and residual intensity for a 5  $\mu\text{m}$  beam-splitter. The traces are for nulls created by path-length difference only (solid line), and with ZnSe used for dispersion compensation (dotted line). Note the broader level of suppression compared to Figure 3.4 from the second order term being smaller at 5  $\mu\text{m}$ .

effect is the beam-splitter, but there can also be contributions from corresponding mirrors having different angles of incidence and from the optical trains not being limited to two dimensions.

### *Beam-splitter Polarization*

Since the beam-splitter is not reflecting the light at normal incidence the amplitudes of reflection from each sense of polarization are slightly different. Although this effect is essentially wavelength-independent, for a given wavelength it is not possible to match the amplitudes for both senses of polarization since the polarization in the plane of incidence reflects slightly more than the sense perpendicular to the plane of incidence. Generalizing the Fresnel equations, as given by Born and Wolf (1993), for non-normal incidence, the amplitudes from each interface are given by

$$r_{12} = \frac{p_2 - p_1}{p_2 + p_1} \quad (3.18)$$

and

$$r_{23} = \frac{p_1 - p_2}{p_2 + p_1} \quad (3.19)$$

where

$$p_i = n_i \cos(\theta) \quad (3.20)$$

for light polarized perpendicular to the plane of incidence and

$$p_i = \frac{\cos(\theta)}{n_i} \quad (3.21)$$

for light polarized parallel to the plane of incidence where  $\theta$  is the angle of incidence.

Then if the thickness of the material is given by

$$h = \frac{\lambda_0}{4 \cos(\theta)}, \quad (3.22)$$

and we define the quantity

$$\beta = 2\pi \frac{n_2 h \cos(\theta)}{\lambda} \quad (3.23)$$

the total reflected intensity for the interference of these two amplitudes is given as

$$r_{tot} = \frac{r_{12} + r_{23}e^{2i\beta}}{1 + r_{12}r_{23}e^{2i\beta}}. \quad (3.24)$$

The reflected intensity for the optic is

$$R = |r|^2 = \frac{r_{12}^2 + r_{23}^2 + 2r_{12}r_{23}\cos(2\beta)}{1 + r_{12}^2r_{23}^2 + 2r_{12}r_{23}\cos(2\beta)}. \quad (3.25)$$

The reflection intensities for each sense of polarization ( $R_{\parallel}$  and  $R_{\perp}$ ) can be calculated using this equation. Then, setting the average reflection intensity to 50%, the average intensity mismatch for both senses of polarization is

$$I_{pol} = 1 - 2(R_{\parallel} - R_{\perp}) \quad (3.26)$$

and the residual intensity from this effect can be calculated using equation 3.15 above. The level at which polarization affects the achievable level of null is a dramatic function of the angle of incidence. For example, if a suppression level of  $> 10^4$  is desired, the angle of incidence of the beam-splitter needs to be  $< 10$  degrees, using the equations above. This is an important constraint on the design of any single-pass nulling instrument.

### *Different Angles of Incidence*

Typically, several relay mirrors are used in each arm of the interferometer to bring the beams into coincidence. If the angle of incidence for corresponding mirrors in the two beams differs by large amounts the phase shift is different for each sense of polarization. This error is only noticeable for large ( $>40$  degrees)

differences in angles of incidence, as calculated by Born and Wolf (1993), for typical metal reflectors. For the designs presented later this error is made negligible by ensuring that all reflections are matched to within several degrees. For longer baseline interferometers with many reflections this phase difference for each sense of polarization must be considered to avoid degrading the null.

### *Out-of-Plane Reflections*

It is often the case for interferometers that the plane of incidence of the optical train of one arm is not coincident, but is rotated with respect to the plane of incidence of the other arm. It is even possible with longer baseline interferometers to have the plane of incidence vary from mirror to mirror in one arm. For oblique reflection this can lead to significant residual intensity from phase variations of the different senses of polarization. This effect can be calculated for a given configuration, but the designs presented in this thesis avoid this entirely by keeping all the optics in the same plane.

### **3.3.4. Diameter of the Star**

The most fundamental limit to nulling observations is that imposed by the target star. If the star is not sufficiently point-like some light will “leak” around the edges of the null providing residual intensity in the focal plane. The total leak is found by integrating the fraction of light transmitted at each angle over the angular diameter of the star. For nearby main sequence stars typical angular diameters are 1-3 milliarcseconds (mas). The fraction of light transmitted for a star of uniform brightness across its disk,  $S$  radians in diameter, is determined by integrating equation 2.2 over the angular diameter of the star. Although stellar discs appear

significantly limb darkened in the visible, infrared observations have suggested that the assumption of uniform brightness is approximately correct (Bester et al. 1996).

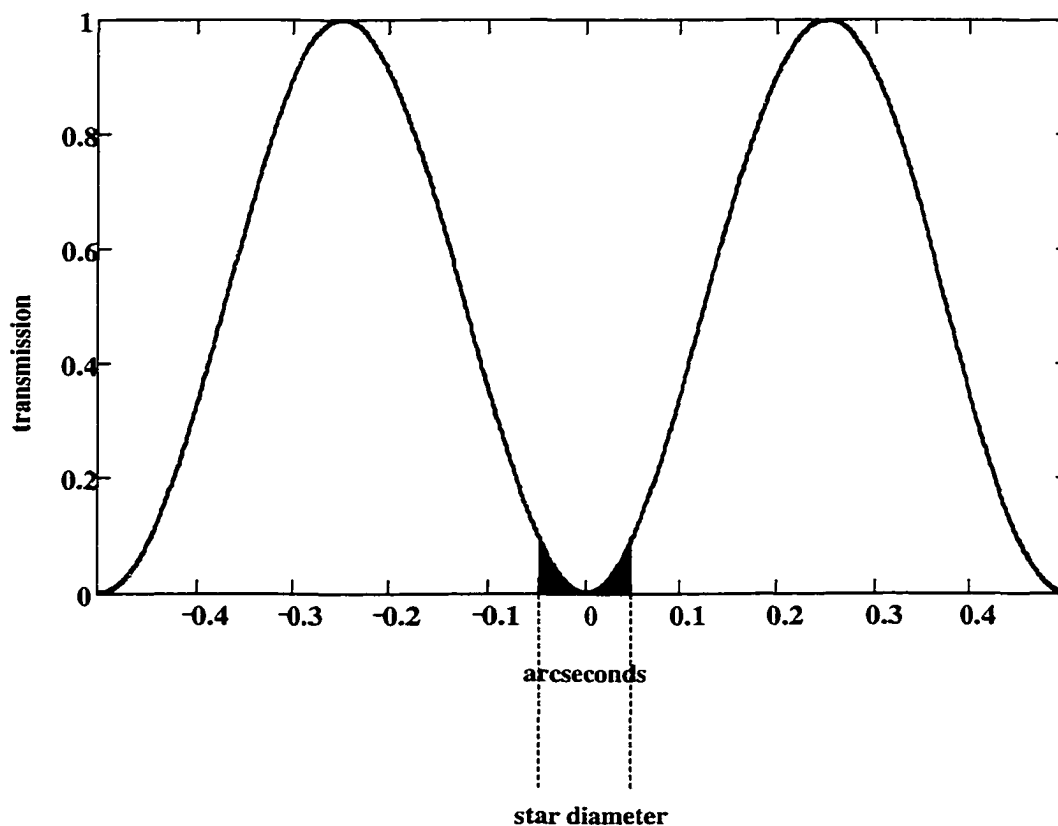


Figure 3.6 Residual intensity from a finite stellar diameter. Since the star is not a true point source some of its light “leaks” around the edges of the null. The star’s diameter is exaggerated to illustrate the effect. Typical nearby main sequence star diameters correspond to  $\sim 1$  mas. The fringe pattern is shown for the MMT interferometer operating at  $10\ \mu\text{m}$ .

The total leak is given by

$$N_{star} = \frac{1}{\pi S^2} \int_0^{S/2} \int_0^{\sqrt{S/2^2 - y^2}} \sin^2 \left( \frac{\pi x b}{\lambda} \right) dx dy \quad (3.27)$$

Since the angle subtended by the star is small compared to the fringe spacing we can use the small angle approximation to write

$$N_{star} = \frac{1}{\pi S^2} \int_0^{S/2} \int_0^{\sqrt{S/2^2 - y^2}} \left( \frac{x \pi b}{\lambda} \right)^2 dx dy \quad (3.28)$$

which can be integrated to obtain the expression

$$N_{star} = \frac{\pi^2}{16} \left( \frac{S}{\lambda/b} \right)^2 \quad (3.29)$$

where  $b$  is the baseline between apertures and  $\lambda$  is the wavelength of observation.

As discussed by Bracewell (1978), the contribution from the star's diameter is a function of the square of the interferometer baseline. Thus for nulling the choice of baseline is a tradeoff between higher spatial sensitivity and poorer levels of suppression.

### 3.3.5. Atmospheric Turbulence

In addition to the above limitations which apply to any nulling interferometer, turbulence in the atmosphere affects the level of suppression possible, posing perhaps the most difficult limit to overcome in ground-based nulling. The application of adaptive optics to nulling has different performance requirements from normal wavefront correction. However, the bright on-axis star provides dramatically more wavefront sensing capability to provide fast, high spatial density correction as discussed by Angel (1994).

### *Nulling with No Wavefront Correction*

For telescope observations without any wavefront correction the suppression level is set by the atmospheric turbulence rather than any of the above quantities. Suppressed images are obtained by taking short exposure images, typically 0.05-0.5 s in length, depending on the quality of seeing. The variation in phase difference between the apertures can be approximated using the structure function for Kolmogorov turbulence,

$$D(r) = 6.88 \left( \frac{r}{r_0} \right)^{5/3}, \quad (3.30)$$

which gives a phase variation in waves for two points separated by a distance,  $r$ , of

$$\Delta\Phi = 0.417 \left( \frac{r}{r_0} \right)^{5/6} \quad (3.31)$$

where  $r_0$  is the coherence length of the turbulence. This variation is large enough that, essentially, the phase difference can be considered to be uniformly distributed over  $2\pi$  radians or one wave. If a number of frames is taken to capture a best null the best residual intensity can be expected to be off from half a wave by

$$\Delta\Phi_{best} \simeq \pi/f \quad (3.32)$$

where  $f$  is the number of frames recorded. The residual intensity is calculated using equation 2.4.

The sampling error is negligible compared to two other errors, the change in phase over the exposure time and higher order phase variations within each pupil. The change in phase between the apertures over the exposure time  $t$  can be approximated using

$$\Delta\Phi_{time} = \sqrt{2} \left( \frac{t}{t_0} \right)^{5/6} \quad (3.33)$$



The coherence time of the atmosphere,  $t_0$ , is given by

$$t_0 = \frac{r_0}{v_w} \quad (3.34)$$

where  $v_w$  is the turbulence weighted wind speed, typically 15-25 m/s. By integrating over this phase change, using equation 2.4, we obtain

$$N_t = \int_{\frac{-\Delta\Phi_{time}}{2}}^{\frac{-\Delta\Phi_{time}}{2}} \frac{1 + \cos(\pi + \Phi)d\Phi}{2} \quad (3.35)$$

which determines the residual intensity due to this effect. The phase variation within an aperture using Kolmogorov turbulence is given in Beckers (1993). The RMS phase variation (in waves) within an aperture is approximately

$$\Delta\Phi_{high} = 0.053 \left( \frac{D}{r_0} \right)^{5/6} \quad (3.36)$$

if tip and tilt errors across the aperture are not present, as is true for the best overlapped and nulled images. For well nulled images where the images are properly overlapped the expected RMS phase error *between* the two apertures is approximately  $\sqrt{2}$  times equation 3.36 so that the residual intensity from this effect is

$$N_{high} = \frac{1 - \cos(2\pi \Delta\Phi_{high} \sqrt{2})}{2}. \quad (3.37)$$

These two values determine the achievable level of suppression without any adaptive optics correction. If the phase is adaptively controlled between the apertures the time variation effect becomes negligible, leaving only the higher order aberrations to limit the suppression. If  $r_0$  is chosen to be 5 m and  $t_0$  is 0.1 s at 10  $\mu\text{m}$ , typical values for average seeing, then the time variations for a 0.1 s exposure time give a mean residual of 4% and the higher order errors contribute 2%.

### *Adaptive Optics*

More precise suppression is possible with the use of adaptive optics to correct the phase errors in the incoming wavefront. Sandler et al (1994) provide a detailed analysis of the expected performance of an adaptive optics system in the presence of atmospheric turbulence. For the situation of an on-axis bright star two errors dominate the performance of the AO system: the system's ability to fit the wavefront variations and the temporal latency of the system. For high levels of suppression sources of error must also be included from sensing the wavefront at a different wavelength than observations and instantaneous variations in wavefront correction between the apertures.

For these sources of error the important number is one minus the Strehl ratio, which gives the fraction of the light not properly suppressed. How this light affects the level of null depends on the source of the error.

The extended Marechal approximation allows us to calculate directly the Strehl ratio for a given RMS wavefront error,  $\sigma$ , expressed in radians. It is given as

$$S = e^{-\sigma^2}. \quad (3.38)$$

### *Fitting Error*

The wavefront error (in radians) due to a finite number of corrector elements in the deformable mirror (DM), according to Hardy(1998), is given by

$$\sigma_{fit} = 0.55 \left( \frac{s}{r_0} \right)^{5/6} \quad (3.39)$$

where  $s$  is the projected inter-actuator spacing and the coefficient, given as 0.53-0.58 by Hardy, is relevant for a continuous plate deformable mirror.

The errors due to the fitting of the wavefront are uncorrelated over spatial sizes larger than the actuator spacing. This results in the residual light,  $(1-S)$ , being spread out into a halo determined by the size of the interactuator spacing,  $s$ . If the residual light is spread into a disk  $\lambda/s$  in diameter while the Airy core is  $\lambda/D$ , the level of the residual light in the Airy core from the fitting error is

$$N_{fit} = \frac{1 - S_{fit}}{2} \left( \frac{s}{D} \right)^2 \quad (3.40)$$

where  $S_{fit}$  is the Strehl ratio associated with the wavefront error from equation 3.39.

#### *Error from Number of Modes Corrected*

In reality the AO system is often limited by the number of Zernike modes that it is capable of sensing and correcting rather than the number of actuators in the DM. If the number of Zernike modes corrected is greater than 10, Beckers (1993) gives the wavefront error as

$$\sigma_{mode} = \sqrt{0.2944 J^{\frac{\sqrt{3}}{2}} \left( \frac{D}{r_0(\lambda)} \right)^{\frac{5}{3}}} \quad (3.41)$$

where  $J$  is the number of corrected Zernike modes. The halo size of the uncorrected light is determined, not by the inter-actuator spacing but by

$$s_{eff} = \sqrt{\frac{\pi D^2}{4 J}}. \quad (3.42)$$

Then the level of suppression from  $J$  corrected modes is given by

$$N_{mode} = \frac{1 - S_{mode}}{2} \left( \frac{s_{eff}}{D} \right)^2. \quad (3.43)$$

This error source is relevant when the number of modes corrected is significantly less than the degrees of freedom in the DM. In this case the fitting error is not relevant since it is included in the modal error estimate.

### *Visible Wavefront Sensing Errors*

If the nulling observations are taken at 11  $\mu\text{m}$  there is a significant difference between the observation wavelength and the wavefront sensing wavelength, typically done in the visible part of the spectrum. Atmospheric dispersion between these wavelengths causes the wavefront sensor to not measure the same column of air. Effectively, the visible and infrared light appear to be two images separated, according to Allen (2000), by an angle, expressed in arcseconds, of

$$\theta_\lambda = 1.38 \tan z \quad (3.44)$$

where 1.38 is the differential amount of refraction between 0.5 and 11  $\mu\text{m}$  and  $z$  is the zenith angle. The RMS wavefront error can be estimated by assuming this effect is similar to anisoplanatism in adaptive optics so that the error, in radians, is

$$\sigma_\theta = \left( \frac{\theta}{\theta_0} \right)^{\frac{5}{6}} \quad (3.45)$$

where  $\theta_0$  is the isoplanatic angle at the science wavelength given by

$$\theta_0 = 0.314 \cos z^{\frac{8}{5}} \frac{r_0}{h} \quad (3.46)$$

where  $h/\cos(z)$  is the mean turbulence height (typically 5 km at zenith). This error is an overestimate since the images are not intrinsically separated on the sky and thus the beams are actually more overlapped as they pass through the atmosphere than this calculation assumes. In addition measurements of this effect (Libengood et al. 1999) have suggested that the actual difference is up to a factor of four

smaller due to poorly determined dispersion of the atmosphere. The contribution from this error is summed in quadrature with the error due to the modes corrected so that the total error is

$$\sigma_{total} = \sqrt{\sigma_{mode}^2 + \sigma_{\theta}^2} \quad (3.47)$$

and the suppression level is determined by equation 3.38.

Although the dispersion between wavelengths is significant for visible sensing, it is dramatically better at  $2 \mu\text{m}$ , where the coefficient in equation 3.44 is only 0.08, essentially negligible. The differential wavefront sensing, discussed in chapter 2, would thus also be useful in tuning the wavefront to eliminate this source of error which is significant for larger zenith angles.

### *Temporal Latency Error*

Errors in the wavefront are also introduced by having a latency between sensing and correction of the wavefront. The temporal latency error (in radians), according to Sandler et al (1994), is given by

$$\sigma_{time} = \left( \frac{\Delta t}{t_0} \right)^{5/6} \quad (3.48)$$

where  $\Delta t$  is the time between sensing and correction, typically comparable to the integration time of the wavefront sensor. The coherence time of the atmosphere,  $t_0$ , is given by equation 3.34.

In contrast to the fitting error, the servo lag creates wavefront errors over all spatial scales. For atmospheric turbulence the power in large spatial scales dominates over smaller scales. Because of this it is reasonable to assume that the residual light from a servo lag will be concentrated on a similar angular scale to the

Airy core. Then the residual intensity is simply

$$N_{time} = \frac{1 - S_{time}}{2}. \quad (3.49)$$

The factor of two in equations 3.40 and 3.50 arises from the fact that the light which is not suppressed is not correlated between the two apertures and thus averages out to half the intensity of the interfered light.

Since the residual light from the servo lag is not spread out over larger spatial scales the allowable tolerance in wavefront error from this effect is much smaller.

### *Differences in Strehl Between Apertures*

If the RMS wavefront error is appreciably different between the two apertures the intensity of the light in the Airy core from the two beams will not match, leading to an error similar to section 3.3.2 above. By calculating the intensity mismatch,

$$I_{diff} = \frac{S_A}{S_B} \quad (3.50)$$

where  $S_A$  and  $S_B$  are the Strehl ratios from each aperture, we can use equation 3.15 to estimate the residual intensity from this error. For the high Strehl ratios expected at 10  $\mu\text{m}$ , the variations are expected to be significantly smaller than is needed to achieve a  $10^4$  null, but this limit will determine how variable the seeing can be on a night of marginal seeing before nulling is affected.

## CHAPTER 4

### A PROTOTYPE NULLING INTERFEROMETER WITH THE OLD MULTIPLE MIRROR TELESCOPE

Although nulling interferometry, as a proposed concept, had become accepted following the initial suggestion by Bracewell (1978) and refinements to be able to detect Earth-like planets by Angel and Woolf (1997), no demonstrations of the technique beyond laboratory interference had been attempted. This chapter presents the first telescope demonstration of the technique using a prototype instrument on the original Multiple Mirror Telescope (MMT).

The original MMT was an ideally suited testbed for nulling, with individual 1.8 m telescopes arranged on a 5 m diameter circle. The nulling interferometer was able to be mounted conveniently at the combined focus of the telescope and use two oppositely spaced telescopes to test the concept.

#### 4.1. Optical Layout

The telescopes are co-mounted on a rigid frame pointed at the star, eliminating the need of variable delay lines for path equalization found in interferometers using separately mounted telescopes. A schematic drawing of the instrument is shown

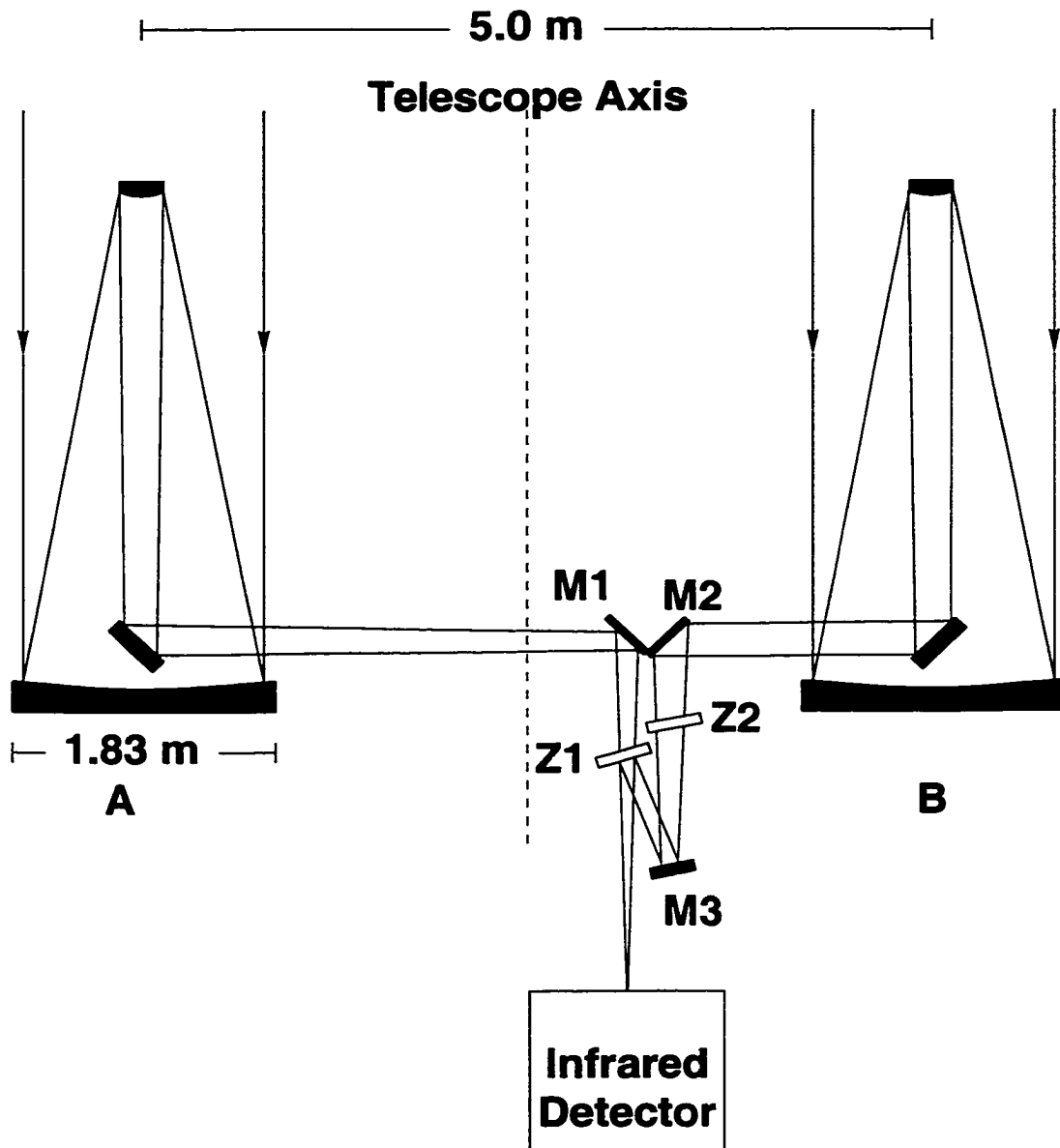


Figure 4.1 Optical layout of the prototype nulling interferometer at the MMT. The instrument is offset from the centerline of the telescope to combine the beams with as few reflections as possible.



in Figure 4.1. The small number of reflections results in low thermal emission. The interferometer is designed to combine the beams after as few reflections as possible, consistent with preserving the relative image orientation. Unmatched reflections are made at nearly normal incidence to minimize polarization differences as described in chapter 3. The  $f/31$  folded Cassegrain beams are combined at a Zinc Selenide beam-splitter, Z1, coated for equal transmission and reflection in the 8-13  $\mu\text{m}$  band. Beam A, after crossing the axis of the telescope, is folded down at M1, and is transmitted by the beam-splitter before coming to a focus. Beam B is folded downward at M2 before reaching the axis of the telescope, through zinc selenide plate Z2 and back up at M3 to equalize the path-lengths before being reflected from the underside of the beam-splitter. Achromatic  $180^\circ$  phase difference is realized by balancing a slight difference in air path with a 40  $\mu\text{m}$  path difference between the two zinc selenide elements, obtained by slight rotation of Z2. The residual chromatic error results in transmission ideally 0.008% over the band 8-12  $\mu\text{m}$ , as calculated using equation 3.14 and shown in Figure 3.4. In practice, the null is limited by atmospheric turbulence at a much higher level. The central null is initially found by translating the beam-splitter vertically, with occasional subsequent small adjustments to correct for flexure. Image detection is made with the Rockwell (now Boeing)  $128 \times 128$  arsenic-doped silicon BIB array of the Mid-infrared Array Camera, MIRAC2 (Hoffmann et al 1998). An internal cold stop limits the effective apertures of the telescopes to 1.6 m, for a diffraction limited image width of 1.5 arcsec.

For a 5 m interferometer at 10  $\mu\text{m}$  wavelength the fringe spacing on the sky is 0.4 arcsec, and full constructive interference for a source is only 0.2 arcsec from the nulled star (equation 2.2).

## 4.2. Observations

Figure 4.2 shows the instrument mounted at the central combining area of the six mirror MMT. In operation, the  $10\text{ }\mu\text{m}$  combined image is observed live on a

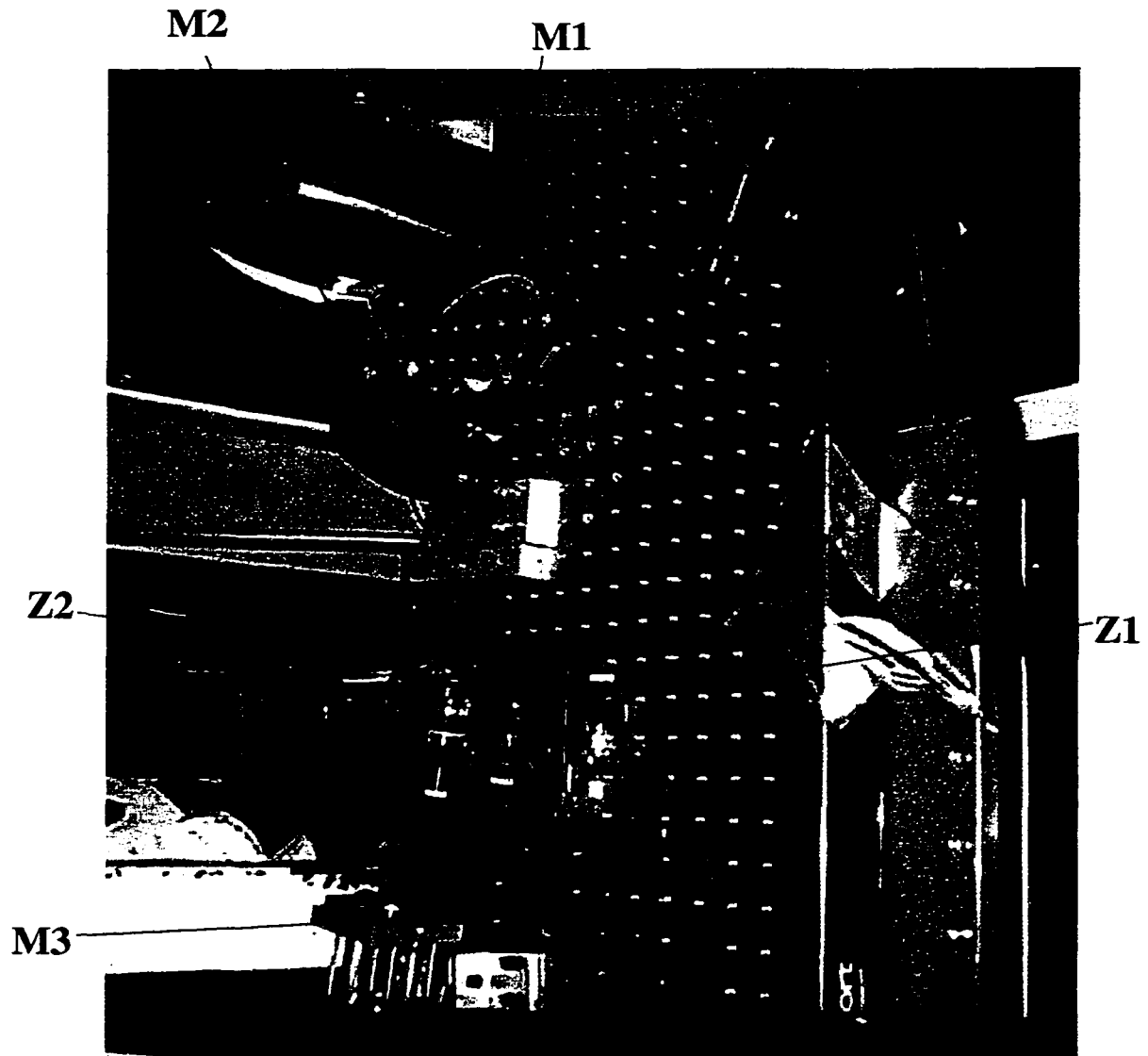


Figure 4.2 Prototype nulling instrument mounted at the central combining area of the MMT.

computer monitor while the beam-splitter is translated to adjust path-length. The star intensity remains steady until the path-lengths are nearly equal, when it is seen to flicker as shown in Figure 4.3. This is caused by atmospheric turbulence which induces relative path-length changes of  $> \pm 5 \mu\text{m}$ , enough to shift the interference randomly between constructive and destructive states relative to its non-interfered flux. The minima are deepest when the average phase difference between the wavefronts is 180 degrees and the average slopes are the same (that is, the individual images are coincident). The flux vs. time from a typical series of frames is shown in Figure 4.3. Each point is a 50 ms exposure of the star  $\alpha$  Tauri with essentially no delay between frames.

Figure 4.4a shows the brightest and faintest snapshot images of the star  $\alpha$  Tauri, which is unresolved at the MMT baseline. The characteristic of the interferometer to cause the entire stellar Airy pattern to disappear is clearly shown. The right hand nulled image has a peak intensity 4.0% and a total integrated flux of 6.0% that of the left-hand constructive image. This small residue arises because phase and tilt differences between the beams are not ideal or stable in even the best nulled exposure, and because higher-order atmospheric aberrations remain uncorrected. But already from this single, short exposure we can deduce that there are no companions lying in the constructive fringes as close as 0.2 arcsec from the star, to a level 3.5 magnitudes (25 times) fainter than the star. Weather did not allow observations through the night for rotated baseline orientation, as prescribed by Bracewell; combination and comparison of such data would have allowed the detection of any companion more than 1% of the star's brightness with separation  $\geq 0.2$  arcsec.

The ability of the interferometer to directly reveal emission sources close to a

nulled star is illustrated by images of late-type giant stars  $\alpha$  Orionis (Fig. 4.4b) and R Leonis. The faintest nulled images are still 36% and 24% respectively of the integrated flux of the brightest image. The large residual fluxes arise because

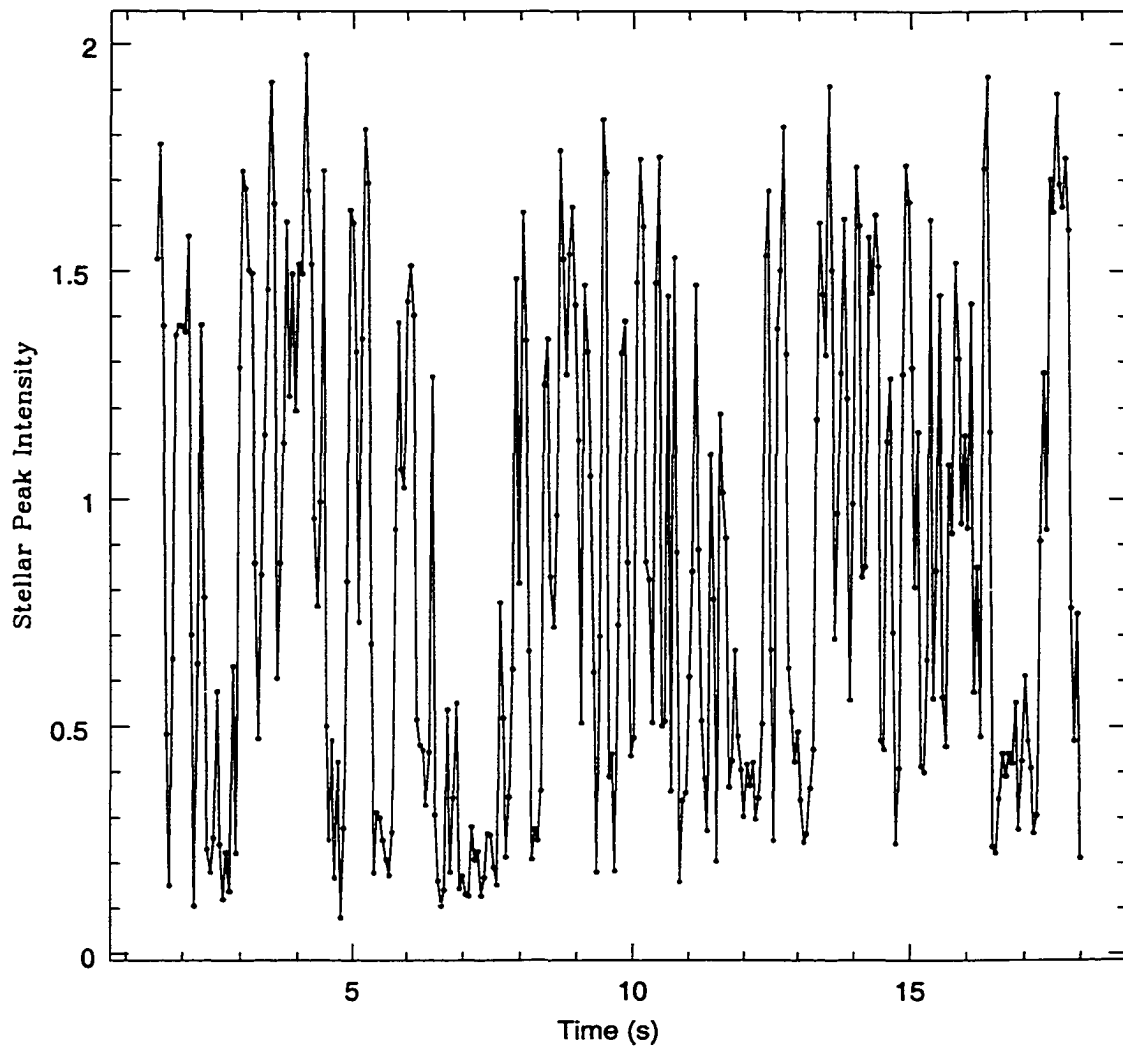


Figure 4.3 Plot of intensity variations of the null due to atmospheric turbulence.

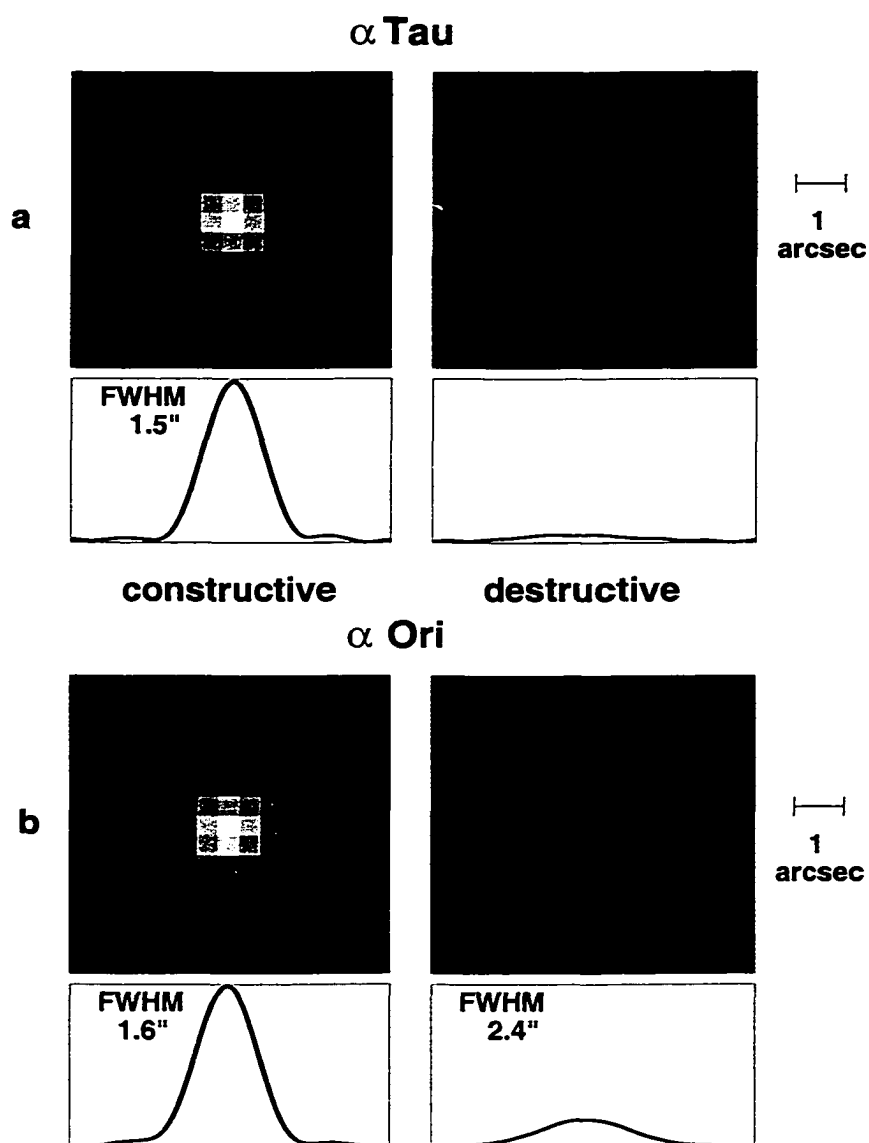


Figure 4.4 Single short-exposure frames at  $10.3 \mu\text{m}$  showing constructive and destructive interference. The one-dimensional plots under the images are smoothed cuts through the central row of pixels.

both stars have surrounding warm dust nebulae with significantly more than a 0.2 arcsec diameter, and thus lying mostly outside the central null fringe. The stellar discs themselves are small enough (40-56 mas diameter, Bester et al. 1996) that only 0.5-1% of their flux is transmitted at the limb, assuming uniform brightness.

The images shown in Figure 4.4 were selected for maximal and minimal flux from a series of 1000 frames of 50 ms exposure for  $\alpha$  Tauri and 500 frames of 100 ms exposure of  $\alpha$  Orionis, taken at 10% bandwidth by MIRAC2 operating in a continuous recording mode with no “dead time”. Alpha Tauri, which is unresolved, was observed on February 17, 1998 under seeing conditions characterized by Fried’s length  $r_0(10 \mu\text{m}) = 3.7 \text{ m}$  as measured by image motion (Martin 1992). Alpha Orionis was observed on January 17-18, 1998, under better seeing conditions ( $r_0 = 4.4 \text{ m}$ , slower motion).

As described in chapter 3, a feature in this implementation of the nulling interferometer, different from Bracewell’s original conception, is that the focal plane shows an image of the field about the nulled star. The image formed is the object flux multiplied by the transmission pattern of equation 2.2 and convolved with the point-spread function (PSF) of the individual elements. As the PSF is broader than the transmission pattern, the interference fringes are not visible in the focal plane. Thus true images are formed of smooth, extended features such as circumstellar dust, whose structure is on a scale larger than the fringe spacing. Alpha Ori and R Leo are shown in Figure 4.5 with increased signal-to-noise in composite images, obtained from the 12 best nulled images by shifting to a common center and adding, after repixelization. In the case of R Leo, the residual image with 1.7 arcsec FWHM is barely wider than the measured constructive image width of 1.5 arcsec, indicating a nebular width  $\leq 1 \text{ arcsec}$ . But Betelgeuse’s dust nebula is clearly

resolved, showing a FWHM of 2.4 arcsec and significant asymmetry. At 1% of the stellar intensity it extends radially 4 arcsec from the star. The image with the star interferometrically removed is the first to show the nebula directly. Previous work has established the amount of dust and its spatial extent from spectral analysis and interferometric synthesis. Thus Danchi et al. (1994) have created visibility curves for  $\alpha$  Orionis and R Leonis which have values of approximately 60% and 70% respectively for a 5 m baseline at 11  $\mu$ m. Calculating our visibility in the same manner, using  $\alpha$  Tauri as our calibration for unit visibility, we obtain good agreement:  $53 \pm 4\%$  for  $\alpha$  Orionis and  $69 \pm 5\%$  for R Leonis.

Figure 4.6 shows difference images formed by subtracting destructive from constructive images, each formed by recentering and co-adding the best individual exposures. The result for R Leonis (Fig. 4.6a) shows a well defined diffraction pattern, out to the third Airy ring which is accentuated to 0.4% of the peak by the central obscuration in the telescope of 10% of the diameter. The non-interfered images of unresolved stars, when similarly aligned and stacked, are not so perfect because they include the halo components from nebular emission or scattering due to higher order wavefront aberrations. These subtract out in the difference image. When a difference image is formed for  $\alpha$  Ori, a skewed Airy pattern results; however, by introducing a shift of 0.3 arcsec between the images, the nearly symmetric pattern shown (Fig. 4.6b) is recovered. The positions of the subtracted stars are shown by the crosses in Fig. 4.4, as determined by the offsets used to produce the symmetric patterns of Fig. 3.5. The offset for  $\alpha$  Orionis does not seem to be an effect of our instrument since it tracks field orientation in different exposures. We thus conclude that the photocenter of the nebular emission is displaced from the star. The offset angle is approximately 25 degrees East of North. Asymmetries in the photosphere and immediate surroundings of  $\alpha$  Orionis

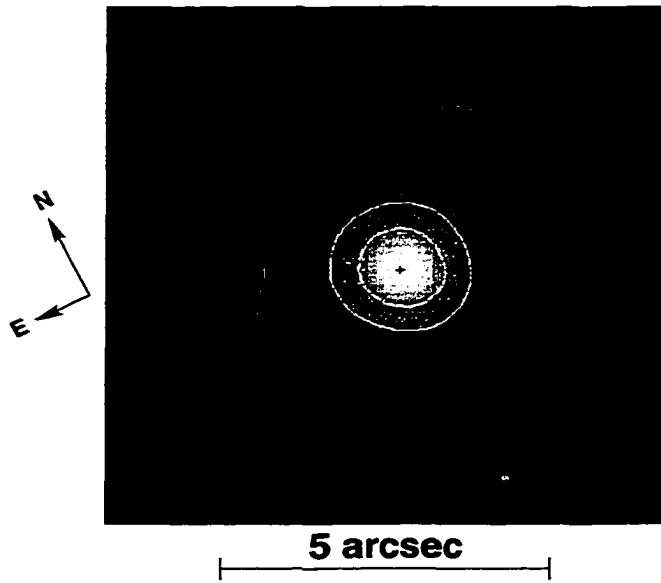
have been observed in H $\alpha$  emission (Hebden et al. 1987), the UV continuum (Gilliland et al. 1996), and 7 mm radio observations (Linn 1998). Bester et al. (1996) speculate the component of 10  $\mu$ m emission they saw from newly forming dust in 1994 was most likely asymmetric. However, the offset in photocenter of the extended 10  $\mu$ m emission has not been apparent in previous observations which were limited in their baseline orientation.

In the present system the best-nulled short exposures simply reflect the best destructive interference found among many images formed from atmospherically perturbed wavefronts. As discussed in chapter 3, change in phase and differential image motion over the integration time of the exposure prevent perfect starlight cancelation. From the measured rate of phase change, this effect alone is expected to result in a residual stellar intensity of 3% for  $\alpha$  Tauri (Hinz et al. 1998). Uncorrected higher order errors across each aperture such as astigmatism and focus also contribute to the residual intensity. Using the value of  $r_0$  derived from the image motion (3.7 m), and using equations 3.36 and 3.37 to estimate the intensity, this effect is expected to add a further 2% to the residual intensity of  $\alpha$  Tauri, for a total flux of 5%, in agreement with the measured value of 6%.

Although demonstrating an ability to make scientific observations, the original MMT nulling interferometer was short-lived. Observations were successfully undertaken both in January and February 1998, after which the MMT was shut down for renovation. The lessons learned in building this prototype, including methods of observation and alignment were crucial in building a more sensitive, cryogenic, nulling interferometer to be used with the renovated 6.5 m MMT.



## R Leonis



## $\alpha$ Orionis

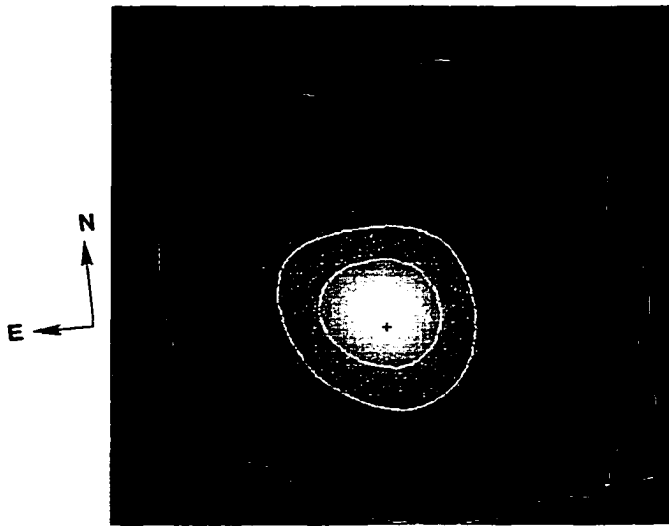


Figure 4.5 Combined nulled images for  $\alpha$  Orionis and R Leonis. The images show the  $10\ \mu\text{m}$  dust nebulae with improved signal-to-noise ratio. The contours are at the level 1%, 10%, and 20% of the non-interfered stellar peak intensity. The small + marks the centroid of the stellar emission. For  $\alpha$  Orionis this is clearly offset from the nebula.

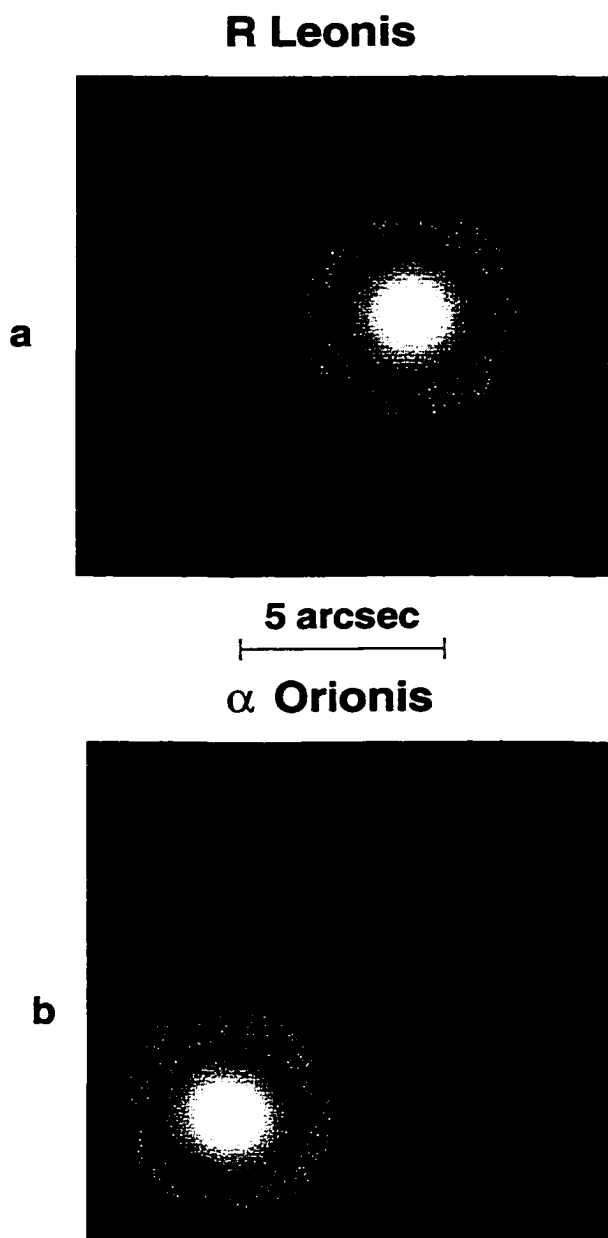


Figure 4.6 The images were obtained by subtracting the nulled images of Figure 4.4 from the corresponding constructive images. For  $\alpha$  Orionis a misalignment of the centroids by 0.3 arcsec was applied to obtain the symmetric diffraction pattern shown.

## CHAPTER 5

### DESIGN OF A CRYOGENIC NULLING INTERFEROMETER FOR THE 6.5 M MMT

This chapter describes the design and construction of a cryogenic nulling interferometer based on the MMT prototype. The instrument, called the Bracewell Infrared Nulling Cryostat (BLINC), has been in use since June 2000 on the converted MMT which now has a single 6.5 m primary. Coupled with the deformable secondary of the MMT (Lloyd-Hart 1999) the instrument will begin searches for faint companions as well as zodiacal dust as described in Chapter 9.

#### 5.1. Instrument Description

The design of BLINC is based on the prototype instrument used on the old MMT (Hinz et al. 1998). A photo and sketch of the optical layout of BLINC is shown in Figure 5.1. Although the optical layout is similar to the prototype there are several changes to improve performance and ease-of-use. The interferometer is enclosed in a liquid nitrogen cooled cryostat and is mechanically attached to the mid-infrared camera, MIRAC (Hoffmann et al. 1998) with a common vacuum. Actuator feedthroughs allow alignment of the interferometer while the cryostat is

cooled and evacuated. An adaptive phasing sensor and corrector is built into the interferometer as described below.

Unlike the prototype instrument, BLINC is designed to work with a single telescope beam. This requires division of the incoming beam into right and left halves in order to create an effective interferometer with the two sides of the telescope.

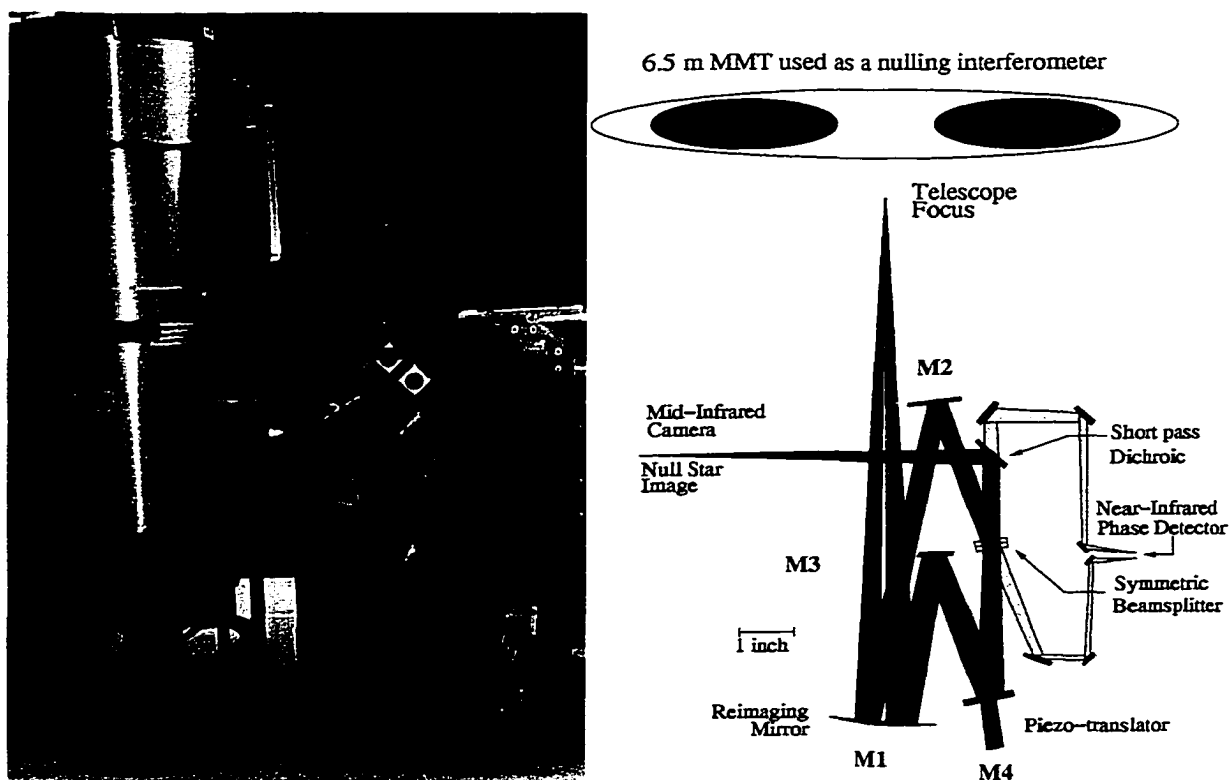


Figure 5.1 The optical layout of BLINC. The individual apertures inscribed in the 6.5 m MT primary are each 2.7 m across and separated by 3.8 m.

### 5.1.1. Nulling Optimization

To achieve a deep null the design must avoid introducing any differences in the two beams which would lead to inefficient interference. Differences in intensity, phase, polarization, or their relative dependence on wavelength will degrade the quality of the null. Sources of these errors include different numbers of reflections, different angles of incidence for reflection, and different coatings on the mirrors of each arm. Although it is possible to build in explicit controls of these quantities in the interferometer it is advantageous to design the optical paths to be nearly identical in order to minimize the differences. To keep the beams as symmetric as possible the interferometer is designed so that, after the reimaging mirror, both beams travel a nearly identical “backwards N” path through the interferometer for the destructive output. The angles of incidence of the relay mirrors are kept as small as possible, consistent with a small instrument, to minimize polarization errors.

### 5.1.2. Optical Layout

The telescope beam comes to a focus just inside the interferometer cryostat. Several baffles and an adjustable rectangular field stop at this point limit the radiation into the optical path. The telescope beam next encounters the main powered optical element (M1) in BLINC: an off-axis ellipsoid which, combined with a pupil reimaging lens, located between the interferometer and camera cryostat, converts the f/9 telescope beam of the full telescope to an f/16 beam required by MIRAC. The light next encounters mirror M3 which reflects only one half of the beam, splitting the light into two halves corresponding to the two sides of the telescope pupil. An additional mirror in each half beam (mirrors M2 and M4) direct the beams onto opposite sides of a 50% transmissive beam-combining optic (normally referred to as a beam-splitter). The beam-splitter is arranged so that

the beams incident on it are overlapped completely after passage through it. The beam-splitter produces two outputs, but only one of these (the nulled one) is sent to the infrared camera, using an additional mirror which also serves as a short pass dichroic. The telescope focal plane is imaged near the interface between the two dewars. A Potassium Bromide lens (not shown) is placed just prior to this focal plane to reimage the pupil to the approximate distance of the MMT secondary which is the entrance pupil of the system. The MIRAC optics reimage the focal plane onto a Si:As detector using a tilted, off-axis ellipsoid. The ellipsoid forms an image of the secondary prior to its reimaged focal plane, where a helium-cooled stop is placed to block out the warm emission from the telescope structure. This stop defines the size of the two beams from each side of the telescope. Since the beams are already overlapped at this point the stop constrains the two apertures to be identical in size. An f/36 stop in MIRAC constrains each beam on the primary to be 2.7 m in diameter. A filter wheel placed just behind the cold stop selects the wavelength detected by the mid-infrared detector.

Light from the star at a wavelength of  $2\ \mu\text{m}$  is also sensed using a detector within BLINC as shown in Figure 5.1. The mirror which reflects the  $11\ \mu\text{m}$  light to MIRAC is a dichroic which is transparent at  $2\ \mu\text{m}$ . Several fold mirrors relay both outputs of the beam-splitter to a HgCdTe NICMOS3 detector. This light is used to detect and control the phase of the interferometer as described in section 3.2.

The optical design is for use initially with the f/9 rigid secondary of the MMT and also with the f/15 deformable secondary once it is commissioned. The change between the two is accomplished by a separate re-imaging ellipsoid for each corresponding focal ratio. The ellipsoid, along with the Potassium Bromide lens, ensures that the original beam, f/9 or f/15, is converted to a final focal ratio

of  $f/16$  as the infrared camera requires. By interchanging only the ellipsoid it is possible to have a well-tested instrument available once the deformable secondary is ready. The off-axis ellipsoid segments are fabricated by Buddy Martin at the Mirror Laboratory at the University of Arizona by bending the correct amount of asphericity into the substrate as the mirror is being polished. This is a convenient way of creating small, off-axis mirrors without having to fabricate the often much larger parent surface.

### 5.1.3. Mechanical Design

The whole interferometer is enclosed in a custom-made nitrogen cooled dewar. The optics are mounted to a vertical cold plate within the dewar which is directly connected to the cryogen container, keeping the optics isothermal. Radiation baffling is done via two concentric shields within the dewar enclosing the entire instrument. In addition extensive interior baffling is placed around the beam paths to prevent scattered light from reentering the beam path. Alignment and phasing of the interferometer is possible with the instrument cooled and evacuated using a number of feedthrough actuators in the case. A custom-designed beam-splitter, as described in 3.1 is used to obtain a broadband null. Detailed mechanical design and cryostat fabrication was performed by Infrared Laboratories, Inc. of Tucson, Arizona.

In addition to its supporting role for nulling, MIRAC is also useful as a direct imager at the MMT. To be able to make efficient use of the instrument, BLINC's ellipsoid can rotate 180 degrees to illuminate a mirror train which sends the telescope beam to MIRAC without splitting it. The imaging channel (shown in Figure 5.2) has an internal cold stop to baffle the central obscuration of the telescope (not done in MIRAC) thereby increasing its sensitivity. This allows both

nulling and imaging observations using the instrument with minimal delay. The mirror movements needed to change modes can be performed with the cryostat cooled, and allow flexible observation scheduling.

#### 5.1.4. The Mid-infrared Array Camera (MIRAC3)

The science camera used for observations is MIRAC3, with a 128 x 128 Arsenic doped Silicon array detector manufactured by Boeing. The camera was built and is maintained as a joint project of the Smithsonian Astrophysical Observatory and the

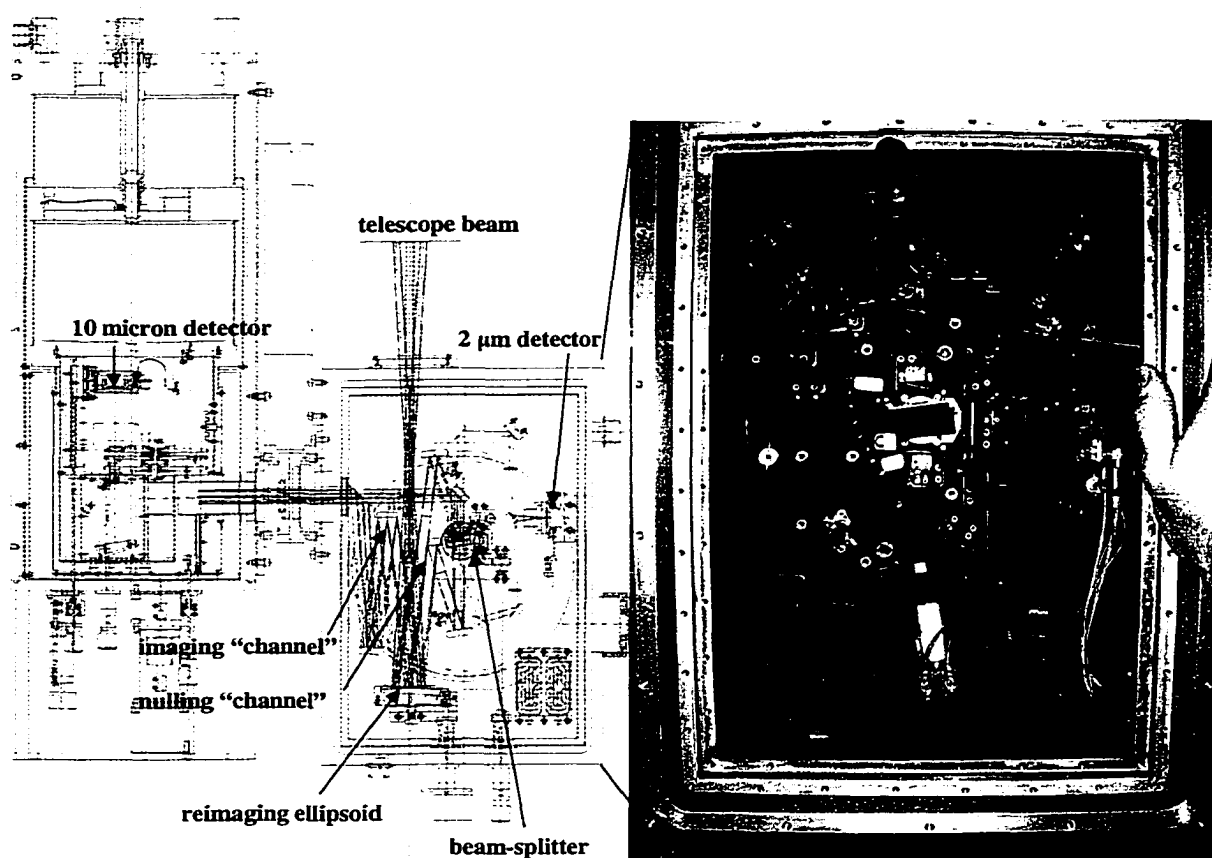


Figure 5.2 Mechanical Drawing and photo of the BLINC cryostat interior.



University of Arizona with support from SAO, U/A, NSF, and NASA. The camera optics allow the formation of a single pupil stop for both arms of the interferometer after the beams have been combined in BLINC. It has a wide selection of filters available in the N band (8-14  $\mu\text{m}$ ) and Q band (17-24  $\mu\text{m}$ ), as well as an N band grism ( $R=80$ ) for dispersing the nulled light. This is useful in diagnosing how the suppression varies with wavelength and in analyzing the residual light for evidence of silicate emission, for example, expected in circumstellar disks. The two instruments are separated by a gate valve with a window inserted in the flange. This allows the instruments to be operated separately if, for example, we wish to have BLINC open to the air, or to remove this window when both instruments are cooled and evacuated to increase the sensitivity. Due to this modularity it is possible to operate BLINC with different science cameras.

Upon entering MIRAC the focal ratio of the full telescope beam is  $f/16$ . The detector's pixels are 75  $\mu\text{m}$  across giving a plate scale of 0.15 arcsec/pixel, oversampling the 0.85 arcsecond diameter point spread function from each nulling aperture.

The camera electronics allow rapid short exposure images (1-100 ms) to be recorded with very little overhead. This is useful in initial observations with BLINC where active phase control is not possible. Individual frames can be selected for those with the best null. In addition, with adaptive phasing of the interferometer it is possible to sense which frames are not well nulled and reject these images in real time, keeping only the images with the best level of suppression.

The camera has an important feature for aligning the interferometer. A lens in one of the filter wheels forms an image of the cold pupil stop on the detector, which is also an image of the telescope pupil. Since the two apertures must be precisely

overlapped to maximize the cancellation this diagnostic is crucial. The alignment of the two beams on the telescope pupil can be measured and adjusted.

#### 5.1.5. The Beam-splitter

As discussed in chapter 3, the key component in the interferometer is the beam-splitter. For initial observations a standard thin film beam-splitter is being used. The final beam-splitter is created using two 5 mm thick, wedged ZnSe plates. The wedging prevents spurious reflections from the outer surfaces of the plates from contaminating the final image. The plates are fabricated with a  $40\text{ }\mu\text{m}$  thickness difference to compensate for phase dispersion. The wedges are put together so that the thin end of each plate points in the same direction. A slight relative translation of the wedges allows the thickness difference to be tuned, compensating for errors in fabrication.

The required  $\lambda/4$  air gap between the plates is created by laying down a thin film coating of aluminum at three points around the edge of one plate. The thickness of the dots is  $2.8\text{ }\mu\text{m}$ . The plates are pressed together at the three points of deposition to create a gap which is flat, from optical inspection using a mercury lamp, to less than a half wave.

### 5.2. Phase Correction System

The phase difference between the beams at  $11\text{ }\mu\text{m}$  can be sensitively controlled at  $2\text{ }\mu\text{m}$ , as described in 3.2. For this measurement it is important to measure both outputs of the interferometer to differentiate true variations in intensity from those created by phase variations. Intrinsic variations will be common to both outputs while phase-induced variations will brighten one image and dim the other.

The current implementation of this technique in BLINC will use a HgCdTe NICMOS3 detector to measure the total flux from both outputs of the beam-splitter. A tunable algorithm in the camera control software calculates the phase error due to an intensity difference and controls an analog output which is fed to a Polytec PI PZT driver. The PZT is mounted to the back of a mirror in one arm of the interferometer as shown in Figure 5.1. The PZT is designed to operate cryogenically and has a stroke at liquid nitrogen temperatures of 15  $\mu\text{m}$ . Phase data taken at the MMT site (Wizinowich et al. 1992) show this amount of stroke should be adequate for tracking phase errors due to atmospheric effects on good nights of seeing. Strain gauge sensors on the PZT ensure linear positioning of the mirror versus input signal. The entire loop will operate at 100-200 Hz to adaptively control the instantaneous null.

### 5.3. Alignment of the Interferometer

To properly suppress the light from a point source the interferometer must precisely overlap the two images of the star as well as overlapping the two pupils (or portions of the primary). That is, the final combined beams must be perfectly colinear. We have designed the system to allow alignment of the entire system on the telescope without requiring the use of a star. Thermal contrast of the telescope pupil and an internal image or field stop within BLINC are viewed to accomplish the alignment of both the pupils and field images. This is useful in being able to have the system ready for observation as efficiently as possible.

The optics are designed so that one arm of the interferometer is not adjustable. The light traveling through this arm of the interferometer defines the optical path to which the other path must be aligned. On the telescope the instrument is hung

from an adjustable gimballed mount which allows the whole unit to be tipped and tilted around axes roughly centered on the focal plane of the telescope. The alignment of the instrument is monitored by using the pupil imaging lens. Since the camera optics create an image of the secondary at MIRAC's cold stop, which has several externally selectable stop sizes, it is possible, by selecting a larger stop size, to see the telescope pupil as seen by both arms of the interferometer on the 10  $\mu\text{m}$  detector. The two arms of the interferometer each show roughly half the pupil, centered on the left and right side of the aperture as shown in Figure 5.3. The instrument is tilted until the image from the non-adjustable arm shows exactly half the secondary obscuration. By rotating the beam-splitter the image corresponding to the adjustable arm of the interferometer is translated to align the outside edge of its image with the inside of the non-adjustable arm. The non-adjustable image is not affected since its light is transmitted through the beam-splitter in the output the 10  $\mu\text{m}$  detector sees. In this way the left and right sides of the telescope pupil are overlapped. Once this is done a smaller cold stop in the infrared camera is selected to define a single pupil size for both arms of the interferometer. This stop, projected onto the primary, defines two circular regions extending from the edge of the inner hole to the outer edge of the mirror on each side of the telescope. They correspond to a physical size on the primary of 2.7 m for each aperture. Once this is done the pupils are overlapped, but the images may still be separated. By creating an image of the field stop in BLINC with each arm of the interferometer, we can see whether there is any misalignment. The final image overlap is accomplished by moving mirror M2 in the adjustable arm of the interferometer. Since this mirror is near the pupil image formed by the reimaging mirror, it does not affect the pupil overlap. It should be noted that the alignment up to this point can all be done prior to pointing the telescope at a star.

Once the beams are overlapped the path-length between the beams must be equalized. The beam-splitter is mounted on a motorized translation stage which can be moved up to 2 mm. This translation is done while monitoring the flux of a star in short exposure images. When the two beams have a large path-length difference the flux of the overlapped images is constant with time. As the stage approaches the point at which the path-lengths are equal the stellar flux will begin to vary in a random way due to atmospheric turbulence-induced phase differences. The amount of this fluctuation is maximized when the stage is at zero path-length difference. It is periodically fine-tuned by using a 50% passband which has a coherence length of approximately  $20\text{ }\mu\text{m}$ . 10% filters are routinely used for the

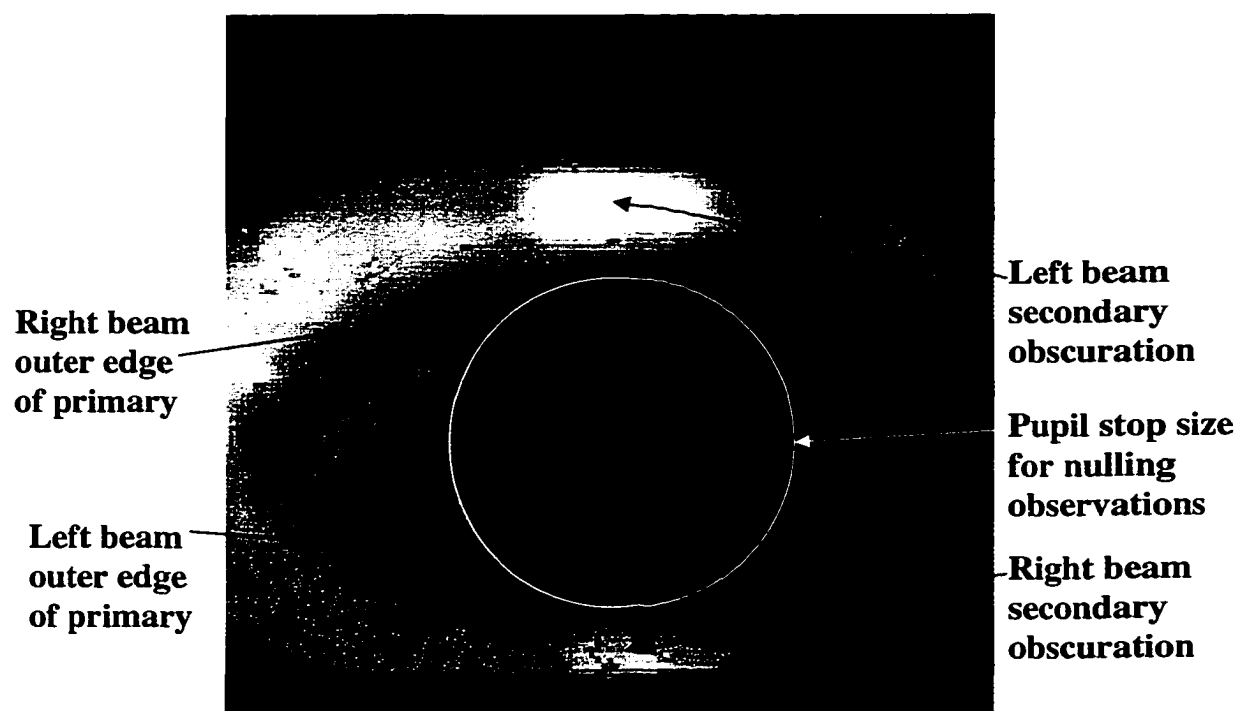


Figure 5.3 Pupil image showing the two sides of the mirror overlapped.

observations for which the coherence length is  $\simeq 100 \mu\text{m}$ , large enough to not limit the null after the fine-tuning.

The path difference can also be fine tuned by changing the position of the source on the detector through telescope pointing along the line connecting the two apertures. This introduces a path difference between the two apertures as illustrated in Figure 2.1. The point on the detector at which zero path-length occurs is thus a sensitive ( $3.1 \mu\text{m}/\text{pixel}$ ) indicator of any change due to telescope or instrument flexure. We have found the stability of the instrument and telescope to be excellent at the MMT. In the initial tests of the instrument, once the interferometer was aligned, the point of zero path-length remained constant (as determined by the placement of the image on the detector corresponding to zero path-length) from night to night over different elevation pointings as well as rotation of the instrument by 90 degrees to create apertures along the perpendicular direction of normal operation.

#### 5.4. Expected Null Depth

As discussed in chapter 3, suppression of the star is limited by error contributions from the instrument design as well as the telescope baseline and atmospheric turbulence. The main contributions to the expected residual intensity at  $11 \mu\text{m}$  are calculated and the results summarized in Table 5.1. The calculations are performed over a 20% bandpass, from  $10\text{-}12.2 \mu\text{m}$ . This corresponds to the portion of the N band which has the best sky background, bracketed by the ozone band on the short side and carbon dioxide absorption on the long side.

### 5.4.1. Phase vs. Wavelength

The residual intensity for the beam-splitter described above from phase variations is shown in Figure 3.4. Optimizing this to create the best null over only the 10-12.2  $\mu\text{m}$  region results in a residual intensity of  $1.7 \times 10^{-6}$ . A more substantial contribution should be allowed for due to the tolerance on the thickness difference. If a 1  $\mu\text{m}$  tolerance on the thickness difference is allowed the residual intensity is at most  $4 \times 10^{-6}$  using equation 3.14.

### 5.4.2. Intensity and Polarization Effects

Using the equations in section 3.3.4 for the reflection intensity for each sense of polarization as a function of wavelength, both the amplitude variations and errors

Source of Error	Fractional Residual Intensity
phase vs. $\lambda$	$4 \times 10^{-6}$
polarization and amplitude	$3.8 \times 10^{-5}$
star leak (sun at 10 pc)	$2 \times 10^{-6}$
adaptive optics spatial errors	$2.0 \times 10^{-4}$ ( $1.6 \times 10^{-5}$ )
adaptive optics temporal errors	$1.2 \times 10^{-4}$ ( $1.7 \times 10^{-5}$ )
<b>Total</b>	<b><math>3.64 \times 10^{-4}</math> (<math>7.7 \times 10^{-5}</math>)</b>

Table 5.1 Contributing levels of residual intensity. The total amount of residual intensity is listed for the case of operation with the MMT's adaptive optics system under good seeing conditions ( $r_0=6.3$  m,  $t_0=0.25$  s). The numbers in parentheses for the AO system correspond to limits which are relevant if a wavefront sensor is used detecting  $\sim 300$  modes and the DM has an update rate of 1 ms (compared to  $\sim 100$  modes sensed and 1.7 ms update rate for the planned system).

from polarization differences can be calculated together. For the angle of incidence of the beam-splitter in BLINC (8.08 degrees) the resulting residual intensity is expected to be  $3.8 \times 10^{-5}$  from both effects. This effect is a dramatic function of the angle of incidence. Increasing the incidence angle to only 15 degrees causes the residual to be  $4.2 \times 10^{-4}$ , compromising the performance.

### 5.4.3. Diameter of the Star

For the BLINC instrument on the MMT the modest baseline means even the closest main sequence stars will not produce an appreciable amount of residual intensity due to their finite diameter. Using equation 3.29 the star leak at  $11 \mu\text{m}$  from a sun-like star at 10 pc is  $1.6 \times 10^{-6}$ . Sirius provides the most residual intensity for a main sequence star at  $9.4 \times 10^{-5}$  while a typical giant star, such as  $\alpha$  Tau, at 20 mas in diameter, is limited to  $8.3 \times 10^{-4}$ . Because of this the very nearest main sequence stars are perhaps the most appealing targets for BLINC (see Table 8.3 for examples). Longer baseline interferometers such as the Large Binocular Telescope (LBT) and especially Keck will not obtain as good a level of suppression, and the larger amount of flux received from the nearby systems will allow BLINC to detect relatively faint structure around these stars despite the modest size apertures compared to Keck and LBT.

### 5.4.4. Atmospheric Turbulence

Chapter 3 discusses the limits to nulling without wavefront correction. This limit is the dominant source of intensity in these telescope observations, limiting the null to approximately 2-15%, depending on seeing conditions. Initial observations have shown that the ability to suppress the light is critically dependent on the strength of upper atmosphere turbulence as indicated by the presence of the



jet stream above the telescope site. The existence of the jet stream has been a consistent indicator that nulling observations are not possible over several different observation periods. This is not surprising, since these conditions produce quickly changing atmospheric turbulence, causing the intensity fluctuations to be averaged out over even short exposure images. Typical windspeeds in the jet stream are 40-50 m/s, which, combined with the smaller values of  $r_0$  typical for these weather conditions corresponds to values for  $t_0$  of  $\leq 40$  ms.

More precise observations will be possible with the deformable secondary of the MMT capable of correcting these higher order aberrations. The deformable mirror has 336 actuators corresponding to an inter-actuator spacing of 31 cm. The system is expected to update at 600 Hz, sensing and correcting approximately 100 Zernike modes. Since the target objects for nulling are very bright stars, in terms of what is typically used for adaptive optics corrections, the MMT system, with its high density of actuators, is capable of delivering a very good Strehl ratio.

For nights of good seeing ( $r_0=6.3$  m and  $t_0=0.25$  sec) the total wavefront error after correcting 100 Zernike modes will be 0.084 rad. This will leave a residual intensity of  $1.3 \times 10^{-4}$  in the focal plane. If the object is at a zenith angle of 45 degrees, the differential refraction through the atmosphere adds an additional 0.053 rad of wavefront error. Combining the two errors in quadrature, the residual intensity from equation 3.40 is  $2.0 \times 10^{-4}$ . This error can be minimized in two ways: by sensing and correcting all modes up to the fitting limit of the deformable mirror ( $\simeq 300$  modes) and by observing sources at high elevation or fine tuning the null with differential wavefront sensing at  $2 \mu\text{m}$ . If these improvements are made, the total wavefront error would drop to 0.048 rad and be spread into a wider halo corresponding to a residual intensity of  $1.6 \times 10^{-5}$ .

The temporal latency provides the other main source of error in the AO system for nulling observations. The lag, approximately  $1/600$  s, is expected to create a wavefront error of 0.015 radians, which is not spread over a wide halo, as the spatial errors are, leading to a residual intensity of  $1.2 \times 10^{-4}$ . The deformable mirror has a settling time of approximately 0.5 ms. If the wavefront could be sensed and reconstructed over this time period the wavefront error would drop to 0.0056 rad, corresponding to a residual intensity of  $1.6 \times 10^{-5}$ . This is feasible in principle, but would require a significantly faster, larger format wavefront sensor than is currently planned for the MMT. This error could also be reduced by a prediction of the wavefront evolution (Stahl and Sandler 1995), though doing so depends on adapting to the changing conditions of the atmosphere.

Each of the errors calculated above can be assumed to be uncorrelated. Thus each error independently contributes to the residual starlight in the focal plane. As listed in Table 5.1 the expected total residual leak of the nulling interferometer is approximately  $3.5 \times 10^{-4}$  for telescope observations. Improvements to the AO system would bring this level down by a factor of  $\sim 5$ .

## CHAPTER 6

### LABORATORY EXPERIMENTS IN PRECISE SOURCE CANCELLATION

In preparation for use with the MMT AO system laboratory tests have been undertaken with BLINC to determine what level of suppression is possible with an artificial source. To accurately assess the performance of the instrument it is important to verify that no errors (due to design or tolerance) prevent the system from reaching the expected  $10^4$  level of rejection.

#### 6.1. Experimental Setup

The setup for laboratory tests is shown in Figure 6.1. The instrument is fed by simulator optics which mimic the focal ratio and image plane location of the telescope beam. A CO<sub>2</sub> laser (emitting at  $10.6\ \mu\text{m}$ ) is used as the light source. The laser beam is co-aligned with a Helium-Neon laser (emitting at  $0.63\ \mu\text{m}$ ) using a dichroic mirror for simpler visual alignment of the system. Several mirrors relay the 3 mm diameter laser beam to a 10 mm diameter gold-coated glass ball which illuminates a 75 cm diameter f/2 mirror simulating the telescope primary. These optics form an f/9 focal ratio converging beam. A final fold mirror sends the light into the interferometer where it comes to a focus.

The defining point source is created by a 5  $\mu\text{m}$  pinhole placed at the focal plane of the telescope which is just inside the top surface of BLINC. The internal ellipsoid mirror, 215 mm away, re-images this and sends the beams through the interferometer. The projected separation of the two apertures on the ellipsoid (defined by the interferometer geometry and the MIRAC cold stop) is approximately 10 mm.

## 6.2. Expected Null Depth

The level of suppression of the source is expected to be limited by the finite diameter of the pinhole. This introduces a residual intensity in the same way as the effect of a finite stellar diameter; light “leaks” around the edges of the null and is not completely cancelled out. The projected fringe spacing on the focal plane, similar to equation 2.2, is given by

$$T(x) = \sin^2 \left( \frac{\pi x b}{\lambda f} \right), \quad (6.1)$$

where  $x$  is the linear dimension in the focal plane,  $b$  is the projected separation of the apertures on the ellipsoid, and  $f$  is the distance to the focal plane. This corresponds to a fringe spacing at the focal plane of approximately 0.23 mm at 10  $\mu\text{m}$ . We can slightly modify equation 3.29 to determine the amount of residual intensity due to the physical size of the pinhole. The fractional amount expected is

$$I_{\text{pinhole}} = \frac{\pi^2}{16} \left( \frac{S}{\frac{\lambda}{b} f} \right)^2 \quad (6.2)$$

where  $S$  is now the physical size of the pinhole. For a 5  $\mu\text{m}$  pinhole and the setup of the interferometer we expect a residual of  $\sim 3 \times 10^{-4}$ .

### 6.3. Alignment and Tolerances

The system is aligned by blocking off the adjustable arm of the interferometer using an internal shutter and measuring the position on the array of the image from the nonadjustable arm. Then by blocking off the fixed arm and adjusting the other arm the image centroid is positioned to  $< 0.1$  pixels of the nonadjustable image.

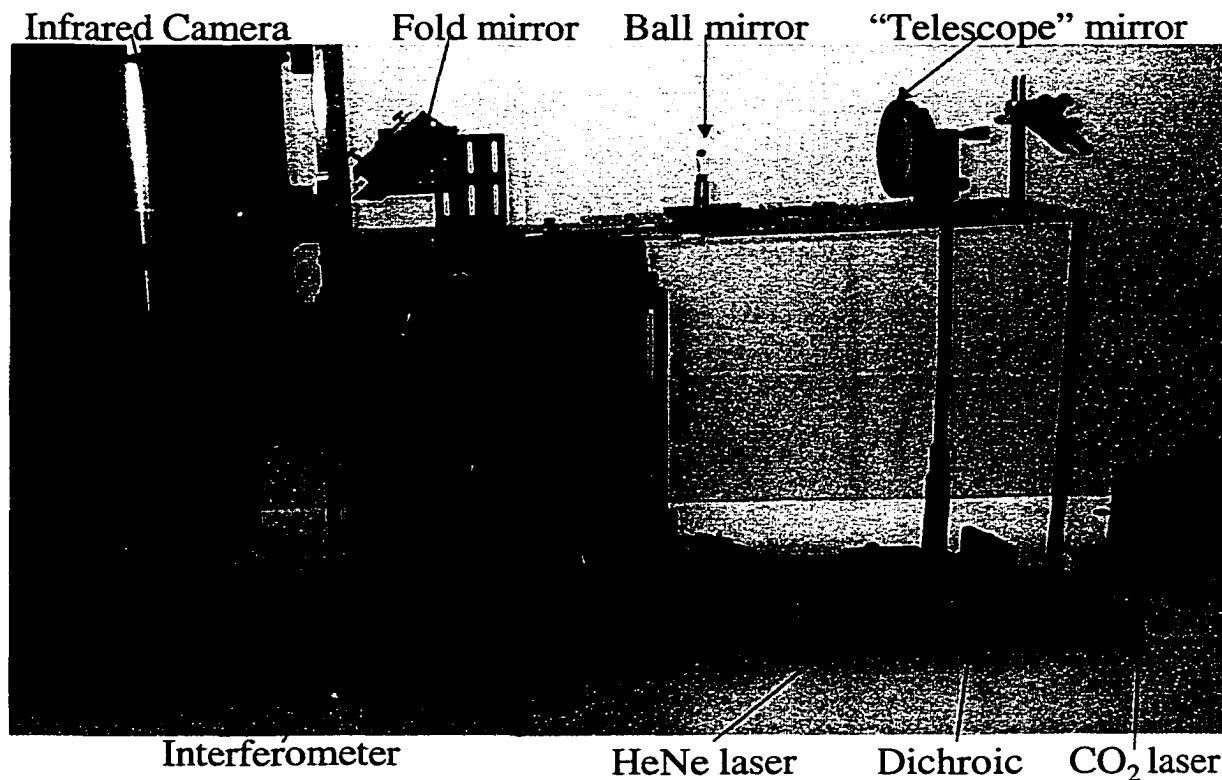


Figure 6.1 The laboratory setup for demonstrating deep levels of nulling. A CO<sub>2</sub> laser, through a series of optics illuminates a pinhole at the focal plane of the interferometer, simulating a point-like source.

If neither beam is vignetted, the common stop in MIRAC ensures that the pupil images are exactly overlapped. The smallest pupil stop in the MIRAC camera is used to minimize tilt errors between the beams. The stop is 1.67 mm diameter and 74 mm from the detector. Once the system is properly aligned the phase is adjusted by changing the voltage on a PZT behind one of the fold mirrors. Since this mirror is nearly normal to the beam, the misalignment caused by a translation on the order of 10  $\mu\text{m}$  is negligible.

To estimate the residual intensity from two images separated by 0.1 pixels, a simulation was created subtracting the wavefront from two pupils, with a diameter equal to the MIRAC stop and a tilt between them of

$$\theta = \tan^{-1} \left( \frac{0.1 p}{d} \right) \quad (6.3)$$

where  $p$  is the pixel size of 75  $\mu\text{m}$  and  $d$  is the distance from the pupil to the detector. Taking the Fourier transform of this subtracted wavefront and summing the total intensity in the image results in a flux of  $4 \times 10^{-5}$ , less than expected from the pinhole size.

The tolerance on the pupil alignment can be calculated in the same way, by shifting one pupil with respect to the other before subtraction. Taking the Fourier transform of the result, the resulting image gives the flux for a given shift. The common pupil is important since otherwise the pupils would need to be aligned to  $\sim 0.01\%$  of their diameter, a very difficult alignment.

## 6.4. Results

The images recorded at constructive and destructive interference are shown in Figure 6.2. Integration time for these images is 0.5 s. At the null position

small variations in path-length cause the image to be as bright as  $5 \times 10^{-3}$  of the constructive peak, but the best images show a residual of  $3.3 \times 10^{-4}$ , in good agreement with the expected residual from the size of the pinhole. The variations

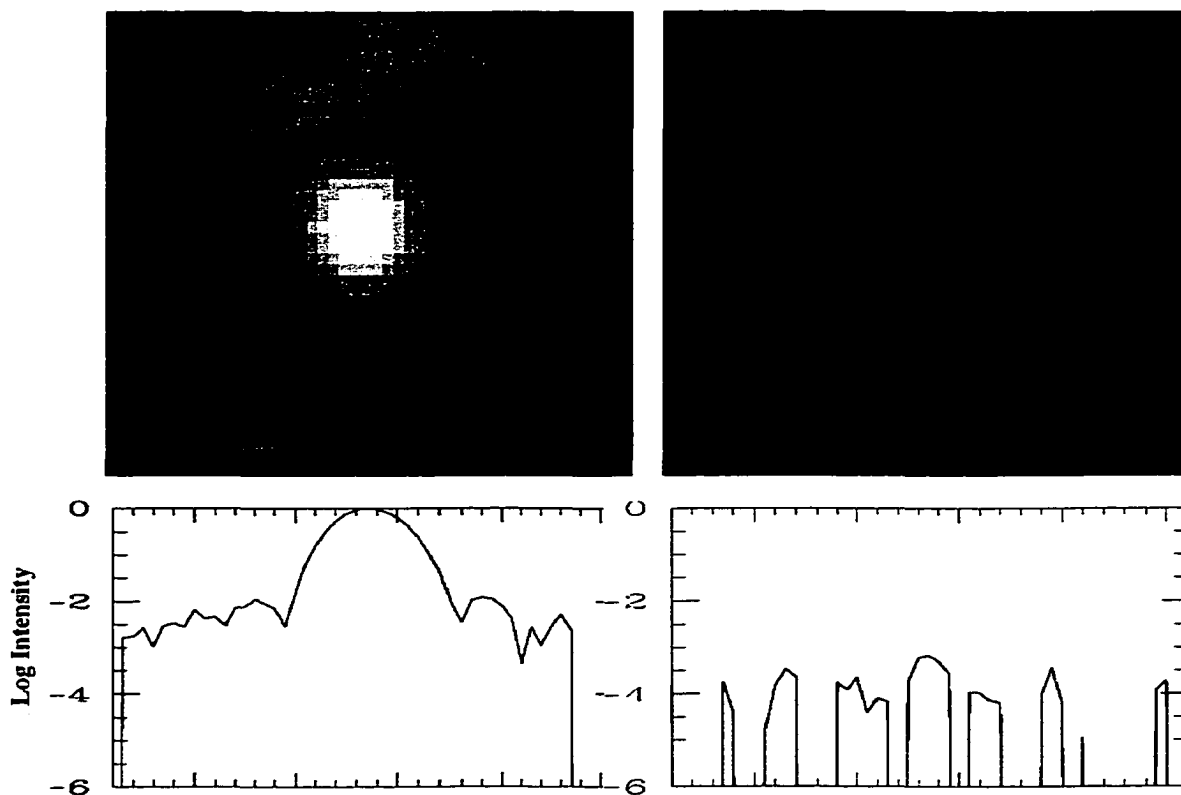


Figure 6.2 Deep suppression of an artificial point source. The two images show the point source at constructive and destructive interference. The integrated flux in the destructive image is  $3.3 \times 10^{-4}$  of the constructive image, as expected from the finite size of the source. The images are shown in log intensity versus greyscale to emphasize the faint structure. The plots show show a horizontal cut through each image.

in intensity are most likely caused by vibrations in the interferometer elements, and can be remedied by better isolation of the system in the vibrationally noisy environment of the laboratory.

The images shown in Figure 6.2 demonstrate the ability of nulling interferometry to suppress the entire Airy pattern as well as the scattered light associated with the source. The scattered light in the constructive image arises from optics after the beams have been combined and is thus suppressed in the same way as the main peak.

A null of a thermal source is more difficult to demonstrate since the point source intensity is significantly below that of even a low power laser. A simpler way of determining the level of path-length compensation in the system is to measure the adjacent nulls to either side of the best null as the relative path-length between the beams is changed. This accurately locates the center of the coherence envelope. As shown in Figure 6.3, the coherence envelope of a 50% bandwidth is asymmetric about the central null creating adjacent nulls which are significantly above the level of the central null and detectably different from one another. The correct amount of compensation (a difference in thickness of  $40\text{ }\mu\text{m}$  for ZnSe plates) would lead to the symmetric fringe pattern shown, with adjacent nulls of equal value at 17.5%. Measurements are plotted for the three successive nulls found for a thermal source with a standard N band astronomical filter (8-13  $\mu\text{m}$ ). The results of 17.7% and 16.9% for the two adjacent nulls are consistent with a thickness error of  $< 4\text{ }\mu\text{m}$  for the ZnSe plates corresponding to a residual of  $< 3 \times 10^{-5}$  over the 20% bandwidth planned for use in telescope observations.

The laboratory results have verified that the nulling design issues addressed in Chapter 5 to optimize the nulling performance have not been compromised in any



detectable way. These tests allowed the use of BLINC with the MMT telescope with confidence that it would perform as expected.

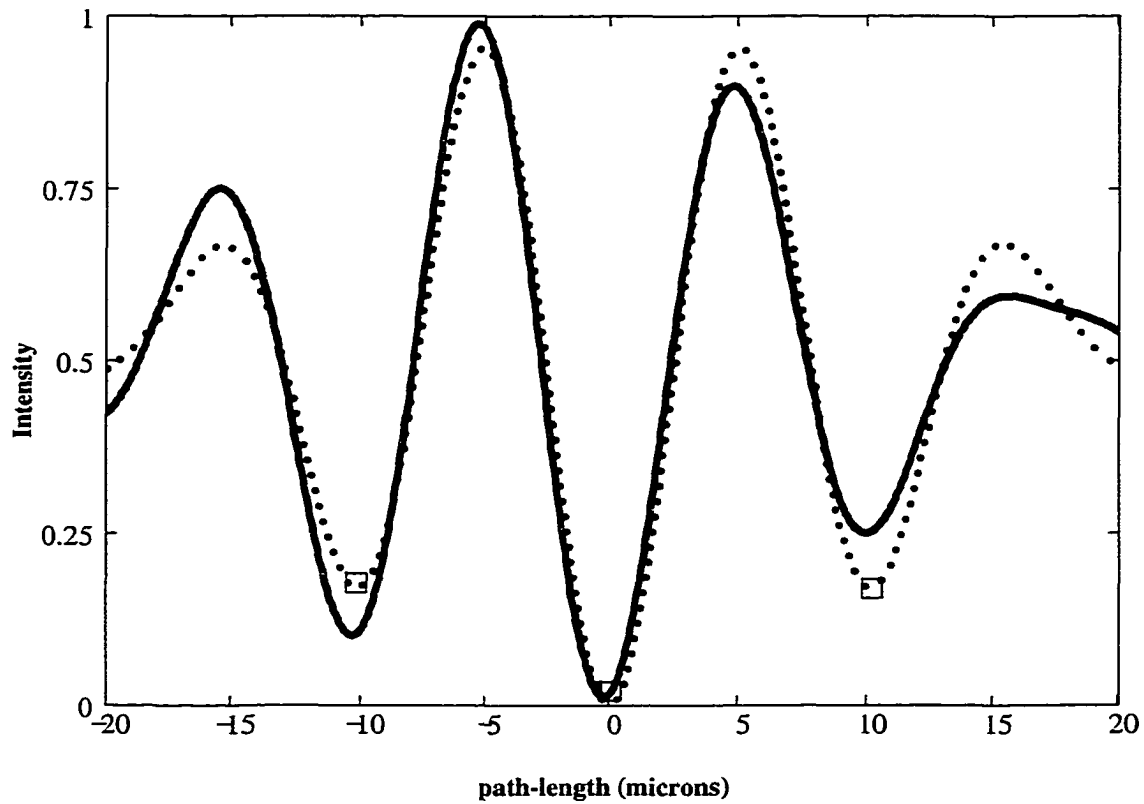


Figure 6.3 Measurement of phase compensation. Coherence envelopes for a 50% bandwidth system with no achromatic phase compensation (solid line) and the correct amount of phase compensation (dotted line). The three boxes are measurements of the three central nulls, demonstrating that the correct amount of phase compensation is in place.

## CHAPTER 7

### NULLING OBSERVATIONS WITH THE 6.5 M MMT

The 6.5 m MMT saw first light at the Cassegrain focus in May 2000, producing images which showed the telescope optics to be of good quality. BLINC was taken to the telescope on June 10-17, 2000 as the first science instrument to be used on the MMT. The telescope was still being finished during this time, but was performing adequately, allowing us to begin nulling observations. Alignment and phasing of the interferometer were achieved while the instrument was cooled and evacuated during the first night of observations, demonstrating the ease of alignment of the system.

#### 7.1. Observing Procedures

Since the atmospheric phase changes rapidly between the apertures, the method of observing, once the system is aligned and phased, is to take sequences of 500 frames, each with an integration of 0.05-0.5 s, depending on atmospheric conditions and source brightness. Under the best atmospheric conditions experience has shown that even 0.5 s is short enough to limit the phase changes to  $< 10\%$ . Observations of science objects are interleaved with similar brightness point source

calibrators. A sequence of 500 frames is sufficient to create several frames with properly overlapped images and a phase difference near enough to a half-wave that the temporal and higher order spatial errors dominate the amount of flux in the focal plane.

Observations were typically taken using a 10% bandwidth filter centered at  $10.3\ \mu\text{m}$  after fine tuning the null using the wider N band filter. Periodic checks on focus (which causes the overlapped images to separate) and phasing were performed to ensure proper interference of the light.

Since the MMT is an altitude-azimuth mounted telescope a derotating mechanism is available to continuously rotate the instrument. For nulling observations the mechanism is kept fixed in order not to rotate the two pupils in the instrument with respect to the telescope. However, the derotator allows orientation of the pupils along any suitable position angle on the sky. This is desirable in order to probe circumstellar structure in all orientations. Phasing and focus were checked after rotation of the instrument derotator, but typically were affected only slightly.

The sequence of frames is background subtracted using images of blank sky taken in between object observations. Once the images are background subtracted an IRAF script automatically calculates the flux in each frame by adding the total flux in a box  $1.8''$  on a side and subtracting the average sky flux surrounding this box to account for any drift in the background flux between the time when object and sky frames are taken. The minimum and maximum fluxes from this sequence are recorded to determine the amount of cancellation possible for each source. The instrumental null, is given by

$$N_i = \frac{I_{min}}{I_{max}} \quad (7.1)$$

where  $I_{min}$  and  $I_{max}$  are the minimum and maximum values recorded in a particular

sequence.

The standard measurement made in interferometry is the instrumental visibility of the source which is given by

$$V_i = \frac{I_{max} - I_{min}}{I_{max} + I_{min}}. \quad (7.2)$$

This is related to the instrumental null by

$$V_i = \frac{1 - N_i}{1 + N_i} \sim 1 - N_i. \quad (7.3)$$

The terms are described as “instrumental” since the results depend on the instrumental and atmospheric conditions as well as the intrinsic source contribution. To recover the true source visibility a measurement of a point source,  $V_c$  must be taken under similar conditions to calibrate the system. Then the source visibility is given by

$$V = \frac{V_i}{V_c}. \quad (7.4)$$

From this it is possible to derive the true source null:

$$N = \frac{1 - V}{1 + V} = \frac{1 - \frac{1 - N_i}{1 + N_i} \frac{1 + N_c}{1 - N_c}}{1 + \frac{1 - N_i}{1 + N_i} \frac{1 + N_c}{1 - N_c}} \sim N_i - N_c. \quad (7.5)$$

This corresponds to the amount of residual flux remaining in the focal plane due only to the structure of the source. It should be noted that this value is normalized to the constructive peak of the star. If the flux in a nulled image is due to extended material, its ratio, compared to the stellar emission, is twice  $N$ , since the constructive peak is twice the value of its uninterfered flux.

Typically two sets of 500 frames are taken for a given setup, with the null value varying between the two sets by approximately 1-3% (an instrumental null of 10% would range from 8-12% in successive sets). The signal-to-noise in the image is able to measure the source to better than this precision, but atmospheric effects cause

the level of suppression to vary by 1-5% between successive sets. The estimated errors in measuring the instrumental null are listed along with each object in Tables 7.2, 7.4, and 7.5. The errors in the instrumental null and the calibration null are summed in quadrature to calculate the uncertainty in the measurement of the residual flux in the nulled image for each object.

The interferometer is sensitive to structure which is  $\geq \lambda/2b$  from the central source, where  $b$  is the baseline of the interferometer. For the 3.8 m baseline of BLINC at  $10.3 \mu\text{m}$  this corresponds to  $0.28''$ . Additional information is available at the resolution limit of the individual apertures. Since the instrument forms a true image of the field any extended flux can be mapped out in two dimensions, free of the central point source. For the MMT the size of the individual apertures is 2.7 m corresponding to a FWHM at  $10.3 \mu\text{m}$  of  $0.8''$ .

## 7.2. Observations

BLINC was used to probe circumstellar environments of several different types of stars, including outflows of AGB and supergiant stars, dust disks around Herbig Ae/Be stars, and main sequence stars. Table 7.1 gives the observing log for the June MMT observations. Different exposure times were used for the individual frames of data, depending on the brightness of the sources. The shortest exposure time possible was chosen for each object consistent with being able to detect the image in well-nulled frames.

## 7.3. Calibration Stars

Calibration stars typically showed nulling levels of 5-15% depending on atmospheric conditions. An example of a typical constructive-destructive image pair for  $\alpha$

Object	Type	Date	Frame Time (s)	Wavelength ( $\mu\text{m}$ )	Instrument Orientation (degrees)
$\alpha$ Boo	CAL	6/13/00	0.05	10.3	0
$\alpha$ Boo	CAL	6/14/00	0.05	10.3, 10.6	0
$\alpha$ Boo	CAL	6/17/00	0.05, 0.1	8.8, 10.3, 11.7	0
$\alpha$ Her	CAL	6/11/00	0.05	10.3	0
$\alpha$ Her	CAL	6/13/00	0.05	10.3	0
$\alpha$ Her	CAL	6/14/00	0.05, 0.1, 0.5	10.3	0
89 Her	EV	6/17/00	0.1	10.3	0
$\alpha$ Sco	EV	6/13/00	0.05	10.3	0
$\alpha$ Sco	EV	6/14/00	0.05	10.3	0, 90
$\chi$ Cygni	EV	6/13/00	0.05	10.3	0
HD188037	EV	6/14/00	0.05	10.3	0
IRC+10216	EV	6/17/00	0.05	8.8, 10.3, 11.7	0
IRC+10420	EV	6/11/00	0.05	10.3	0
$\mu$ Cep	EV	6/11/00	0.05	10.3	0
NML Cygni	EV	6/13/00	0.05	10.3	0
NML Cygni	EV	6/14/00	0.05	10.3	0, 90
R Cas	EV	6/11/00	0.05	10.3	0
R Crb	EV	6/17/00	0.1	10.3	0
RX Boo	EV	6/13/00	0.05	10.3	0
W Hya	EV	6/17/00	0.05	10.3	0
HD150193	HAEBE	6/14/00	0.5	10.3	0
HD163296	HAEBE	6/14/00	0.5	10.3	0, 90
HD179218	HAEBE	6/14/00	0.5	10.3	0, 90
Vega	MS	6/13/00	0.5	10.3, 11.7	90
Vega	MS	6/14/00	0.5	10.3	0
Altair	MS	6/14/00	0.5	10.3	0

Table 7.1 Observing log for nulling observations. The stars are grouped into evolved stars (EV) such as AGBs and supergiants, Herbig Ae/Be stars (HAEBE), main sequence (MS) stars, and point source calibrator stars (CAL).

Bootes is shown in Figure 7.1. The images are shown in logarithmic intensity scaling at the same grey-scale level to bring out the faint structure. The peak of the nulled starlight in this image is 3% of the constructive image with a total flux remaining in the image of 7%. The nulled image is expected to be wider than the constructive image since the light which does not cancel out in a nulled image is from higher-order wavefront aberrations, such as focus, astigmatism, and trifoil in the two pupils which are scattered into an area greater than the Airy pattern of the star.

The star  $\alpha$  Herculi is used as a calibrator despite the fact it is known to have a dust shell. This is based on several previous interferometric measurements (Danchi et al. 1994) which measure it as unresolved on a 4-5 m baseline. The measurements of it appear consistent with other calibrator stars measured on the same nights as  $\alpha$  Herculi.

#### 7.4. Evolved Stars

Table 7.2 lists the evolved stars observed with BLINC and their associated source visibilities. These observations probe the dust outflows around asymptotic giant branch (AGB) and red supergiant (RSG) stars in an effort to understand their spatial extent and structure. This information gives useful constraints on the mass-loss history of these stars determining whether the mass-loss, for example, is uniform in time or episodic.

Much useful information has also been gathered in this area by the Berkeley Infrared Spatial Interferometer (Danchi et al. 1994). This interferometer can achieve high spatial resolution through heterodyne techniques to probe the dust outflow and stellar diameters of evolved stars. Typical measurements, however, are

sensitive to dust outflow only along one direction. The azimuthal structure of the dust is poorly constrained by such observations.

BLINC is able to detect structure at lower spatial resolution, but is sensitive to azimuthal structure. Such sensitivity allows probing for structures such as disks and jets in the outflow which may be faint compared to the central star, but detectable once the central source is suppressed. Currently, one poorly understood

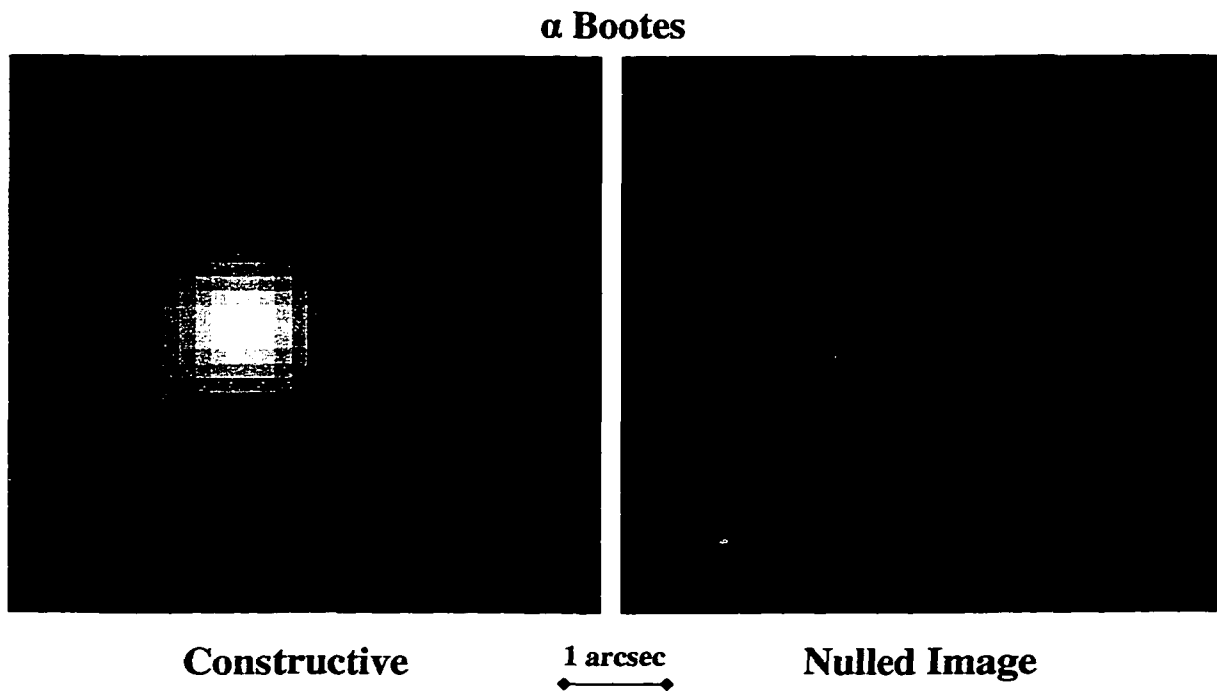


Figure 7.1 Constructive and destructive images for a typical calibrator star. Each pixel is  $0.15''$ . The greyscale is logarithmic with intensity.



area of AGB evolution is how the rather complex structure typically seen in planetary nebulae, the end-product of AGB stars, develops. The structure of planetary nebulae (PN) often appears quite asymmetric with bipolar or elliptical structure to the outflow. However, AGB stars are assumed and often observed to have circularly symmetric outflows quite different from the structure seen in PN. Whether this transition takes place between the AGB and PN stages or whether the asymmetries arise earlier in the AGB outflow is poorly understood (Lopez 1999). The early stages of mass loss around AGB stars are generally very mild, forming only a very faint circumstellar envelope around a star. This makes it very difficult to disentangle the stellar emission from the extended dust component. Nulling interferometry allows the structure of the surrounding dust outflow to be seen more clearly. In addition, the amount the point source is able to be suppressed is indicative of the spatial extent of the central component of the emission, corresponding to the visibility measurements of spatial interferometers. Since the apertures are derived from the 6.5 m mirror it is possible to measure this visibility at any chosen orientation of the baseline. By measuring the visibility at different orientations and forming an image of the extended emission it is possible to explore the levels of asymmetry in AGB stars at different points along their evolution to PN and to constrain models for dust formation around these stars.

#### **7.4.1. Resolved Examples**

For the evolved stars observed at the MMT the majority had structure resolvable at the resolution of the individual apertures. Images were constructed for those resolved by coadding several frames which had similar levels of null. The variations, from frame to frame for the images used for combination were  $< 5\%$  of the flux. Typically the dust was only mildly resolved for these stars, providing constraints on

spatial extent and ellipticity of the dust. Figure 7.2 shows a typical example of such an observation. The dust around the star  $\mu$  Cephei is shown to be mildly elliptical at a position angle of  $\sim 100^\circ$  once the light from the central star is suppressed. While Sudol, et al. (1999) have measured the mid-infrared visibility of  $\mu$  Cephei for a similar baseline, no two-dimensional or high resolution data exists for the source. The image suggests that the dust outflow is not circularly symmetric, but more bipolar in its structure.

Object	Instrumental Null (%)	Residual Flux (%)	Source Visibility (%)	Calibrator	Position Angle (degrees)	Extended?
IRC+10420	64 $\pm$ 2	57 $\pm$ 4	27 $\pm$ 3	$\alpha$ Her	117	yes
$\mu$ Cep	44 $\pm$ 1	35 $\pm$ 3	48 $\pm$ 3	$\alpha$ Her	108	yes
R Cas	19 $\pm$ 4	8 $\pm$ 6	85 $\pm$ 10	$\alpha$ Her	134	no
RX Boo	24 $\pm$ 1	18 $\pm$ 3	70 $\pm$ 4	$\alpha$ Boo	156	no
$\alpha$ Sco	27 $\pm$ 1	20 $\pm$ 4	67 $\pm$ 6	$\alpha$ Her	6	yes
$\alpha$ Sco	25 $\pm$ 1	18 $\pm$ 2	69 $\pm$ 3	$\alpha$ Boo	110	
$\alpha$ Sco	26 $\pm$ 3	19 $\pm$ 2	67 $\pm$ 3	$\alpha$ Boo	22	
$\chi$ Cygni	34 $\pm$ 2	27 $\pm$ 5	58 $\pm$ 6	$\alpha$ Her	17	yes
NML Cygni	62 $\pm$ 3	57 $\pm$ 5	27 $\pm$ 4	$\alpha$ Her	126	yes
NML Cygni	58 $\pm$ 1	52 $\pm$ 2	31 $\pm$ 2	Altair	114	
NML Cygni	63 $\pm$ 1	58 $\pm$ 2	26 $\pm$ 2	Altair	13	
HD188037	30 $\pm$ 4	23 $\pm$ 5	63 $\pm$ 7	Altair	120	yes
IRC+10216(11.7 $\mu$ m)	78 $\pm$ 1	74 $\pm$ 2	15 $\pm$ 1	$\alpha$ Boo	173	yes
IRC+10216(8.8 $\mu$ m)	80 $\pm$ 4	76 $\pm$ 4	14 $\pm$ 3	$\alpha$ Boo	174	
R CrB	10 $\pm$ 4	2 $\pm$ 4	97 $\pm$ 8	$\alpha$ Boo	4	no
WHya	25 $\pm$ 1	18 $\pm$ 2	70 $\pm$ 3	$\alpha$ Boo	102	yes
89 Her	11 $\pm$ 5	3 $\pm$ 5	94 $\pm$ 9	$\alpha$ Boo	178	no

Table 7.2 Nulling measurements of evolved stars at 10.3  $\mu$ m. The position angle is measured in degrees east of north and refers to the orientation of the interferometer baseline. The final column tabulates whether the dust is resolved compared to the PSF of a single element.

For stars with more pronounced dust outflows the structure is complex enough that the images are difficult to interpret in terms of simple structures. Figure 7.3 shows two images of the dust flow around  $\alpha$  Scorpii at two different baseline orientations. The cross marks the center of the stellar emission in each case. For one orientation the dust seems to be cleared out of the center region and the main peak of emission is significantly offset from the star position. In the orthogonal orientation the dust peak centers on the star peak and is more prominent compared to the rest of the cloud, suggesting that the inner dust is quite asymmetric.

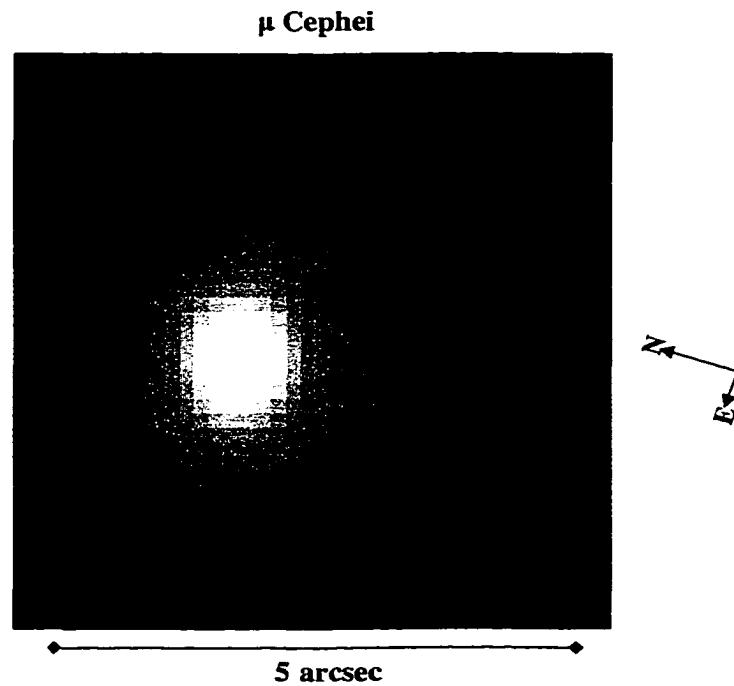


Figure 7.2 Nulled image of dust around  $\mu$  Cephei. The dust outflow has a measured ellipticity of 0.17 and position angle of  $100^\circ$  at a wavelength of  $10.3 \mu\text{m}$ . The grayscale is logarithmic versus intensity to enhance the faint structure.

Asymmetry is also apparent in the extended component, as shown by the ridges and clumps. These appear to be small enough to be modulated by the fringe pattern of the interferometer so that their relative intensity changes between the two images. This results in a faint underlying structure which is common to the two images with smaller clumps of varying brightness determined by the baseline orientation. A proper image of the dust cloud would require more observations at different orientations to reconstruct the actual brightness of the small clumps, but these images show that the dust outflow is a complex structure, not well described by a symmetric outflow.

Danchi et al. (1994) construct a model of the outflow around  $\alpha$  Scorpii from baselines similar in orientation to the left image in Figure 7.3. They conclude the dust shell is detached from the star with an inner radius of  $1''$ . This appears consistent with the image since the offset of the emission can only be introduced if the light is not dominated by dust close-in to the star. However, the right image, which probes dust structure in the orthogonal direction has a brighter central peak and is not offset from the stellar emission. This suggests that along the approximately north-south cut we are seeing dust close-in to the star, indicating that the dust model is not spherically symmetric even close-in to the star.

Figure 7.4 shows the nulled image of HD 188037, an AGB star with an A type companion. The primary, an M5 giant, has a mass-loss rate of  $2.7 \times 10^{-7} M_{\odot}/\text{year}$  (Jura and Kleinmann 1992) creating a significant infrared excess in its spectral energy distribution. The A star is probably a main sequence star and is located  $0.75''$  away at a position angle of  $274^{\circ}$ . Jura and Kleinmann (1997) estimate the physical separation of the pair as 450 AU, since little orbital motion has been measured over 100 years of observations. Figure 7.4 shows an extension of the

dust in the direction of the companion, suggesting that the main sequence star is illuminating the dust created by the giant and creating a detectable dust cloud of its own at  $10.3 \mu\text{m}$ .

IRC+10216 is an AGB star on the verge of the transition to a planetary nebula. Near-infrared observations of the star reveal a complex circumstellar structure evolving over timescales of only several years (Osterbart et al. 1999,

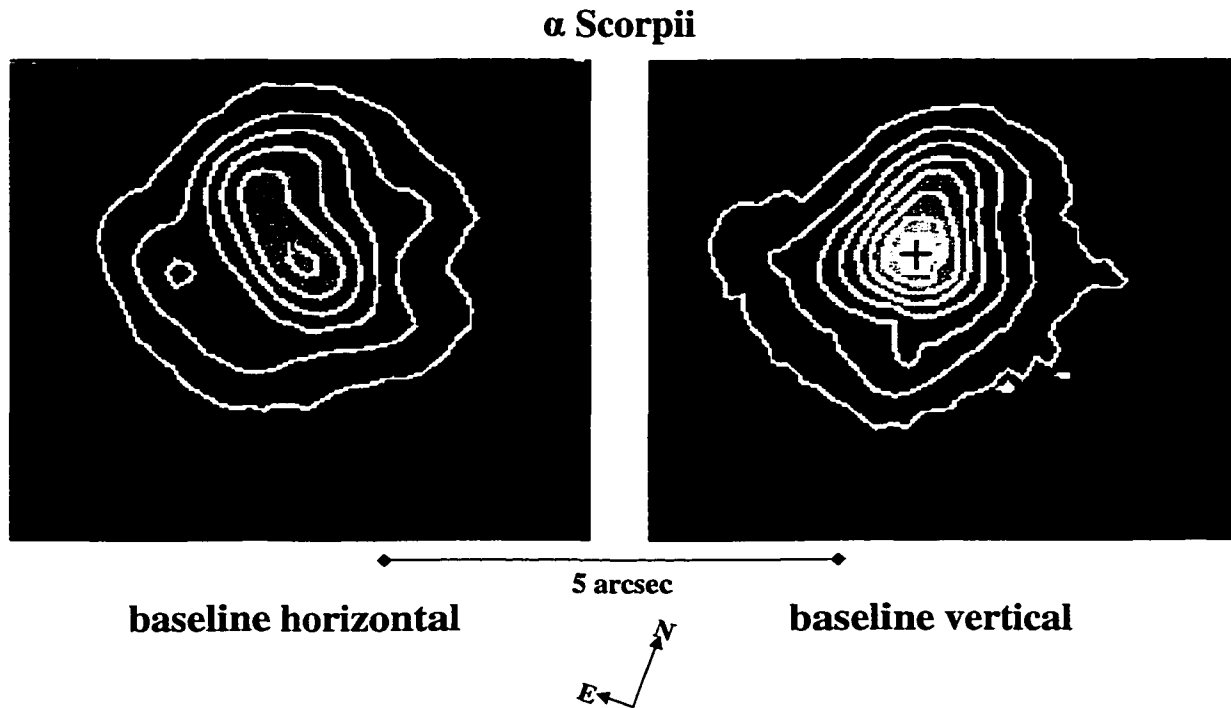


Figure 7.3 Nulled images of  $\alpha$  Scorpii at  $10.3 \mu\text{m}$  wavelength for two different baseline orientations. The center of the stellar emission is marked as a “+” on each image. The lowest contour corresponds to 1% of the constructive stellar peak, with a 1% spacing between contours.

Tuthill et al. 2000). Nulling at  $11.7 \mu\text{m}$  reveals an extended symmetric dust structure. By subtracting the nulled image from the constructive image (Figure 7.5) the point source is revealed to be centered on this emission. However, using the same technique at  $8.8 \mu\text{m}$  the point-like emission is shown to be divided into two sources. The orientation of these two sources corresponds to the two brightest clumps seen in the near-infrared, designated A and D by Osterbart et al (1999). The nulling observations suggest that at  $8.8 \mu\text{m}$  similar structures are dominant

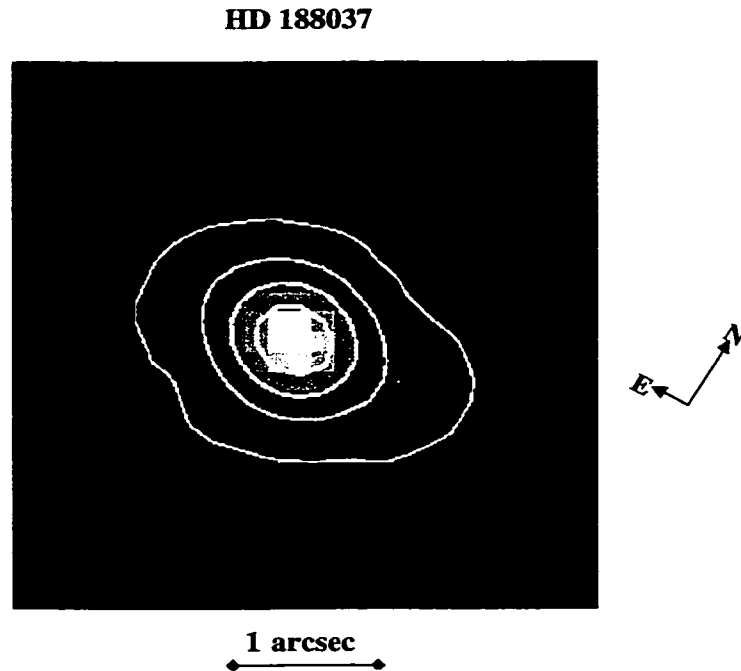


Figure 7.4 Nulled image of HD 188037 at  $10.3 \mu\text{m}$ . The companion,  $0.75''$  away at a position angle of  $274^\circ$ , is shown as a “+” on the image. The grayscale stretch and contours are linear with intensity, with the contours spaced every 20% in intensity from the peak of the image.

in the outflow as in the near-infrared, forming a bipolar-like structure. However at  $11.7\ \mu\text{m}$  the central star, located approximately between the two bright clumps seen in the near infrared and at  $8.8\ \mu\text{m}$ , is the dominant point source in the image.

## 7.5. Herbig Ae/Be Stars

Spectral energy distributions (SED) of pre-main sequence stars such as T Tauri stars and their intermediate mass analogs, Herbig Ae/Be stars, show clear evidence of an extended, cool component providing a significant infrared excess above the stellar emission. This excess is assumed to be in the form of a circumstellar disk (Shu, Adams, and Lizano 1987), but simple, geometrically thin, optically thick models of a disk fail to reproduce the observed spectral energy distribution, underestimating the amount of flux in the mid-infrared. Recent self consistent models (Kenyon and Hartmann 1987, Chiang and Goldreich 1997, D'alessio et al. 1998) which can reproduce the SED have disk geometries with a significant flare to the radial structure of the disk. The surface of the flared disk is exposed to stellar irradiation creating a heated surface layer, or what is usually termed a disk atmosphere. Because of this exposure to the stellar flux, the surface layer is heated to a higher temperature than the underlying disk. In addition to creating emission features, the mid-infrared flux from such models is significantly more extended, making the structure detectable with a nulling interferometer.

### 7.5.1. Model Parameters

The spatial distribution of the infrared emission is determined by the temperature distribution as well as the optical depth of the atmosphere. Chiang and Goldreich

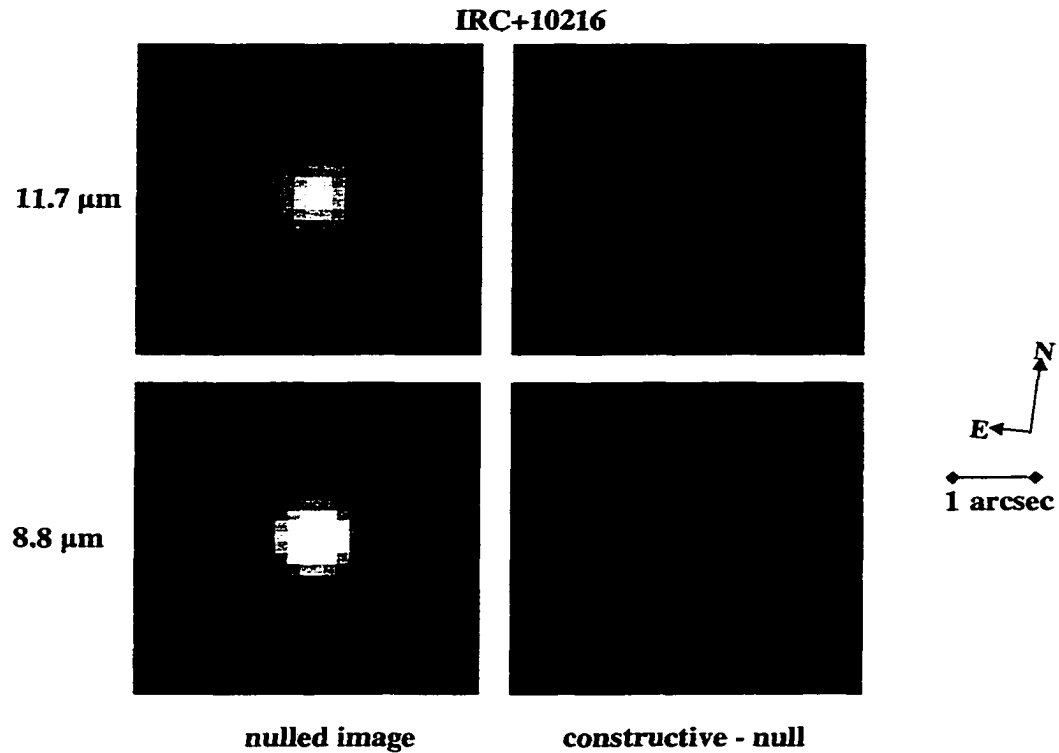


Figure 7.5 Images of IRC+10216 showing the extended and point-like components. The right image in each pair is formed by subtracting the nulled image from the constructively interfered image, effectively showing what is being modulated by the interferometer. The  $11.7 \mu\text{m}$  images show a single central point source which is suppressed in the nulled image. The  $8.8 \mu\text{m}$  image shows the point-like emission which is suppressed in the nulled image is really two sources. The pairs at each wavelength are normalized to the same intensity scale to demonstrate the dominance of the extended structure compared to the point-like emission.



(1997), hereafter CG, derive a temperature distribution for the superheated dust of

$$T_{atm}(r) \simeq T_* \left( \frac{R_*}{2r} \right)^{\frac{2}{5}} \quad (7.6)$$

where  $T_*$  and  $R_*$  are the effective temperature and radius of the central star.

This is significantly less steep than the  $r^{-3/4}$  temperature distribution of a flat, blackbody disk. If the stellar radiation strikes the disk surface at an angle,  $\alpha$ , as shown in Figure 7.6, then the optical depth of the superheated layer is  $\sim \alpha$ , since the stellar radiation will penetrate to an optical depth of approximately unity at grazing incidence. Thus the atmosphere is optically thin in the infrared since the absorptivity of typical grains decreases from the visible (where the stellar radiation peaks) to the infrared. For a disk in hydrostatic equilibrium the grazing angle is a function of distance from the star, given by CG as

$$\alpha = 4 \left( \frac{T_*}{T_c} \right)^{4/7} \left( \frac{r}{R_*} \right)^{2/7} \quad (7.7)$$

for large distances from the star.  $T_c$  is the quantity

$$T_c = \frac{G M_* \mu_g}{k R_*} \quad (7.8)$$

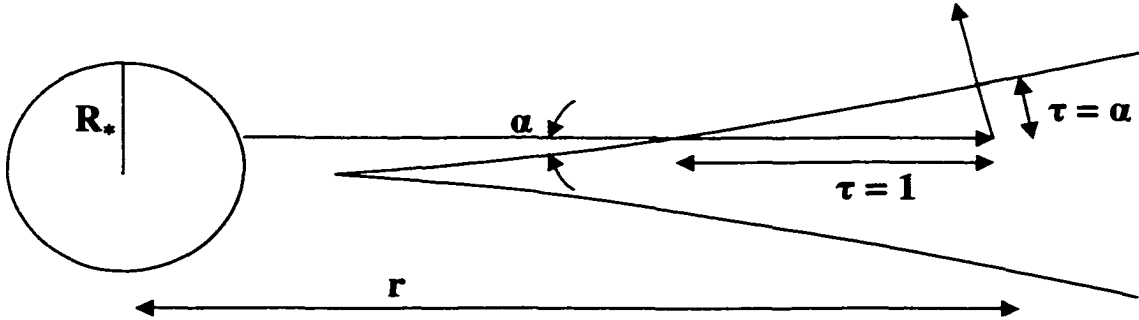


Figure 7.6 Sketch of Herbig disk model.

where  $\mu_g$  is the mean molecular weight of the gas,  $k$  is the Stefan-Boltzmann constant, and  $G$  is the gravitational constant. For an optically thin disk atmosphere the emission contributed by a given annulus,  $dr$ , of a face-on disk is

$$I_\nu(r) = B_\nu(T(r))\alpha r dr \quad (7.9)$$

where  $B_\nu$  is the Planck function. Constants and terms such as the ratio of absorption cross sections at visible and infrared wavelengths are not included since only the distribution of the emission is important for modelling the response of the interferometer, not the total amount.

For stars with parameters similar to those listed in Table 7.3 the  $10.3 \mu\text{m}$  emission is predicted to come from an annulus centered at  $\sim 17$  AU from the star. The response of the interferometer is found by multiplying equation 7.8, scaled appropriately for the distance to the star, by the transmission pattern of the interferometer (equation 2.2) to get

$$I_{null} = 4 \int_0^{r_1} \int_0^{r_1} I_\nu(\sqrt{x^2 + y^2}) \sin^2 \left( \frac{\pi b x}{\lambda} \right) dx dy. \quad (7.10)$$

The equation is easiest to calculate in rectangular coordinates due to the one-dimensional structure of the transmission pattern.  $I_\nu$  is only nonzero for values of  $r > 0.6$  AU, corresponding to the sublimation region of silicate dust near the star. The outer limit,  $r_1$ , is taken to be 500 AU. The model is not sensitive to the exact value of these limits since little flux is produced at the extremes. Since the object size is on the order of the fringe spacing of the interferometer the light detected from the disk at constructive interference must also be calculated. This is given by

$$I_{con} = 4 \int_0^{r_1} \int_0^{r_1} I_\nu(\sqrt{x^2 + y^2}) \cos^2 \left( \frac{\pi b x}{\lambda} \right) dx dy. \quad (7.11)$$

The disk atmosphere is not the only source of infrared emission from the system. The model of CG estimates that 0.3 of the light comes from the optically thick,

cooler disk. The distribution of this emission is close enough to the central star that it can be approximated as a point source. This modifies the expected null by an amount  $\frac{1-0.3}{1+0.3}$  giving a null of 7/13 if the light from the atmosphere is completely resolved. The expected null depth from the total is

$$N = \frac{I_{null}}{I_{con}} \frac{7}{13}. \quad (7.12)$$

The calculated expected nulls for the three Herbig Ae/Be stars are listed in Table 7.3.

Star	Spectral Type	d (pc)	T <sub>*</sub> (K)	R <sub>*</sub> (R <sub>⊙</sub> )	M <sub>*</sub> M <sub>⊙</sub>	Expected Residual Flux
HD150193	A2Ve	150	10000	2.1	2.6	41%
HD163296	A0Ve	122	10500	2.8	3.3	49%
HD179218	B9Ve	240	10000	2.5	3.4	41%

Table 7.3 Model parameters and expected nulls for Herbig Ae/Be stars. Parameters are taken from Hillenbrand et al. (1992) and Meeus et al. (2000).

### 7.5.2. Measurements

As shown in Table 7.4 the measured nulls for three nearby Herbig Ae/Be stars are indistinguishable from the null measured on a point source under the same conditions. Although the level of nulling achievable is not dramatic, due to the presence of atmospheric turbulence, the measurements clearly conflict with typical models of long wavelength emission for Herbig Ae/Be stars.

Meeus et al. (2000) present ISO spectra for a sample of Herbig Ae/Be stars including the three objects observed with the MMT. All three objects show

significant silicate emission features over the  $10.3\ \mu\text{m}$  filter pass band used for MMT observations. The strength of emission is similar for the three stars and contributes approximately 50% of the total flux in each case. The relative equality of the two contributions requires that both sources of the flux, the silicate emission and continuum, each be spatially unresolved, since either one, if extended, would contribute more flux to the null than is detected in the measurements.

Star	Null	Residual Flux	Position Angle
HD150193	$13\pm 5\%$	$0\pm 5\%$	$97^\circ$
HD163296	$12\pm 7\%$	$-1\pm 7\%$	$94^\circ$
HD163296	$16\pm 2\%$	$3\pm 3\%$	$10^\circ$
HD179218	$16\pm 2\%$	$3\pm 3\%$	$162^\circ$
HD179218	$14\pm 2\%$	$1\pm 3\%$	$87^\circ$

Table 7.4 Observations of Herbig Ae/Be stars. The calibrator star for these observations was  $\alpha$  Her with a measured null of  $13\pm 2\%$  using the same integration time as the science objects.

Although the model presented above fails to reproduce the observations, a temperature distribution which falls more steeply with increasing radius would be consistent with observations. However this requires a modification of the model, since the model of CG does not have the exponent of the temperature distribution as a free parameter. One possible change is to assume a different grain size distribution for the dust. The models of CG assume a small grain size ( $0.1\ \mu\text{m}$ ) for the dust to derive the above temperature distribution. If larger grains were dominant in the disk atmosphere the temperature distribution would more closely follow a power law of  $r^{-1/2}$ , causing the annulus of emission to shrink from 17 AU

to 7 AU. This would create a residual flux of approximately 10-15%, marginally consistent with the observations.

### 7.5.3. HD163296

Of the three stars, the most detailed information about the surrounding excess is known for HD163296. Mannings and Sargeant (1997) observed it at 2.7 mm and found an elongated dust disk, at an inclination of  $58^\circ$  approximately 110 AU in diameter with a position angle of  $126^\circ$ . Grady et al. (2000) confirm this structure in the visible with HST, where a disk illuminated by scattered light is seen to have an inclination of  $60^\circ$  and a position angle of  $140^\circ$ . No residual flux is detectable in the nulled image above that of the starlight. The position angles corresponding to the two observations for this star are  $10^\circ$  and  $94^\circ$ . Although neither of these lies along the major axis of the disk, the two observations would still be expected to resolve the disk at the intermediate angles of observation if the mid-infrared emission followed the spatial structure of the model presented above.

## 7.6. Main Sequence stars

Two main sequence stars were nulled during the initial observations: Vega and Altair. Table 7.5 lists the measurements for these objects. IRAS measurements of these two stars detect infrared excess for Vega but not for Altair (Aumann et al. 1984). For Vega the infrared excess is only apparent for wavelengths of  $25\ \mu\text{m}$  and longer. At  $12\ \mu\text{m}$  no excess is detected above photospheric emission from the star. The uncertainty of these measurements is listed as 4% for both stars. In addition the uncertainty in extrapolating the photospheric emission to mid-infrared wavelengths is approximately 3% (Cohen 1996). Thus zodiacal emission around these stars would have to be less than approximately 15% of the stellar flux to be

consistent with these observations. The equivalent number to compare with this limit for nulling is approximately twice the  $3\sigma$  limit to the residual flux, since the emission from the dust is split into the constructive and destructive outputs of the interferometer. This corresponds to 24% for Vega and 20% Altair. Thus, the limit for dust around Altair and Vega is not better than the results from IRAS photometry. However, this limit is a more direct measurement of the excess in the sense that no observations at other wavelengths and models of the photospheric emission are needed to differentiate the stellar from the zodiacal component to the light.

Star	Null	Residual Flux	Wavelength	Position Angle
Vega	$14\pm3\%$	$1\pm4\%$	$11.7\ \mu\text{m}$	$133^\circ$
Vega	$13\pm3\%$	$0\pm4\%$	$10.3\ \mu\text{m}$	$135^\circ$
Altair	$8\pm4\%$	$-5\pm5\%$	$10.3\ \mu\text{m}$	$97^\circ$

Table 7.5 Observations of main sequence stars. The calibrator star for these observations was  $\alpha$  Her with a measured null of  $13\pm2\%$  using the same integration time as the science objects.

#### 7.6.1. Limit to Zodiacal Dust

Using the measurements in Table 7.5 it is possible to place a limit on the strength of the zodiacal cloud around these two stars relative to the level the zodiacal disk in the Solar System. Kelsall et al. (1998) created an 88 component fit to the zodiacal emission measurements of the DIRBE instrument on the COBE satellite which accurately models the mid-infrared flux from dust in our solar system. For our purposes only the smooth cloud component is necessary to predict the level of

detectable zodiacal dust. The density of the zodiacal cloud from this model has a power law dependence on radius and an exponential dependence on the vertical thickness:

$$n = n_0 R^{-\alpha} e^{-\beta g(z/R)^\gamma} \quad (7.13)$$

where  $n_0$ ,  $\alpha$ ,  $\beta$ , and  $\gamma$  are fit by the DIRBE data. The function,  $g(z/R)$  approximates the absolute value of  $z/R$  in the model and is given as

$$g = \begin{cases} (|z|/R)^2 / 2\mu & \text{for } |z|/R < \mu \\ |z|/R - \mu/2 & \text{for } |z|/R \geq \mu \end{cases} \quad (7.14)$$

where  $\mu$  is a free parameter. The fitted temperature distribution of the dust is

$$T(r) = T_0 r^\delta \quad (7.15)$$

where  $T_0$  is the temperature of the dust at 1 AU. The total emission from the dust is given as

$$I = \frac{2\pi}{d^2} \int \int n(r, z) B_\lambda(T(r)) dr dz \quad (7.16)$$

where  $B_\lambda$  is the Planck function and  $d$  is the distance of the system. The model parameters fit by Kelsall et al. (1998) to the DIRBE data are listed in Table 7.6.

At  $10.3 \mu\text{m}$  the model gives an integrated flux of  $110 \mu\text{Jy}$  for a solar level zodiacal dust cloud around a star at 10 pc. For Vega and Altair the detectable level of dust is found by calculating the flux for the appropriate distance, temperature, and size for each star (given in Table 7.7). The temperature of a dust cloud around a star whose effective temperature,  $T_*$ , and radius,  $R_\odot$ , differs from the sun can be scaled by using

$$T_0 = \left( \frac{R_*}{R_\odot} \right)^{1/2} \frac{T_*}{T_\odot} \quad (7.17)$$

for the temperature at 1 AU. This model is multiplied by the transmission function of the interferometer (equation 2.2) to account for the amount of flux observed in

the nulled output of the instrument. The overall density,  $n_0$ , is adjusted to create a level equal to the limit of detection. This value, divided by the solar level density, determines the level of zodiacal dust detectable for a particular system. For Vega the  $3\sigma$  limit on the residual flux of 12%, or 8.4 Jy, corresponds to 3700 times solar using the above model, whereas the IRAS photometric limit corresponds to a limit of 1800 times solar level. For Altair the nulling limit is somewhat better, corresponding to a limit of 2500, whereas IRAS photometry limits the dust to 1800 times solar level.

Parameter	Description	Value
$n_0$	Density at 1 AU	$1.3 \times 10^{-7}$
$\alpha$	Radial power-law exponent	1.34
$\beta$	Vertical shape parameter	4.14
$\gamma$	Vertical power-law exponent	0.942
$\mu$	Widening parameter	0.189
$T_0$	Temperature at 1 AU	286
$\delta$	Temperature power-law exponent	0.467

Table 7.6 Parameter values for the solar zodiacal cloud.

Parameter	Vega	Altair
Spectral Type	A0V	A7IV-V
Temperature	9250K	8250K
Size	$2.4R_{\odot}$	$1.6R_{\odot}$
Distance	7.75 pc	5.15 pc

Table 7.7 Parameters for Vega and Altair. Values are taken from Allen (2000).



Although the limits set by initial observations are similar in level to the limits set by infrared photometry, nulling observations with phase control will improve the sensitivity by several times the current result. With adaptive optics the limit will be one to two orders of magnitude better, dramatically improving the current best estimates of zodiacal dust around nearby stars. The level of dust detectable with future nulling observations will be discussed further in chapter 8.

## CHAPTER 8

### FUTURE OF GROUND-BASED NULLING

With the advent of large aperture interferometers and adaptive optics systems, ground-based nulling has the potential to increase greatly our understanding of planetary systems. The ability of a nulling interferometer to detect companions or zodiacal dust is determined by two metrics: the level of suppression achievable and the photometric sensitivity. The suppression analysis for BLINC in chapter 5 suggests the limit for ground-based nulling is on the order of  $10^{4-5}$  limited by the spatial and temporal correction of the wavefront for the planned MMT AO system. Here, the photometric sensitivity is estimated for ground-based systems as determined by the brightness of the sky background and the telescope emission, and related to the corresponding sensitivity to zodiacal dust and planetary companions.

#### 8.1. Photometric Sensitivity

For ground-based observations nulling is a technique most easily performed in the thermal infrared (3-13  $\mu\text{m}$ ) due to the relaxed requirements on wavefront correction relative to optical wavelengths. For these observations the noise source for the immediate surroundings of a star is different from the optical and near-infrared

(0.5-2  $\mu\text{m}$ ) where limits, using adaptive optics coronagraphy, are typically set by the amount of scattered light introduced by the optics and adaptive optics residuals. These usually show up as long-lived speckles in the focal plane, mimicking faint companions (Ryan et al. 1998, Langlois et al. 1998). Through nulling, scattered starlight and the associated speckle pattern are reduced to well below the noise level associated with the background light contributed by the sky and the warm telescope mirrors. Since this noise source is dominant, a deformable secondary, rather than a conventional AO system, is advantageous not only for the phase correction it performs but also because it does not introduce any extra warm surfaces. Extra surfaces in a conventional AO system add a significant amount of background light in the thermal infrared, decreasing the system's sensitivity.

The background light is dominated by warm telescope emission and sky background. The photons due to the telescope can be modelled as a greybody of emissivity,  $e$ , at the temperature of the nighttime air, 0° Centigrade. Then the received photons per second are

$$n_{tel} = \frac{\nu^2}{c^2} \frac{e \Delta \nu A \Omega}{e^{\frac{h\nu}{kT}} - 1}, \quad (8.1)$$

where  $A$  is the total area of both apertures, and  $\Omega$  is the angular area the energy is spread over in the focal plane, chosen as  $\lambda/D$  in radius. This equation reflects the fact that the background is a factor of two lower than typical telescope background since the light is split equally into the two outputs of the interferometer.

The sky brightness is determined by the details of absorption bands, mainly of water and carbon dioxide, but also including effects from trace gases such as ozone, methane and nitric oxide. The HITRAN database of atmospheric absorption (Allen 2000) provides an accurate model of the sky brightness in the thermal infrared for high altitude observatories. Using these data the brightness across the passbands

can be integrated to determine the sky brightness seen by the detector in photons per second,  $n_{sky}$ . The model of the sky background, along with a 5% emissive telescope background are shown in Figure 8.1

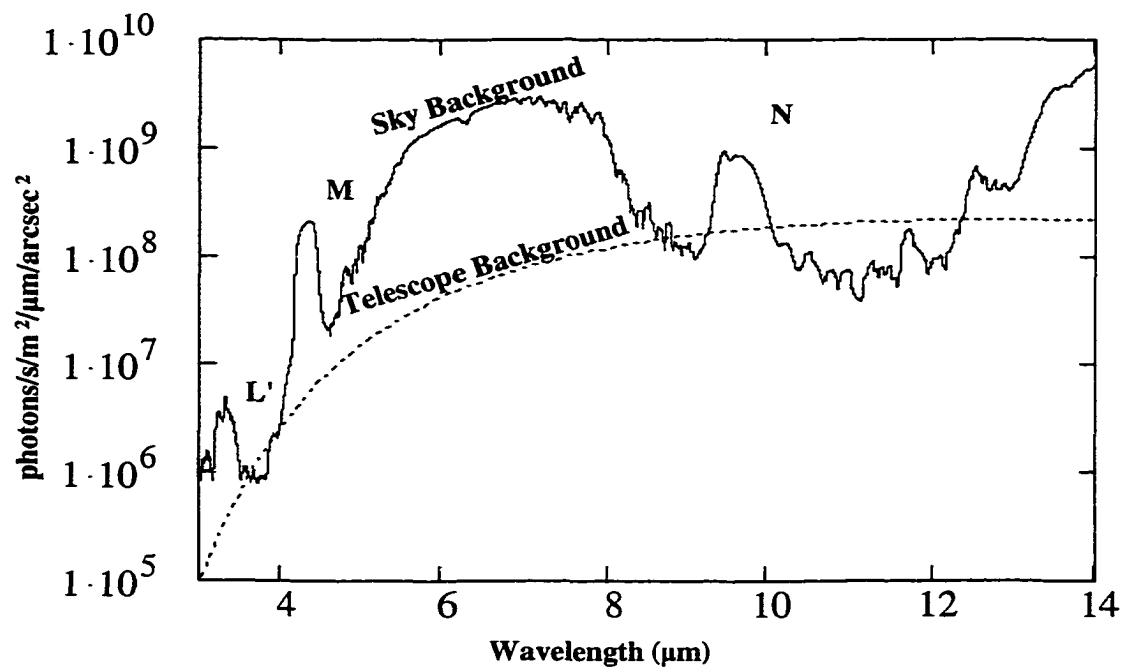


Figure 8.1 Sky and telescope background in the thermal infrared. The telescope background is calculated for a 5% emissive system at a temperature of 0° C.

The values for these two contributions dominate over other sources of error in the mid-infrared, such as detector read noise. If accurate, frequent sky subtraction is performed so that the variation in sky brightness does not affect the measurement, the noise level is given, by Poisson statistics, as the square root of the total number of photons detected. The signal flux is negligible compared with the background so that the minimum signal detectable (in photons/s) at a level 5

times above the noise is

$$s_{min} = 5\sqrt{\frac{n_{tel} + n_{sky}}{t Thpt}} \quad (8.2)$$

where  $t$  is the total integration time and  $Thpt$  is total throughput of the instrument, including the quantum efficiency of the detector. This equation is valid when the signal is above that of the expected residual intensity of the null, as estimated in chapter 3. For signals below this, the detectability is determined by the ability to calibrate the residual intensity of the instrument, as well as the relative position of the object with respect to the star. Being able to confirm a signal through astrometric or spectral information becomes important in this case, allowing detection of signals fainter than the residual starlight.

### 8.1.1. MMT Nulling Sensitivity

When coupled with the adaptive secondary, the MMT nulling interferometer, BLINC, will be capable of probing for the faint zodiacal dust expected around nearby main sequence stars if they have planetary systems. In addition, the interferometer will be capable of detecting massive sub-stellar companions as described below. The sensitivities are calculated for three atmospheric passbands: L', M, and the 10-12.2  $\mu\text{m}$  region of the N band.

At 11.1  $\mu\text{m}$  a telescope emissivity of 5% gives a background flux of  $1.1 \times 10^{10}$  photons/s for a 20% passband. The sky background is very dark in the 10-12.2  $\mu\text{m}$  region, equal to approximately 2% telescope emissivity, or  $3.4 \times 10^9$  photons/s using the same collecting area,  $A$ , and solid angle,  $\Omega$ , for the total sky background. The quantum efficiency of the MIRAC detector is approximately 35% at 11  $\mu\text{m}$ . If we adopt a total throughput of 20% the  $5\sigma$  limit to sensitivity is 660  $\mu\text{Jy}$  per  $\sqrt{\text{hour}}$  of integration.

In the M atmospheric passband the same telescope emissivity yields a background flux of  $1.3 \times 10^8$  photons/s. However, the sky background is dominated by emission from ozone and water creating a relatively high flux of  $4.7 \times 10^8$  over this spectral region and limiting the amount of flux that is transmitted through the atmosphere to  $\sim 70\%$ . Detectors working at  $5 \mu\text{m}$  typically have a higher quantum efficiency in the range of 60-80%. An overall throughput of 50% would allow a  $5 \sigma$  detection of a  $190 \mu\text{Jy}$  source per  $\sqrt{\text{hour}}$ .

The sky is much darker at L band. The sky background in this region results in a sky flux of  $3.5 \times 10^6$  photons/s. The telescope emissivity, then, dominates the noise with a background flux of  $8.2 \times 10^6$  photons/s. This results in a limit of  $18 \mu\text{Jy}$  per  $\sqrt{\text{hour}}$ .

Parameter	MMT	LBT
Emissivity	5%	7%
Element diameter	2.7 m	8.2 m
11.1 $\mu\text{m}$ throughput	20%	50%
M band throughput	50%	50%
L' band throughput	50%	50%

Table 8.1 Telescope parameters for sensitivity calculations.

### 8.1.2. LBT Sensitivity

The BLINC instrument is a prototype for the Large Binocular Telescope (LBT) nulling interferometer. BLINC will develop the methods and techniques for detecting faint structure using nulling. Beginning in 2004 the LBT will be able to search for zodiacal dust and planetary companions at considerably improved

sensitivity with a technique that has been tested and proven on the MMT. The LBT instrument will preserve the simplicity of the current system by having a common mount, thus not requiring delay lines, and deformable secondaries, and resulting in only three warm reflections prior to combination of the light. The LBT nulling interferometer will have the benefit of a larger collecting area with only one additional warm reflection. This will create only a slightly higher emissivity while greatly increasing the number of detected photons from an object. At  $11.1\ \mu\text{m}$  a telescope emissivity of 7% gives a background flux of  $1.6 \times 10^{10}$  photons/s for a 20% passband. The sky background is the same value as for the MMT:  $3.4 \times 10^9$  photons/s. Recent Si:As detectors produced by Boeing have a quantum efficiency of 80-90%, a significant improvement over the previous generation. If the total throughput is set at 50% the  $5\ \sigma$  limit to sensitivity is  $45\ \mu\text{Jy}$  per  $\sqrt{\text{hour}}$  of integration.

In the M band a 7% telescope emissivity yields a background flux of  $1.8 \times 10^8$  photons/s. The sky background, again, is the same as the MMT at  $4.6 \times 10^8$  photons/s over this spectral region. For a throughput of 50% the  $5\ \sigma$  detection limit is of a  $22\ \mu\text{Jy}$  source per  $\sqrt{\text{hour}}$ .

The telescope emissivity in the  $L'$  band corresponds to a background flux of  $1.2 \times 10^7$  photons/s which, with the same sky flux as for the MMT, sets the detectable flux limit at  $2.1\ \mu\text{Jy}$  per  $\sqrt{\text{hour}}$  for the LBT.

## 8.2. Science Goals

As discussed in chapter one, nulling will be most useful in detecting exo-zodiacal dust and companions. Probing planetary systems will have two components: detecting zodiacal dust disks at  $11\ \mu\text{m}$ , where they are relatively bright, and

detecting extrasolar giant planets in the 4-5  $\mu\text{m}$  region. Giant planets are most easily found at 5  $\mu\text{m}$ , since they are anomalously bright in this region, both as evidenced by the spectrum of Jupiter and by theoretical models of giant planets (Burrows et al. 1997). The strength and existence of zodiacal dust are important in determining whether a planetary system exists around a particular star as well as whether it will be possible to find terrestrial-type, life bearing planets in the future with a TPF mission (Woolf and Angel 1995). A very bright zodiacal dust disk could make the detection of an Earth-like planet with TPF much more difficult, both from confusion of dust clumps in the cloud with planets and from the added background noise it introduces.

### 8.2.1. Zodiacal Dust

The DIRBE model of our own zodiacal dust (Kelsall et al. 1998) provides a good estimate of what level of sensitivity can be expected for dust around nearby stars. The model is described in chapter 7. The overall density of the cloud is adjusted to produce a value for the integrated flux in the mid-infrared. The density compared to solar level is referred to as the “zodi” level of the cloud. The detectable flux for a cloud is a function, not only of the spectral type of the star and distance,

	MMT( $\frac{\mu Jy}{\sqrt{hr}}$ )	LBT ( $\frac{\mu Jy}{\sqrt{hr}}$ )
10-12.2 $\mu\text{m}$	660	45
M band	190	21
L' band	18	2.1

Table 8.2 Photometric sensitivity limits of the MMT and LBT nulling interferometers. The levels correspond to  $5\sigma$  above the noise level of the system.



but of the baseline of the interferometer. Along with nulling out the star, the interferometer will suppress the central part of the dust cloud. By multiplying the intensity distribution of the cloud (equation 7.15) by the transmission of the interferometer (equation 2.2) prior to integration, this effect can be accounted for. Figure 8.2 shows the level of flux which would be measured with the MMT interferometer versus cloud density for stars with a range of spectral types at 10 pc. As can be seen, the detectable level of flux is dependent on the spectral type of the star, since this determines the spatial extent of the dust corresponding to roughly 300 K, and thus how much surface area is emitting mid-infrared radiation.

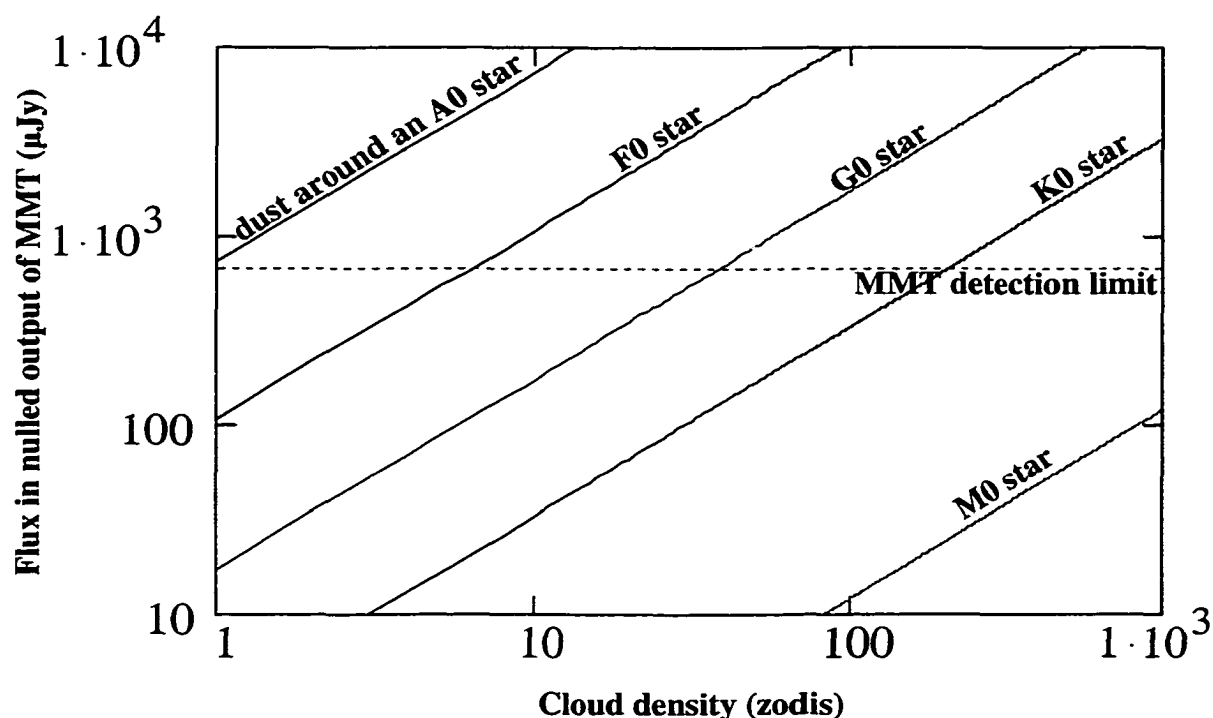


Figure 8.2 Transmitted flux of zodiacal dust at the MMT for different spectral types at 10 pc.

Clouds around A0 stars would be detectable down to 1 zodi, G0 stars would need  $\geq 40$  zodis of dust, while a dust cloud around an M0 star at 10 pc would need to be nearly 6000 times solar level. Figure 8.3 shows the equivalent plot for the LBT instrument. The longer baseline of the LBT allows it to detect the hotter dust closer in to a star which the MMT instrument partially suppresses. At 10 pc the LBT is sensitive to dust  $> 0.8$  AU from the star. This effect, along with the greater photometric sensitivity, allows it to be sensitive to solar level dust for stars with a spectral types as late as G5 at a distance of 10 pc.

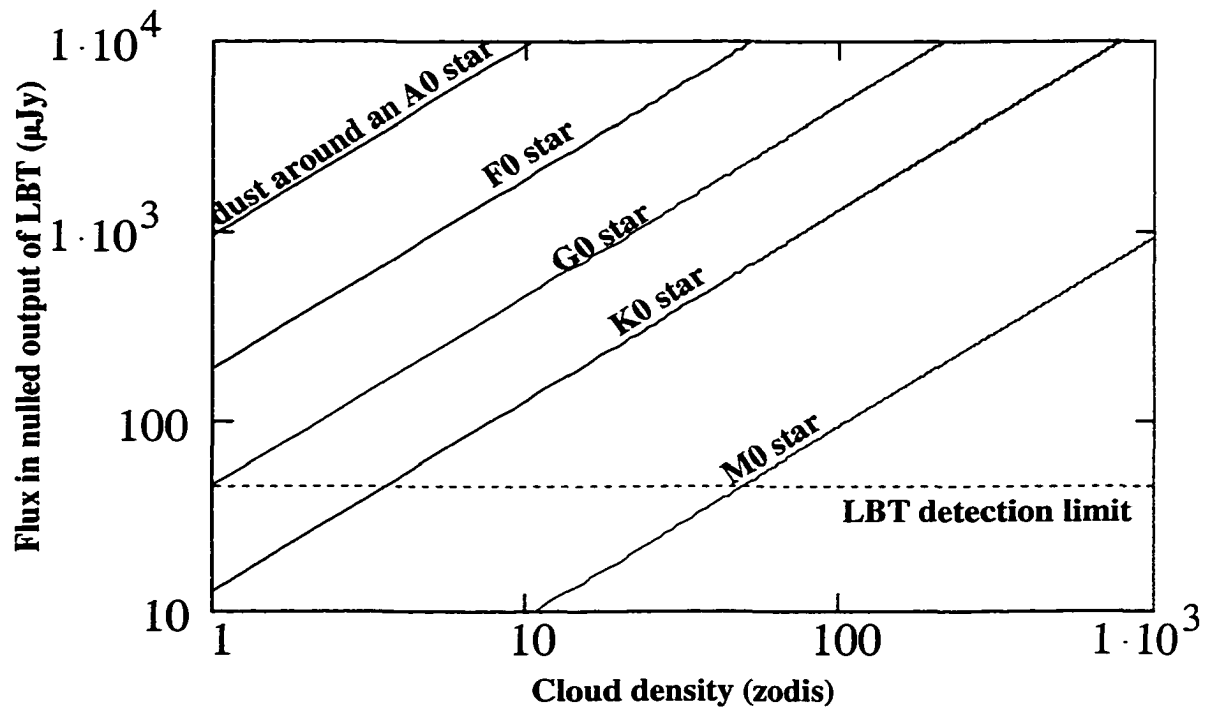


Figure 8.3 Transmitted flux of zodiacal dust at the LBT for different spectral types at 10 pc.

A strength of the MMT nulling instrument is its ability to create a deep null for even the closest stars due to its short baseline. The achievable level of null, if the level is dominated by the diameter of the star, is 13 times better than the LBT and 450 times better than the Keck interferometer, using equation 3.29. Since the dust around these stars will also be brighter, due to their being closer, the nearest stars, earlier than spectral type M, are especially interesting for nulling observations with the MMT. Table 8.3 lists the parameters and detectable levels of dust for all northern hemisphere stars within  $\sim 5$  pc and earlier than M0.

Star	Spectral Type	Distance (pc)	Dust Limit (zodis)	Star Leak (fraction)
Sirius	A1 V	2.64	0.07	$9.4 \times 10^{-5}$
$\epsilon$ Eri	K2 V	3.22	9.9	$1.0 \times 10^{-5}$
61 Cyg A	K5 Ve	3.48	29	$7.0 \times 10^{-6}$
61 Cyg B	K7 Ve	3.50	50	$6.0 \times 10^{-6}$
$\alpha$ CMi	F5 IV-V	3.50	0.85	$2.3 \times 10^{-5}$
$\tau$ Ceti	G8 Vp	3.65	6.6	$9.5 \times 10^{-6}$
Gl380	K2 Ve	4.87	34	$4.4 \times 10^{-6}$
$\omega$ 2 Eri	K1 Ve	5.04	29	$4.3 \times 10^{-6}$
70 Oph	K0 Ve	5.09	23	$4.6 \times 10^{-6}$
Altair	A7 IV-V	5.14	0.6	$1.6 \times 10^{-5}$

Table 8.3 Detectable limits of dust around the nearest stars with the MMT nulling interferometer. The limits in zodis correspond to the photometric limit of  $660 \mu\text{Jy}$  at  $11.1 \mu\text{m}$ .

### 8.2.2. Giant Planets

Planet searches are important, not only for understanding how common or rare they are, but for understanding the typical distribution in orbital radius and mass of companions. Giant planets, in addition to signalling the existence of a planetary system, by their placement and orbital parameters, determine the suitability of the system for harboring smaller Earth-like planets in stable orbits. Such information is important in assessing which planetary systems might be the most promising to search for life-bearing planets.

Direct detection of a companion is more feasible in the thermal infrared than the visible, since the planet's thermal emission in the infrared is brighter, in comparison to the stellar emission, than the amount it reflects in the visible. However, by looking for a planet in the infrared where it is emitting its own radiation rather than the reflected light from its star, the detectability of a giant planet is sharply dependent on how old it is, and thus how much it has had a chance to cool. Burrows et al. (1997) have created nongray atmosphere models for substellar companions with temperatures in the range 100-1300 K. They present spectra of giant planets as a function of surface gravity and temperature. By modeling how these bodies cool and contract with time they generate a grid of brightness estimates for atmospheric passbands, including N, M, and L'. Figure 8.4 shows an interpolation of their predictions for a 5 Jupiter mass object at 10 pc from an age of 0.1-1 Gyr in the N, M, and L' bands along with the plotted MMT sensitivity limits. As can be seen, the N band sensitivity is insufficient to detect the object at any age, M band observations could detect it if it were younger than 0.5 Gyr, while the L' band would allow detection out to 0.7 Gyr. The L' and M band offer significant advantages in sensitivity in looking for giant planets over

the N band. Again interpolating the models of Burrows et al. (1997) Figure 8.5 shows the L' band fluxes of giant planets as a function of mass for 0.5, 1, and 5 Gyr old objects at 10 pc along with the MMT and LBT limits. From these it is possible to derive mass limits for detection with each instrument, as summarized in Table 8.5. These numbers are expected to be only mildly dependent on the planet-star separation since the source of noise is the thermal background of the telescope. The closest separation nulling can sense is determined by the separation of the apertures, and is  $0.10''$  for the MMT and  $0.027''$  for the LBT in the L',

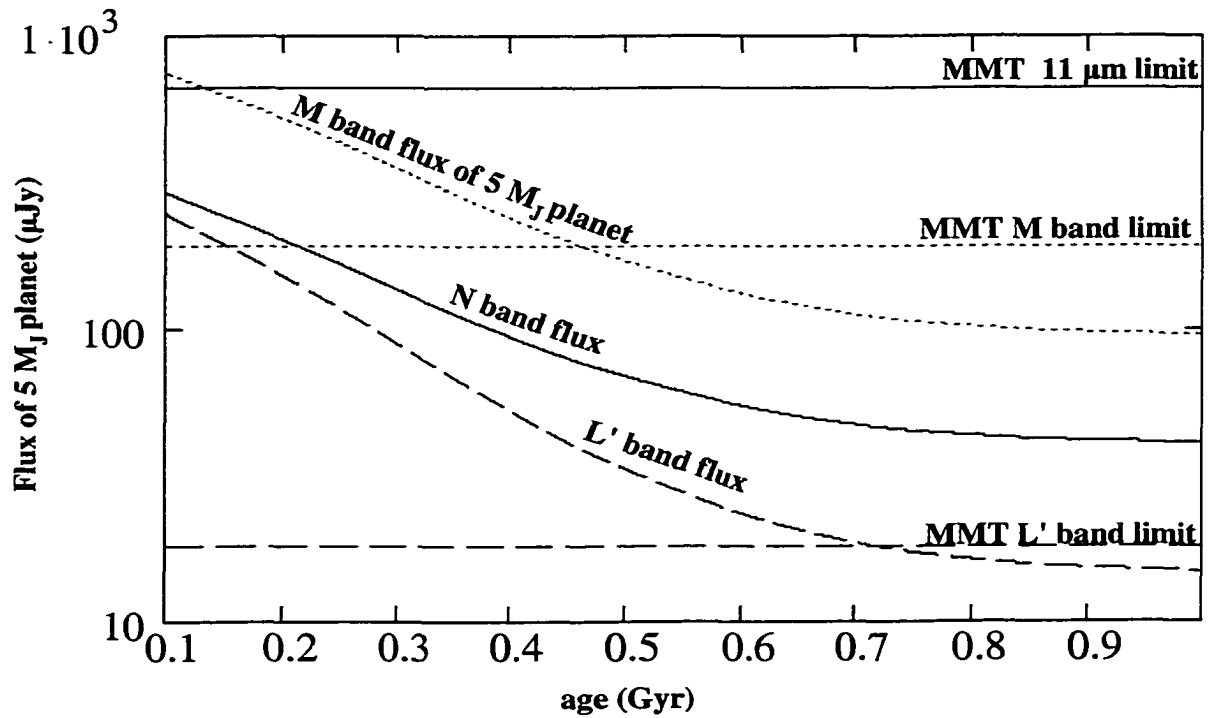


Figure 8.4 Detectability of planets in the N, M, and L' bands. The fluxes, from Burrows et al. (1997), are for a 5 Jupiter mass at 10 pc. The planet is most readily detectable in the L' band.

corresponding to 1 and 0.3 AU, respectively, at 10 pc.

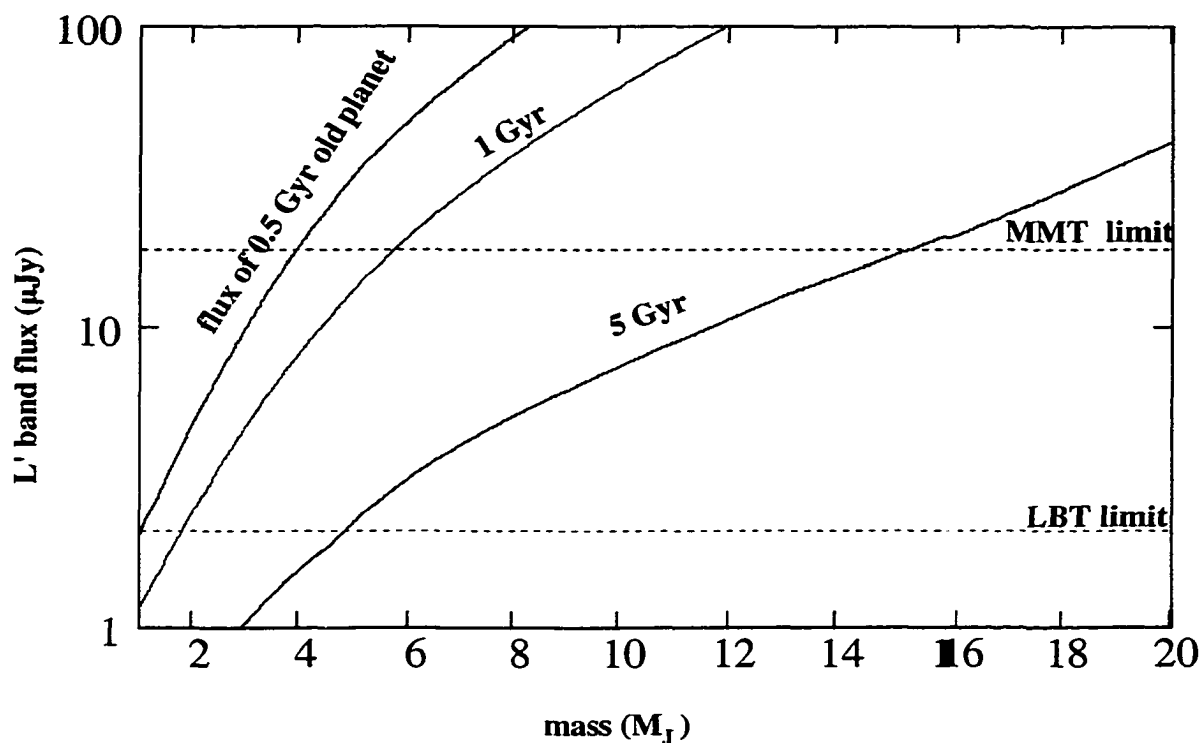


Figure 8.5 Minimum planet mass detectable at  $L'$  for the MMT and LBT. Fluxes are for objects at 10 pc.

Close-in to the star, where calibration issues can compromise the detectability of companions, it will be important to have a robust method of differentiating the planet from the star signal. A G star at 10 pc is approximately  $10^4$  Jy in  $L'$ . Even a  $10^4$  rejection will leave a 1 mJy source, 50 times brighter than the MMT detection limit. However, the planet signal can be modulated, either by sky rotation or rotation of the pupils on the MMT primary. In addition the astrometric shift of the star as it is nulled can verify detection. A source at the limit of detection, 20

$\mu\text{Jy}$ , and  $0.1''$  from the star would produce an astrometric shift of 2 mas, a small but measurable shift in the stellar residual.

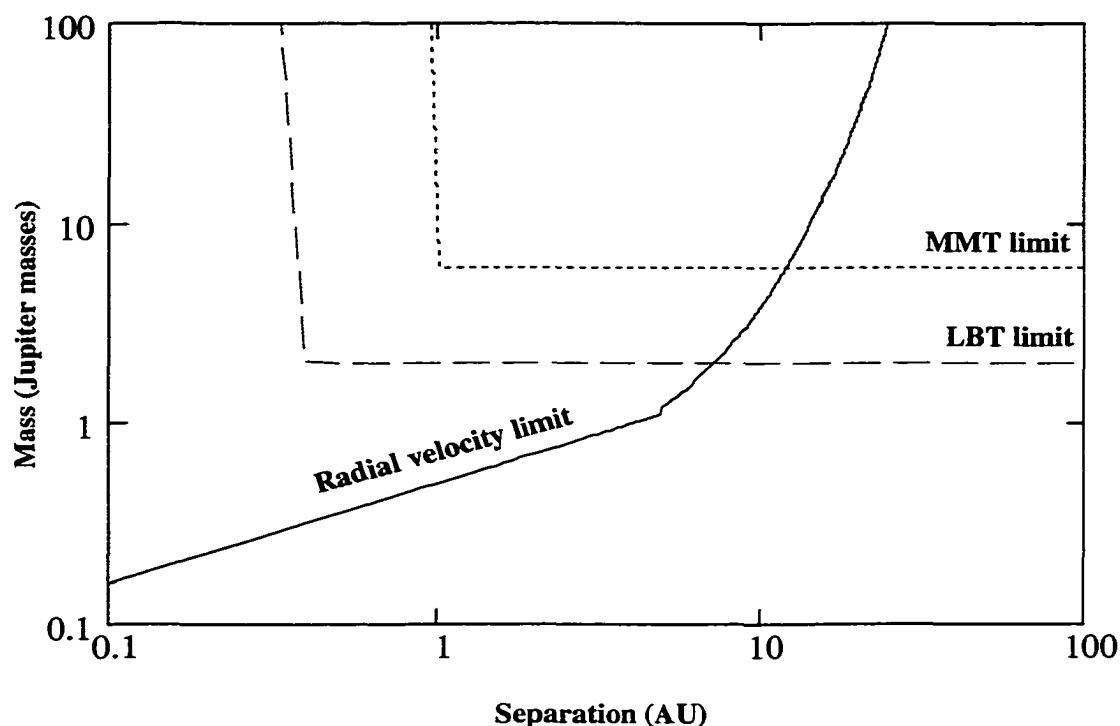


Figure 8.6 Comparison of parameter space for nulling and radial velocity detections. The radial velocity limit is for a 10 year search with a precision of 5 m/s.

The usefulness of direct detection in studying planetary systems can be seen by comparing the expected sensitivity of nulling searches to indirect methods of detecting planets, such as Doppler velocity searches (Figure 8.6). Since the detected parameter in this case is the planet's effect on its star due to orbital motion, planets closer in are much more readily detectable. Thus, although 51 Pegasi was a surprise compared to what was expected for planet detections, it is

not unusual that it was discovered before a similar size planet in an orbit like that of Jupiter. Direct detection, by sensing the planet emission directly is, if anything, less sensitive to close-in planets due to the increased difficulty of separating it from the stellar emission. This results in the technique being complementary to Doppler velocity searches. This is important for creating a balanced view of the makeup of planetary systems. It is also complementary in the sense that younger stars are less able to be probed by radial velocity searches due to stellar activity. The youthfulness of such systems would be expected to have warmer giant planets leading to direct detection more easily than older planets around stars probed by radial velocity searches.

Finding long-period giant planets is interesting for more than just the detection of planetary systems. As discussed by Lunine (2000) giant planets in long-period orbits are important dynamically for the characteristics of the system. For example, a low eccentricity, long period orbit is thought to be important in a planetary system for providing a dynamically stable region for terrestrial planets (Jones, Sleep, and Chambers 2001). In addition the existence of a giant planet near the ice line of a planetary system is probably necessary for perturbing ice-bearing planetessimals into collision orbits with terrestrial planets, providing them with water and volatiles early in their history (Petit et al. 2000). Thus the placement and parameters of a long period giant planet will be informative in understanding the likely existence and habitability of terrestrial planets in that system.

### 8.3. 2020 Telescope

The next generation of ground-based telescopes is currently envisioned as having an overall collecting area of  $\sim 700 \text{ m}^2$ , compared to the  $110 \text{ m}^2$  of the LBT,



which has the most collecting area of those under construction. The “Decadal Review” (2000?) recommended a telescope of this class as a priority for funding over the next decade. Although this collecting area could all go into one single telescope, as envisaged for example, in the design of the California Extremely Large Telescope (Nelson et al. 2000), there are significant advantages to having a two element interferometer, each 20 m in diameter, as proposed by Angel et al. (2001). For planet finding a two element, short baseline interferometer has the unique capability of deep suppression of the starlight combined with improved photometric sensitivity over the LBT. Extrapolating the sensitivity from Table 8.2 we can expect a sensitivity of  $7 \mu\text{Jy}$  per  $\sqrt{\text{hour}}$  for the 10-12.  $\mu\text{m}$  region and  $0.3 \mu\text{Jy}$  per  $\sqrt{\text{hour}}$  for  $L'$ .

Since the photometric sensitivity would be greatly improved for a nulling interferometer with such large apertures, the detectable level of flux is significantly below the level of flux expected from “star leak”. In such a situation it is most important to be able to isolate a companion signal from the contaminating starlight. This can be done spectrally, or by phase chopping.

The spectral discrimination is dependent on understanding precisely the source of stellar leak. If the source is the finite diameter of the star, for example,

	MMT	LBT
Minimum mass at 0.5 Gyr	$4 M_J$	$1 M_J$
Minimum mass at 1 Gyr	$6 M_J$	$2 M_J$
Minimum mass at 5 Gyr	$15 M_J$	$5 M_J$

Table 8.4 Detectability of planets at 10 pc at  $L'$  band.

the wavelength dependence is determined by equation 3.29, and could expect to be calibrated out. If, however, the source of error is adaptive optics errors or chromatic phase errors, the dependence with wavelength could be less well determined, making this more difficult.

Phase chopping was first suggested for multiple element nulling interferometers by Woolf et al. (1998) to isolate planetary signals from exo-solar zodiacal dust in space-based systems. The concept uses two pair of nulling interferometers. Each pair nulls the star, but the two nulled outputs are combined at different phase shifts to modulate the planet signal, isolating it from any slowly varying signal in a manner analogous to sky chopping used for ground-based telescopes. This phase chopping is achievable with a large two element system by splitting each aperture into two, just as BLINC does with the MMT, so that a total of four elements is available for combination.

Assuming such discrimination would permit detection at the photometric limit of the telescope, one of the most exciting possibilities is the detection of Earth-like planets around the very nearest (3-5 pc) stars. Since an Earth-like planet, 10 pc away, emits approximately  $0.4 \mu\text{Jy}$  in the 10-12.2  $\mu\text{m}$  region (Beichman, Woolf, and Lindensmith 1999), a large 20 m telescope could expect to detect a planet at this limit after 2 hours if it were around, for example,  $\epsilon$  Eridani or  $\tau$  Ceti.

Single aperture systems could expect to achieve the same photometric sensitivity and be able to suppress the starlight to a similar level using single aperture nulling techniques (Baudoz et al. 1999), but would not be sensitive to an astrometric shift or be able to modulate the light from a planet.

Although significant work remains to be done in proving the technique, nulling promises to be a valuable technique for observations of planetary systems. Although

originally planned as a space-based technique, it is likely that the significant work over the next decade in using the technique will be with ground-based instruments. Refining the technique with the succession of telescopes described above will help to set the stage both scientifically and technically for a space-based mission to search for the existence and habitability of extra-solar Earths.

## CHAPTER 9

### DESIGN CONSIDERATIONS FOR THE TERRESTRIAL PLANET FINDER

The work described in previous chapters is an essential prelude to space missions to look for planets through direct detection. Ground-based work helps to refine the technology as well as probe circumstellar regions to faint levels. This chapter addresses design considerations for space-based interferometers which use nulling techniques. I discuss different array configuration and how they affect performance of the interferometer. The optical setup of a beam-combiner is sketched out for an example configuration to illustrate the important issues. Finally, a new method of achieving an achromatic null is presented which has some important advantages over previously proposed techniques.

The Terrestrial Planet Finder (TPF) mission (Beichman, Woolf, and Lindensmith 1999) has been envisioned as a space-based multiple pair nulling interferometer working in the thermal infrared to detect and characterize spectroscopically planets down to the size of Earth around nearby stars. The goal of the mission is to determine the frequency and habitability of Earth-size planets, as well as be able to probe them for signs of life.

### 9.1. Configuration Design

A general optimization issue for TPF which has not been fully explored is the configuration of an interferometer. Specific issues have been addressed such as breadth of the null (Angel and Woolf, 1997), asymmetric beam-patterns (Leger et al. 1993), and the ability to chop the planet signal (Woolf et al. 1998). While solutions have been proposed to deal with each of these a systematic optimization will ensure that the required performance of the interferometer is achieved with the minimum number of elements, keeping the beam combination and control for multiple elements as straightforward as possible.

The beam pattern of an interferometer is given by the vector sum of the light from each element of the system. For a one-dimensional interferometer the complex amplitude is

$$A_{tot}(\theta) = \sum_m A_m e^{2\pi i s_m \theta} \quad (9.1)$$

where  $\theta$  is the angle from the pointing center of the array perpendicular to the baseline,  $A_m$  is the complex amplitude of the  $m$ th element corresponding to the size of the aperture ( $Amp_m$ ) and its phase shift ( $\phi_m$ ), and  $s_m$  is its spacing (expressed in waves). The variables are only defined in reference to a fiducial element of amplitude 1, zero spacing, and zero phase shift. So for an  $n$  element interferometer there are  $2(n - 1)$  variables, counting the complex variable,  $A_m$  as one.

For the case of a two element interferometer we can satisfy two constraints. If we constrain it to have destructive interference on axis ( $A(0)=0$ ) this requires a second element with the same amplitude and the opposite phase as the first (a complex amplitude of -1). The second constraint is that at some angle,  $\alpha$ , away it constructively interfere ( $A(\alpha) = 1 + Amp_2$ ). Then the second element is spaced at a distance  $1/2\alpha$  from the first element as is expected, since this describes the

original concept of Bracewell for a nulling interferometer.

In terms of equation 9.1 above, the useful qualities of a nulling interferometer are expressed by the constraints

$$A(0) = 0 \quad (9.2)$$

$$A(\alpha) = 1 + \sum Amp_m \quad (9.3)$$

$$\frac{d A(0)}{dx} = 0 \quad (9.4)$$

$$\frac{d^2 A(0)}{dx^2} = 0 \quad (9.5)$$

$$A(-\alpha) = 0 \quad (9.6)$$

These equations correspond, respectively, to an on-axis null, fully constructive interference, a wide null ( $\theta^4$ ), a super-wide null ( $\theta^6$ ), and an asymmetric beam pattern, capable of chopping. The second constraint is really  $n - 1$  constraints since each complex amplitude on the left side of the equation has to equal  $Amp_m$  for the corresponding element at the angle of constructive interference.

For a three element interferometer there are four free parameters. Two are needed to satisfy equation 9.3 above, and one to satisfy equation 9.2 leaving one free parameter to satisfy an additional constraint. Choosing 9.4, we can derive the amplitude, phase shifts and spacings needed to satisfy these equations. It is instructive to derive the results for this in detail. Equation 9.2 is given as

$$1 + A_1 + A_2 = 0 \quad (9.7)$$

which can be rewritten as

$$A_2 = -1 - A_1. \quad (9.8)$$

Equation 9.4 for a three element interferometer is

$$A_1 s_1 + A_2 s_2 = 0 \quad (9.9)$$

which, in combination with equation 9.8 can be solved to get

$$A_1 = \frac{s_2}{s_1 - s_2}. \quad (9.10)$$

Equation 9.3 gives the two constraints

$$Amp_1 = A_1 e^{-2\pi i s_1 \alpha} \quad \text{and} \quad Amp_2 = A_2 e^{-2\pi i s_2 \alpha} \quad (9.11)$$

so that

$$Amp_1 = \left| \frac{s_2}{s_1 + s_2} \right| \quad \text{and} \quad Amp_2 = \left| \frac{s_2}{s_1 + s_2} - 1 \right|. \quad (9.12)$$

The complex phase of the right side of equation 9.11 has to be  $2\pi n$  to create a positive real value, where  $n$  is an integer. The phase is determined both by the spacing and phase of the element. Solving for the spacing we get

$$s_1 = \frac{a - \phi_1}{\alpha} \quad \text{and} \quad s_2 = \frac{b - \phi_2}{\alpha} \quad (9.13)$$

where  $a$  and  $b$  are integer values and  $\phi_1$  and  $\phi_2$ , expressed in waves, are constrained to be zero or  $1/2$ , depending on the signs of equations 9.8 and 9.10. Since  $a$  and  $b$  can take on any value the equations do not have a unique solution. However taking  $a = 1$  and  $b = -1$  a solution is found with  $Amp_1 = Amp_2 = 0.5$  and  $\phi_1 = \phi_2 = 0.5$ , creating an equal spacing interferometer with side elements which have a diameter half as large as the central one. Different values for  $a$  and  $b$  can be chosen, but the solutions either result in solutions with one amplitude as zero or create interferometers with wider spacings, making the choice of 1 and -1 the best solution. This configuration is often referred to as a degenerate Angel cross (DAC) since it can be thought of as a 1-dimensional version of a 4 element 2-dimensional array first suggested by Angel (1990) to give a wide null. Its transmission pattern is shown in Figure 9.1.

If, instead of equation 9.4, 9.6 is chosen as the additional constraint, a similar derivation gives equal spacing of the elements of phase shifts  $\pm 2/3$  of a wave.

However, 9.6 is an overly strict constraint. If instead the constraint is given as  $(A(-\alpha) \neq 1)$  more flexibility is possible in the configuration. One change would be to vary the spacing between the elements so that different spatial frequencies are sampled by the different pair combinations. Figure 9.1d shows an example of such an array, with a 3:2 ratio between the two spacings which satisfies the constraints of a three element nulling interferometer with an asymmetric transmission pattern. An asymmetric pattern is advantageous for differentiating structure which is only on one side of the star (such as a planet) from a signal which is symmetric around the star (such as zodiacal dust). It also permits phase chopping, which is the modulation of the transmission pattern to keep the null centered on the star while changing the side which the closest constructive peak is on from the positive to negative angle.

An example of a four element chopping array is shown in Figure 9.2a. While this array uses an extra element to satisfy the same constraints as the three element versions, the equal amplitude and  $1/4$  wave phase shifts of the elements could provide advantages in implementation compared to the three element cases. This configuration was suggested by Woolf et al. (1998) as a simple TPF precursor mission. It is usually referred to as a double Bracewell, since it is essentially two interleaved nulling interferometers with a  $1/4$  wave phase shift between the two pairs.

Angel and Woolf (1997) proposed a four element design (shown in Figure 9.2b), usually referred to as the OASES design, with a null which varies as  $\theta^6$  near the null. Such a wide null efficiently suppresses the light from the star while having a constructive peak close enough to the star to be sensitive to Earth-like planets. The array can be shown to satisfy equations 9.2, 9.3, 9.4, and 9.5. This



corresponds to six constraints, which is an optimum use of the number of degrees of freedom for a four element array. If instead a design is required with a  $\theta^4$  null but an asymmetric transmission pattern the equations can be solved to get the result shown in Figure 9.2c. The spacings correspond to approximately -16.6, 0, 13.0, and 29.5 m, with corresponding phase shifts of 146, 0, -114, and -260 degrees.

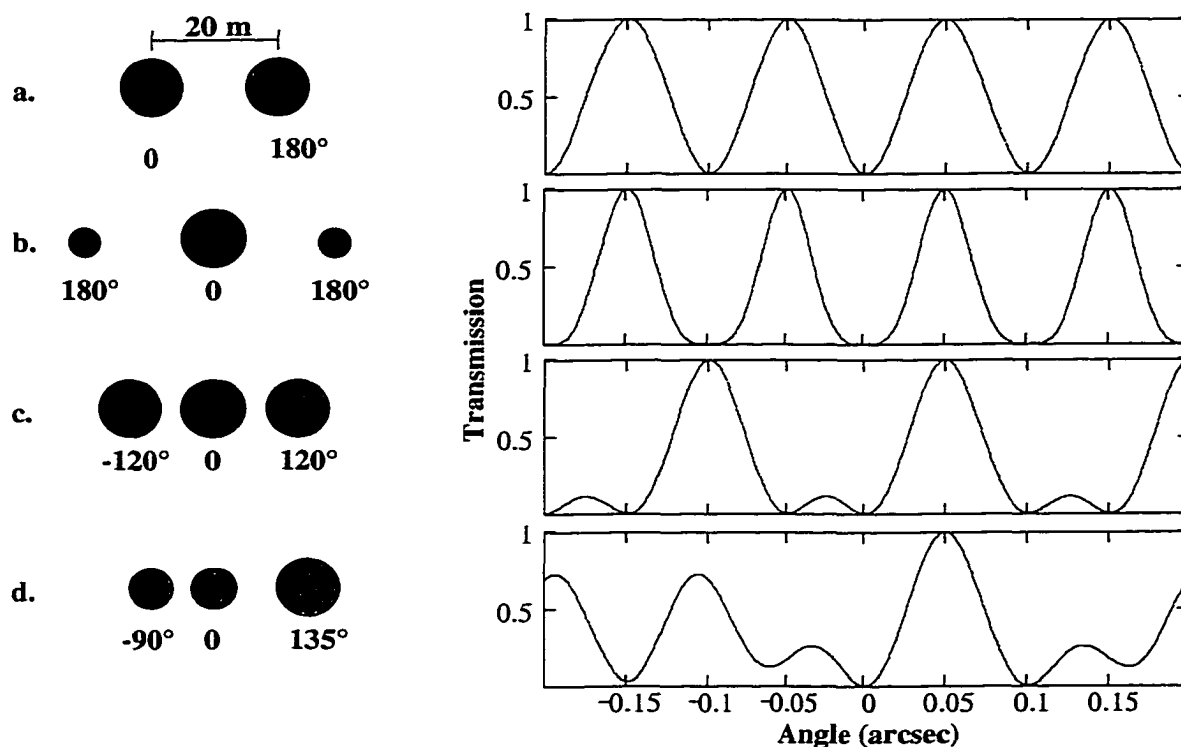


Figure 9.1 Transmission patterns for three-element arrays. The diameter of the elements corresponds to the amplitude of each telescope with the phase shifts listed below. The overall length of each array is scaled so that the transmission pattern has its first constructive peak at 0.1 arcsec for 10  $\mu\text{m}$  wavelength.

Like the three element solution, this configuration is overly constrained by the asymmetry equation, allowing some flexibility in modifying the configuration to a more conventional spacings and phase shifts. Previous arrays have been proposed to create the same capabilities, but use six elements to achieve the same result. A four element system would reduce the complexity of beam combination and allow higher throughput for the system.

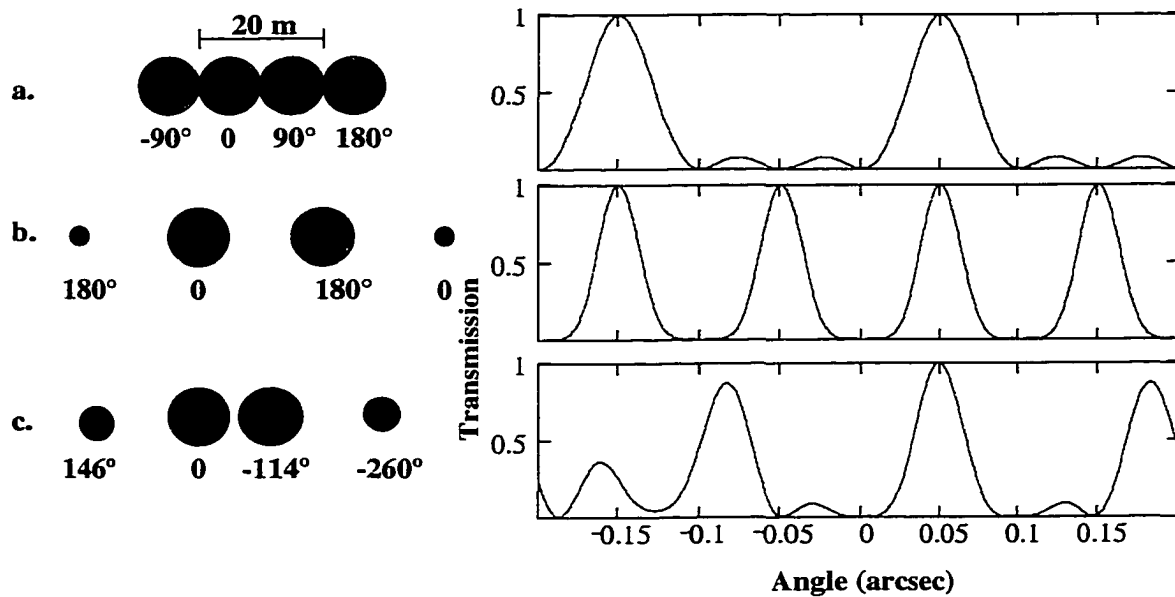


Figure 9.2 Transmission patterns for four-element arrays. The diameter of the elements corresponds to the amplitude of each telescope with the phase shifts listed below. The overall length of each array is scaled so that the transmission pattern has its first constructive peak at 0.1 arcsec for 10  $\mu\text{m}$  wavelength.

## 9.2. A Strawman Optical Design for TPF

The optical setup of a multi-pair nulling beam-combiner is dependent on the interferometer configuration, but a beam-combiner will have common features for just about any configuration. The beam combination design for BLINC can be extended to multiple element designs to illustrate the relevant issues. For this purpose two beam-combiners for linear configurations, an OASES configuration, and a double Bracewell setup are presented in Figure 9.3 and 9.4. This illuminates some of the control issues associated with the combiner, as well as how the configuration impacts the optical design of the combiner. Some assumptions are required to sketch a design. It is assumed the combiner will use dielectric plates to achieve the achromatic null (Angel, Burge, and Woolf 1996). If another method is chosen to obtain the null (such as rotation shearing (Shao and Colavita 1992)) the combiner will become more complex. The main increase in complexity is the fact that two nulled outputs are produced in the rotation shearing concept. It is assumed a single-pass beam-splitter can be used which may not be possible. Finally, it is assumed, for simplicity in the drawing, that the full spectral range (expected to be 7-17  $\mu\text{m}$  for TPF) can be handled by a single combiner, rather than split into channels prior to nulling. Again, this may not be realistic. These assumptions and the specific examples are meant only to help clarify what a beam-combiner might entail, in terms of complexity.

The collectors are not shown in the diagrams. The collectors will take care of proper baffling of the beam (pupil stop and cold stop) and create a beam-size suitable for handling by the combiner. The first fold mirror in each beam is meant to be the "tertiary" mirror of the collector which sends the beams to the combiner. The beam-combiners are not drawn to scale but the relative path-lengths involved

are kept proportional. Beam folding will be needed to package the beam-combiner properly.

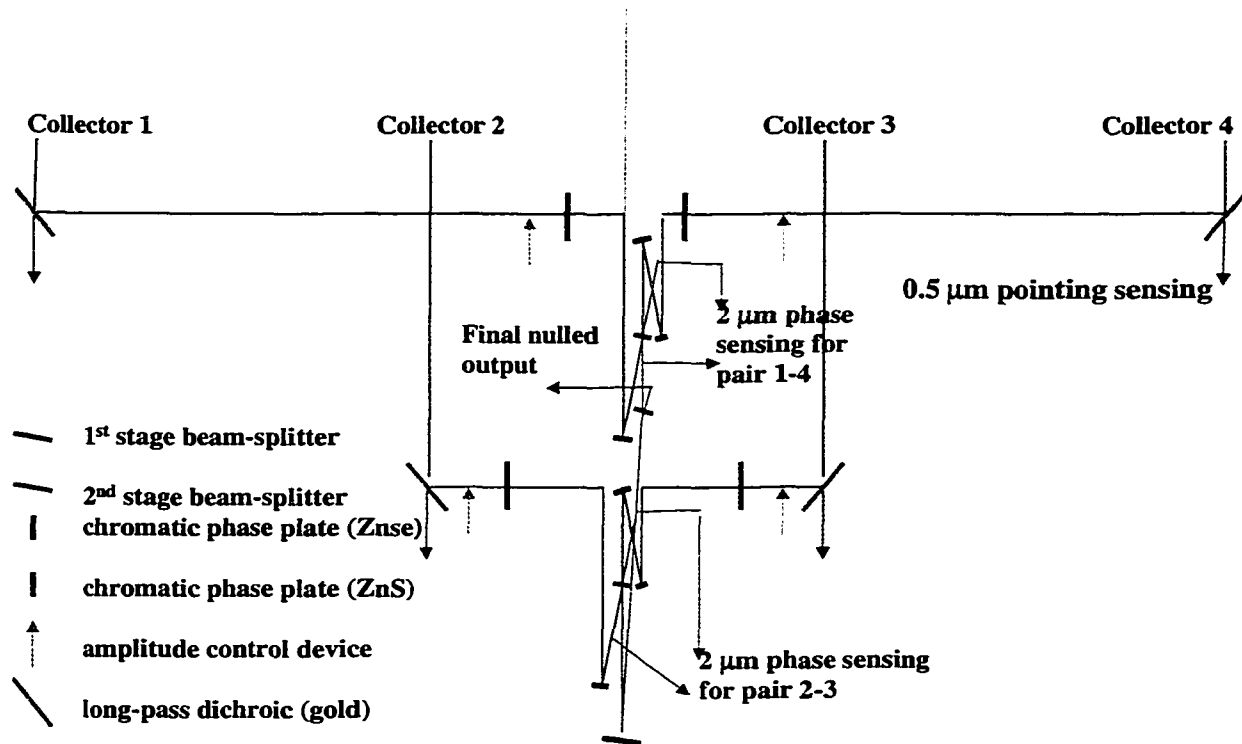


Figure 9.3 An optical layout of an OASES beam-combiner.

The beams are combined similar to the ground-based nulling approach on the MMT. That is, the image orientation is preserved, the reflections off the beam-splitters are kept nearly normal to avoid polarization-dependent effects of a dielectric stack, all combining optics are kept in one plane, and the optical paths of the two beams being combined are kept as similar as possible so that effects such as different incidence angles of reflection for the two beams do not affect the

relative phase. In this scheme pointing control of each element is sensed at  $0.5\ \mu\text{m}$  and phase control is sensed at  $2\ \mu\text{m}$ . The achromaticity of the null is tuned by ZnSe/ZnS plates in each pair of beams. Amplitude devices will also be required in each beam. Most likely these can be simple devices which block a small portion of the light ( $<1\%$ ) in each beam to equalize the amount of light in each pair. The first stage beam-splitters are the most critical since these must be properly adjusted to achieve a null from each pair of telescopes. The second stage beam-splitter is less critical since it simply fine tunes the width of the null, in the OASES setup, or the phase chopping, in the double Bracewell setup.

### 9.3. Nulling with a Mesh Beam-splitter

One challenging requirement in the current baseline for TPF is the broad wavelength coverage needed ( $7\text{-}17\ \mu\text{m}$ ) to study regions of the spectrum important for understanding the chemical makeup of the planet and signs of habitability and life. The nulling concept presented in chapters 2-3 can be extended over broader ranges by using a second dielectric compensation, as suggested by Angel, Burge, and Woolf (1996), but the tolerances required on the amplitude matching require thin-film stacks which have broad-band performance over  $> 100\%$  bandwidth. This is a serious difficulty for thin film design. Other nulling techniques (Shao and Colavita 1992) use a beam-splitter in double pass, thus avoiding this difficulty. However these techniques are limited to 50:50 combination of the light, which may not be the desired ratio in a TPF mission, as shown for the different configurations above.

The technique outlined below is a novel way of doing nulling which combines the advantages of a single-pass system (simple beam combination, non-rotation of

pupils) with the achromaticity needed for a TPF mission.

All the current techniques make use of thin-film stacks which are roughly 50% transmissive in order to mix the light from a pair of telescopes. These techniques are inherently limited by the spectral performance of the thin film stack, although by using the beam-splitter in a double-pass the effects of chromatic variations can be minimized. Instead it is possible to mix the light by using a beam-splitter which has a reflective (metallic) coating over 50% of the beam area. These beam-splitters

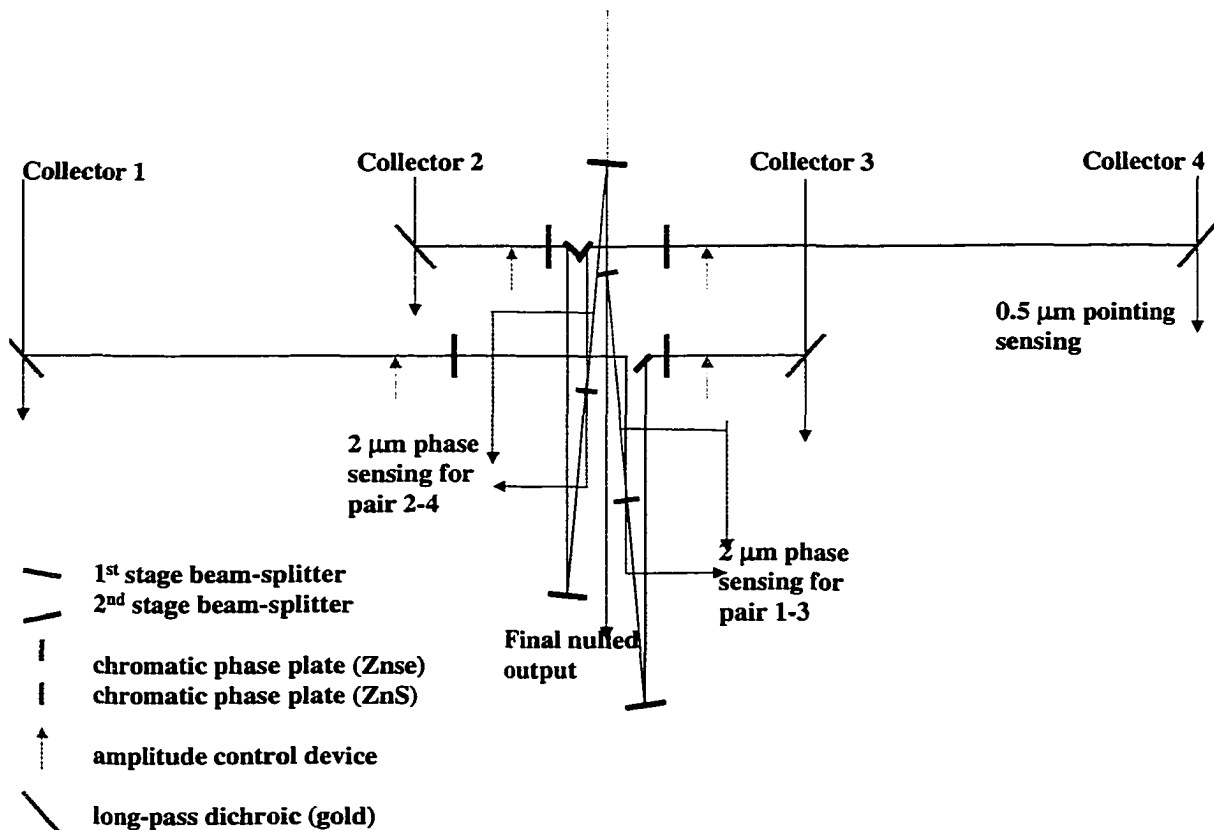


Figure 9.4 An optical layout for a double Bracewell beam-combiner.

are often referred to as polka-dot or mesh beam-splitters, and are typically an aluminum coating of 0.1-1 mm dots on a suitable glass substrate. The beam combination for these beam-splitters is different from thin-film designs and is thus worth going through in detail.

In a symmetric system (Figure 2.1) the beam-splitter reflects one beam while transmitting the other. The beam-splitter creates a 90 degree phase shift between the beams as described in chapter 2. This creates a situation where both outputs of the beam-splitter are equal in intensity. By changing the phase it is possible to get a constructive image in one output and a nulled image in the other. This is quite different from a mesh beam-splitter. In this case the phase shift between the beams is determined by the reflective coating of the material, which is only encountered by the reflected beam. For most metals used as good reflectors this phase shift is nearly 180 degrees (gold at 10  $\mu\text{m}$  is 178 degrees). Thus both outputs of the beam-splitter have interfered beams which are (nearly) out of phase. A nulled image is created for both outputs. In a thin-film system, for comparison, all the light suppressed in one output appears in the other output of the interferometer. A true null could be created by path-length difference and dielectric compensation, but the null could be tuned much more easily since only a few degrees of phase shift (to fine tune the  $\sim 178^\circ$  shift of a metal reflection) would be needed to create the null. However creating a nulled image in both outputs would seem to violate the conservation of energy. Where does the light go?

A mesh beam-splitter diffracts the light as well as reflecting half the amount, and is in this sense different from a thin-film stack beam-splitter. Thus the light is spread into orders by the grid pattern in the beam-splitter. When the phase difference between the beams is one-half wave, the 0th order image is cancelled

out and the light is diffracted into the  $m=1$  and  $-1$  orders. When the light is in phase between the beams all of the energy from the star appears in the 0th order. It is easiest to visualize if the mesh beam-splitter is thought of as a series of reflective stripes covering half the area. Then when the light destructively interferes two bright images appear to either side of the central nulled star. A numerical calculation of the image for a striped beam-splitter is shown in Figure 9.5 for different phase shifts between the beams.

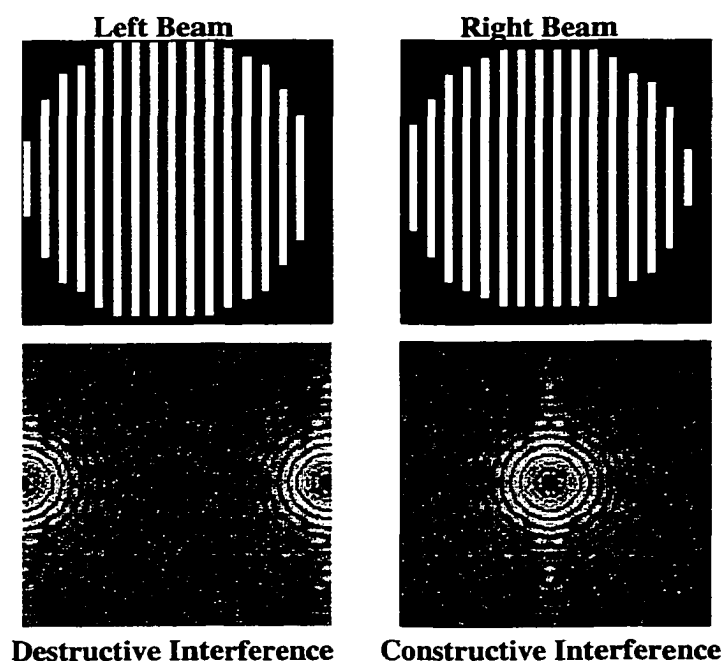


Figure 9.5 Pupil of a mesh beam-splitter system and resulting images. The two images, shown in logarithmic stretch to emphasize the faint detail, correspond to the beams interfering destructively or constructively. The residual light in the destructive image is  $6 \times 10^{-5}$  near the central source.



For a nonsymmetric system with an equal number or +2 reflections between the beams the situation is different. No phase shift is introduced at all for the equal reflection case, while a phase shift of only a few degrees is incurred for a system with a difference of two reflections. The advantage of a nonsymmetric system over a symmetric system is the same as for a thin-film beam-splitter: the off-axis image is not doubled to either side of the pointing center. For this system the phase could be introduced by dielectric plates to create a null in the same way as described in chapter 3.

An important issue is the optimum size for the individual dots or stripes on the beam-splitter. It is necessary to have the dots significantly (50-100 times) larger than the wavelength of light so that the light splitting can be independent of the wavelength of light. This suggests a size of about 1 mm for the individual dots. The required beam size is set by the number of dots needed across the beam to reach a certain level of precision. The finite size of the dots leads to the beams being slightly shifted one with respect to the other. In other words a slight pupil misalignment of the beams is introduced which gives a fractional shift to the pupil on the order of the dot size over the beam size. This effect can be estimated numerically, by creating the pupils, combining them out of phase, and taking the Fourier transform to obtain the resulting image. Performing this calculation for a different number of stripes across the pupil suggests that approximately 100 stripes are needed to achieve a suppression factor of  $10^6$ . For 0.5 mm dots this would require a beam size of 50 mm, a reasonable size for beam combination.

### **9.3.1. Signal-to Noise Comparison of a Mesh Beam-splitter**

In a typical nulling combiner, as described in chapter 3, a constructively interfered image contains all the energy of both elements and the equivalent background

from one telescope, since the background is split into two outputs. For a mesh beam-splitter the energy for a given source is split between the outputs, and the phase difference between the beams simply changes its position in the focal plane. Compared with the thin-film beam-splitter the mesh beam-splitter has a factor of 2 less signal in a given output. If both outputs are used to measure the signal, the signal-to-noise comparison is still  $\sqrt{2}$  times worse for the mesh beam-splitter.

The background can be reduced by inserting a cold field stop the size of the Airy pattern in each element. This creates a background only from the portion of the sky corresponding to the source position. Since the background from each element is not coherent, the light from it is split equally between the 0th order image and the  $\pm 1$ st order images. This results in the same signal-to-noise as a conventional beam-splitter, but at the cost of only being able to detect signals within the Airy core of a single element.

## REFERENCES

- Allen, C.W. 2000, *Allen's Astrophysical Quantities*, ed. Arthur N. Cox (New York : AIP press)
- Angel, R. 1990, *Proc. NASA/STSCI Workshop on Next Generation Space Telescope*, Bely, P., Burrows, C., & Illingworth, G. Space Telescope Science Center Institute, Baltimore MD, p. 81
- Angel, J. R. P. 1994, *Nature* 368, 203
- Angel, J. R. P., Burge, J. & Woolf, N. J. 1996, *Proc. SPIE* 2871, 516
- Angel, J. R. P. & Woolf, N. J. 1997, *ApJ* 475, 373
- Angel, J. R. P. et al. 2001 PowerPoint presentation.
- Aumann, H.H., Gillett, F.C., Beichman, C.A., deJong, T., Houck, J.R., Low, F.J., Neugebauer, R.G., Walker, R.G., Wesselius, P.R. 1984 *ApJ* 278, L23
- Baudoz, P., Rabbia, Y., Gay, J. 2000, *A&ASup* 141, 319
- Beckers, J.M. 1993, *AR&AA* 31, 13
- Beichman, C. A., Woolf, N. J. & Lindensmith, C. 1999, *Terrestrial Planet Finder, Jet Propulsion Laboratory: Pasadena CA, JPL Publication 99-3*
- Bester, M., Danchi, W.C., Hale, D., Townes, C.H., Degiacomi, C.G., Mekarnia, D. Geballe, T.R. 1996, *ApJ* 463, 336
- Born M., & Wolf, E. 1993, *Principles of Optics*, Pergaman Press, Oxford, NewYork
- Bracewell, R. N. 1978, *Nature* 274, 780

- Butler, R.P., Marcy, G.W., Vogt, S.S., Fischer, D.A. 2000, IAU Symposium 202, Planetary Systems in the Universe
- Burrows, A., Marley, M., Hubbard, W.B., Lunine, J.I., Guillot, T., Saumon, D., Freedman, R., Sudarsky, D., & Sharp, C. 1997, ApJ 491, 856
- Chiang, E.I., & Goldreich, P. 1997, ApJ, 490, 368
- Cohen, M., Wittenborn, F.C., Carbon, D.F., Davies, J.K., Wooden, D.H., & Bregman, J.D. 1996, AJ, 112, 2274
- D'Alessio, P., Canto, J., Calvet, N., Lizano, S. 1998, ApJ 500, 411
- Danchi, W.C., Bester, M., Degiacomi, C.G., Greenhill, L.J., & Townes, C.H. 1994, AJ 107, 1469
- Gay, J., Rabbia, Y. & Manghini, C. 1997 Infrared Space Interferometry: Astrophysics & the Study of Earth-Like Planets, ed. C. Eiroa, Kluwer Academic p. 187
- Gilliland, R.L., & Dupree, A.K. 1996, ApJ 463, L29
- Grady, C.A., Devine, D., Woodgate, B., Kimble, R., Bruhweiler, F.C., Boggess, A., Linsky, T.L., Plait, P., Clampin, M., Kalas, P. 2000, ApJ, 544, 895
- Hardy, J.W. 1998, Adaptive Optics for Astronomical Telescopes, Oxford University Press, Oxford, New York
- Hebden, J.C., Christou, J.C., Cheng, A.Y.S., Hege, E.K., Strittmatter, P.A., Beckers, J.M., & Murphy, H.P. 1987, ApJ 309, 745
- Hillenbrand, L., Strom, S.E., Vrba, F.J., Keene, J. 1992, ApJ, 397, 613

- Hinz, P. M., Angel, J. R. P., Hoffmann, W. F., McCarthy, D. W., McGuire, P. C., Cheselka, M., Hora, J. L., & Woolf, N. J. 1998, *Nature* 395, 251
- Hinz, P. M., Angel, R., Woolf, N., Hoffmann, W., McCarthy, D.W. 1999 *Working on the Fringe: Optical and IR Interferometry from Ground and Space. Proceedings from ASP Conference Vol. 194.* Eds. Stephen Unwin and Robert Stachnik p. 401
- Hoffmann, W.F., Hora, J.L., Fazio, G.G., Deutsch, L.K., & Dayal, A. 1998 *Proc. SPIE* 3354, 647
- Jones, B.W., Sleep, P.N., Chambers, J.E. 2001, *A&A* 366,254J
- Jura, M., & Kleinmann, S.G. *ApJS*, 83, 329
- Kelsall, T., Weiland, B.A., Franz, B.A., Reach, W.T., et al. 1998, *ApJ* 508, 44
- Kenyon, S.J., & Hartmann, L. 1987, *ApJ* 323, 714
- Langlois, M., Sandler, D., Ryan, P., & McCarthy, D. 1998, *Proc. SPIE* 3353, 189
- Leger, A., Pirre, M. & Marceau, F. 1993, *Astron. Astrophys.* 277, 309
- [ ] Leger, A., Mariotti, J.M., Menesson, B., Puget, J.L., Rouan, D., & Schneider, J. 1996 *Icarus* 123, 249
- Lim, J., Carilli, C.L., White, S.M., Beasley, A.J., & Marson, R.G. 1998, *Nature* 392, 575
- Lloyd-Hart, M. 2000, *PASP* 112, 264
- Lopez, B. 1998, *Asymptotic Giant Branch Stars*, IAU Symp. 191

- Lunine, J. 2000 Proceedings of the National Academy of Sciences, Astrobiology Special Issue
- Mannings, V. & Sargeant, A.I. 1997, ApJ 490, 792
- Marcy, G.W., Cochran, W.D. & Mayor, M. 2000 Protostars and Planets IV, eds. Mannings, V., Russel, S., & Boss, A.P., University of Arizona Press, Tucson, Arizona, p. 1285
- Martin, H.M. 1992 App. Opt.
- Meeus, G., Waters, L.B.F.M., Bouwman, J., van den Ancker, M.E., Waelkens, C., and Malfait, K. 2000, A&A
- Michelson A.A., & Pease, F.G. 1921, ApJ 53, 249
- Nelson, J. 2000 PowerPoint Presentation [www.ucolick.org/~celt/presentations.html](http://www.ucolick.org/~celt/presentations.html)
- Osterbart, R., Balega, Y.Y., Blocker, T., Men'shchikov, A.B., Weigelt, G. 1999, A&A 348, 805
- Petit, J.M., Morbidelli, A., Chambers, J. 2000 Icarus in press
- Phillips, J.D., & Hickey, C. 1995 Proc. SPIE 2477, 15
- Ryan, P.T., Fugate, R.Q., Langlois, M., & Sandler, D.G. 1998, Proc. SPIE 3353, 107
- Sandler, D.G., Stahl, S., Angel, J.R.P., Lloyd-Hart, M., McCarthy, D. 1994, J. Opt. Soc. Am. A 11, 925
- Shao, M. & Colavita, M. M. 1992, Ann. Rev. Astron. & Astrophys. 30, 457
- Shu, F.H., Adams, F.C., & Lizano, S. 1987 ARA&A 25, 23

- Stahl, S.M., & Sandler, D.G. 1995, ApJ 454, 153
- Sudol, J.J., Dyck, H.M., Stencel, R.E., Klebe, D.E., Creech-Eakman, M.J. 1999, AJ 117 1609
- Tuthill, P.G., Monnier, J.D., et al. 2000, ApJ in press
- Wizinowich, P., McLeod, Lloyd-Hart, M., Angel, J.R.P., Colucci, D., Dekany, R., McCarthy, D., Wittman, D., Scott-Fleming, I. 1992, App. Op. 31 6036
- Woolf, N. J. & Angel, J. R. P. 1995, OSA Technical Digest 23
- Woolf, N. J., Angel, J.R.P., Beichman, C.A., Burge, J.H., Shao, M., Tenerelli, D.J. 1998 Proc. SPIE 3350, 683